UNIVERSITAT POLITÈCNICA DE VALÈNCIA
DEPARTAMENTO DE MÁQUINAS Y MOTORES TÉRMICOS

DOCTORAL THESIS

AEROTHERMAL CHARACTERISATION OF SURFACE HEAT EXCHANGERS FOR TURBOFANS

PRESENTED BY

D. Andrés Felgueroso Rodríguez

SUPERVISED BY

Dr. D. Jorge García Tíscar

FOR THE DEGREE OF

Doctor of Philosophy

JUNE 2023

DOCTORAL THESIS

"Aerothermal characterisation of surface heat exchangers for turbofans"

Presented by: D. Andrés Felgueroso Rodríguez
Supervised by: Dr. D. Jorge García Tíscar

THESIS EXAMINERS

Dr. D. Simone Mancin
Dr. D. Daniel Gil Prieto
Dr. D. Ezequiel González Martínez

DEFENSE COMITEE

Chairman: Dr. D. Antonio José Torregrosa Huguet
Secretary: Dr. D. Octavio Armas Vergel
Member: Dr. D. Daniel Gil Prieto

Valencia, June 2023

A Ángeles Marcelina

Abstract

In a present marked by the continuous fight against pollution and climate change, research into technological improvements that allow an acceptable transition for society towards a greener future occupies a fundamental role. Specifically, aviation is a constant focus of innovation, since it is considered an essential function in a society as globalized as today's, but with worrying levels of pollution.

In this regard, the development of engines with high efficiencies such as high bypass ratio turbofans, or even hybridization with electric propulsion plants, is a key step for the environmental transition. However, these types of alternatives present a technological challenge in terms of their thermal management, based mainly on the need to increase the cooling of new components. In this context and promoted by the *Aerodynamic upgrade of Surface Air Cooled Oil Cooler (SACOC)* project of Clean Sky 2, this doctoral thesis focuses on the experimental study of geometries of heat exchangers of surface for cooling the engine oil through the use of air from the secondary flow of the turbofan. Currently, there are a number of limitations regarding the capacity to carry out a detailed analysis and design of this type of heat exchanger due to the lack of facilities that allow a correct, complete and robust experimental characterisation. The main data sources are based on numerical calculations validated from extrapolations under conditions of questionable applicability.

Throughout the thesis, the results obtained after a detailed characterisation of four different geometries of heat exchangers using both intrusive and optical techniques are presented. Firstly, a detailed introduction of the installation designed and used for the characterisation is made. A flow bank is capable of generating a typical draft around the exchangers, while an oil conditioning system controls the point of operation on the hot side. To more realistically recreate operating conditions, a methodology is presented to automatically generate distortion screens capable of reproducing

a two-dimensional distribution of target velocities through additive manufacturing of variable porosity panels. This model, analyzed by means of CFD and validated experimentally, is used to reproduce the typical speed profile present around the exchanger in a real operating circumstance.

After defining relevant metrics that allow analysing the behaviour of the different geometries, it is concluded that aerodynamic and thermal problems are highly coupled in these devices, demonstrating the need for careful design to improve the performance of the exchanger. The results show that an improvement of more than 12% in pressure drop and almost 20% in heat exchange can be obtained. In addition, the impact of using the distortion screen has been confirmed, with variations of the order of 10% in both variables. The results also show that it is possible to perform a preliminary characterisation reliably with a 3D printed model, as the results are practically identical to those of the aluminium model in terms of velocity fields, pressure losses and corrected eigenfrequencies.

With the meticulous analysis carried out in this doctoral thesis, it can be concluded that it is essential to have an experimental installation that reproduces the real operating conditions of an engine to carry out relevant studies of heat exchangers. For this, it is necessary to use appropriate metrics together with the development of an exhaustive, reliable and robust methodology. The results and methodology presented in this research may have a significant impact, not only at an academic level, but also at an industrial level, since they open the door to developing more efficient thermal management systems in preliminary design stages that are more economically affordable, they consume less time and have greater flexibility to introduce modifications in the geometries.

Resumen

En un presente marcado por la continua lucha contra la contaminación y el cambio climático, la investigación en mejoras tecnológicas que permitan una transición aceptable para la sociedad hacia un futuro más ecológico ocupa un papel fundamental. En concreto, la aviación es un foco constante de innovación, ya que es considerada una función indispensable en una sociedad tan globalizada como la actual, pero con unos niveles de contaminación preocupantes.

En este aspecto, el desarrollo de motores con altas eficiencias como turbofans de alta relación de derivación, o incluso la hibridación con plantas propulsivas eléctricas, es un paso clave para la transición medioambiental. Sin embargo, este tipo de alternativas presentan un reto tecnológico en cuanto a su gestión térmica basado, principalmente, en la necesidad de aumentar la refrigeración de nuevos componentes. En este contexto e impulsada por el proyecto *Aerodynamic upgrade of Surface Air Cooled Oil Cooler (SACOC)* de Clean Sky 2, esta tesis doctoral se centra en el estudio experi- mental de geometrías de intercambiadores de calor de superficie para la refrigeración del aceite motor mediante el uso del aire del flujo secundario del turbofan. Actualmente, existen una serie de limitaciones en cuanto a las capacidades para llevar a cabo un análisis y diseño detallado de este tipo de intercambiadores de calor debido a la falta de instalaciones que permitan un correcta, completa y robusta caracterización experimental. Las principales fuentes de datos se basan en cálculos numéricos validados a partir de extrapolaciones en condiciones de cuestionable aplicabilidad.

A lo largo de la tesis se presentan los resultados obtenidos tras una detallada caracterización de cuatro diferentes geometrías de intercambiadores de calor empleando tanto técnicas intrusivas como ópticas. Primeramente, se hace una introducción detallada de la instalación diseñada y utilizada para la caracterización. Un banco de flujo es capaz de generar una corriente de aire típica alrededor de los intercambiadores, mientras que un sis-

tema de acondicionamiento de aceite controla el punto de operación por el lado caliente. Para recrear de manera más realista las condiciones de funcionamiento, se presenta una metodología para generar de manera automática pantallas de distorsión que son capaces de reproducir una distribución bidimensional de velocidades objetivo mediante la manufactura aditiva de paneles de porosidad variable. Este modelo, analizado mediante CFD y validado experimentalmente, se utiliza para reproducir el perfil de velocidades típico presente en torno al intercambiador en una circunstancia real de operación.

Tras definir métricas relevantes que permitan analizar el comportamiento de las distintas geometrías, se llega a la conclusión de que los problemas aerodinámico y térmico están altamente acoplados en estos dispositivos, demostrando la necesidad de un cuidadoso diseño para mejorar las actuaciones del intercambiador. Los resultados muestran que puede llegar a obtenerse una mejora de más de un 12% en la caída de presión y casi un 20% en el intercambio de calor. Además, se ha confirmado el impacto del uso de la pantalla de distorsión, con variaciones del orden de 10% en ambas variables. Los resultados también muestran que es posible realizar una caracterización preliminar de manera fiable con un modelo impreso en 3D, pues los resultados son prácticamente idénticos a los del modelo de aluminio en cuanto campos de velocidades, pérdidas de presión y frecuencias propias corregidas.

Con el minucioso análisis llevado a cabo en esta tesis doctoral, se puede concluir que es fundamental tener una instalación experimental que reproduzca las condiciones de funcionamiento reales de un motor para realizar estudios relevantes de intercambiadores de calor. Para ello, es necesario el uso de métricas adecuadas junto con el desarrollo de una metodología exhaustiva, fiable y robusta. Los resultados y metodología presentados en esta investigación pueden llegar a tener un impacto importante, no solo a nivel académico, si no a nivel industrial, ya que abren la puerta a desarrollar sistemas de gestión térmica más eficiente en unas etapas de diseño preliminares que son más asequibles económicamente, consumen menos tiempo y tienen mayor flexibilidad para introducir modificaciones en las geometrías.

Resum

En un present marcat per la lluita contínua contra la contaminació i el canvi climàtic, la recerca en millores tecnològiques que permetin una transició acceptable per a la societat cap a un futur més ecològic ocupa un paper fonamental. Concretament, l'aviació és un focus constant d'innovació, ja que és considerada una funció indispensable en una societat tan globalitzada com l'actual, però amb uns nivells de contaminació preocupants.

En aquest aspecte, el desenvolupament de motors amb altes eficiències com turbofans d'alta relació de derivació, o fins i tot la hibridació amb plantes propulsives elèctriques, és un pas clau per a la transició mediambiental. Tot i això, aquest tipus d'alternatives presenten un repte tecnològic quant a la seva gestió tèrmica basat, principalment, en la necessitat d'augmentar la refrigeració de nous components. En aquest context i impulsada pel projecte *Aerodynamic upgrade of Surface Air Cooled Oil Cooler (SACOC)* de Clean Sky 2, aquesta tesi doctoral se centra en l'estudi experimental de geometries d'intercanviadors de calor de superfície per a la refrigeració de l'oli motor mitjançant l'ús de l'aire del flux secundari del turbofan. Actualment, hi ha una sèrie de limitacions quant a les capacitats per dur a terme una anàlisi i disseny detallat d'aquest tipus d'intercanviadors de calor a causa de la manca d'instal·lacions que permetin una caracterització experimental correcta, completa i robusta. Les fonts de dades principals es basen en càlculs numèrics validats a partir d'extrapolacions en condicions de qüestionable aplicabilitat.

Al llarg de la tesi es presenten els resultats obtinguts després d'una detallada caracterització de quatre geometries diferents d'intercanviadors de calor emprant tant tècniques intrusives com òptiques. Primerament, es fa una introducció detallada de la instal·lació dissenyada i utilitzada per a la caracterització. Un banc de flux és capaç de generar un corrent d'aire típic al voltant dels intercanviadors, mentre que un sistema d'acondicionament d'oli controla el punt d'operació pel costat calent. Per recrear de manera

més realista les condicions de funcionament, es presenta una metodologia per generar de manera automàtica pantalles de distorsió que són capaces de reproduir una distribució bidimensional de velocitats objectiu mitjançant la manufactura additiva de panells de porositat variable. Aquest model, analitzat mitjançant CFD i validat experimentalment, sutilitza per reproduir el perfil de velocitats típic present al voltant de lintercanviador en una circumstància real doperació.

Després de definir mètriques rellevants que permetin analitzar el comportament de les diferents geometries, s'arriba a la conclusió que els problemes aerodinàmic i tèrmic estan altament acoblats en aquests dispositius, demostrant la necessitat d'un disseny acurat per millorar les actuacions de l'intercanviador. Els resultats mostren que es pot obtenir una millora de més d'un 12% en la caiguda de pressió i gairebé un 20% en l'intercanvi de calor. A més, s'ha confirmat l'impacte de l'ús de la pantalla de distorsió, amb variacions de l'ordre del 10% a les dues variables. Els resultats també mostren que és possible fer una caracterització preliminar de manera fiable amb un model imprès en 3D, ja que els resultats són pràcticament idèntics als del model d'alumini en tant que camps de velocitats, pèrdues de pressió i freqüències pròpies corregides.

Amb la minuciosa anàlisi duta a terme en aquesta tesi doctoral, es pot concloure que és fonamental tenir una instalůlació experimental que reprodueixi les condicions de funcionament reals d'un motor per fer estudis rellevants d'intercanviadors de calor. Per fer-ho, cal fer servir mètriques adequades juntament amb el desenvolupament d'una metodologia exhaustiva, fiable i robusta. Els resultats i metodologia presentats en aquesta investigació poden arribar a tenir un impacte important, no només a nivell acadèmic, sinó a nivell industrial, ja que obren la porta a desenvolupar sistemes de gestió tèrmica més eficient en unes etapes de disseny preliminars que són més assequibles econòmicament, consumeixen menys temps i tenen més flexibilitat per introduir modificacions a les geometries.

List of publications

Following the work performed in the framework of this doctoral thesis and its associated projects, the following journal papers have been published:

[1] A. Broatch, P. Olmeda, J. García-Tíscar, A. Felgueroso, et al. "Experimental aerothermal characterization of surface air-cooled oil coolers for turbofan engines". International Journal of Heat and Mass Transfer 190, 2022, p. 122775.

[2] J. Sánchez-Dehesa, P. Gao, F. Cervera, A. Broatch, J. García-Tíscar, and A. Felgueroso. "Experimental evidence of the Poisson-like effect for flexural waves in thin metallic plates". Applied Physics Letters 120, 9 2022, p. 094102.

[3] A. Broatch, X. Margot, J. García-Tíscar, and A. Felgueroso. "An automatized methodology to generate velocity distortion panels for wind tunnel testing". Journal of Wind Engineering and Industrial Aerodynamics 227, 2022, p. 105065.

[4] M. Chávez-Modena, L. M. González, E. Valero, A. Broatch, J. García-Tíscar, and A. Felgueroso. "Experimental and numerical methodology for the aero-thermal analysis of a SACOC heat exchanger". Applied Thermal Engineering 219, 2023, p. 119409.

[5] A. Broatch, J. García-Tíscar, A. Felgueroso, M. Chávez-Modena, L. González, and E. Valero. "Numerical and experimental analysis of rounded fins for high speed air-cooled heat exchangers". International Journal of Heat and Mass Transfer 201, 2023, p. 123575.

Additionally, one more manuscript has been submitted to the journal Applied Thermal Engineering and is undergoing peer review:

[6] A. Broatch, J. García-Tíscar, P. Quintero, and A. Felgueroso. "Rapid aerodynamic characterization of surface heat exchangers for turbofan aeroengines through optical techniques and additive manufacturing". Submitted to Applied Thermal Engineering, 2023.

The results have also been presented in different international conferences:

[7] M. Chávez-Modena, L. M. González, E. Valero, A. Broatch, J. García-Tíscar, and A. Felgueroso. "Numerical and experimental analysis of thermo- aerodynamic performance in an aero engine surface heat exchanger". In: AIAA Aviation 2021 Forum. 2021.

[8] J. Sánchez-Dehesa, P. Gao, F. Cervera, A. Broatch, J. García-Tíscar, and A. Felgueroso. "Redirection of flexural waves in thin plates". In: Euronoise. 2021.

[9] A. Broatch, J. García-Tíscar, A. Felgueroso, M. Gelain, and A. Couilleaux. "Non-intrusive aerothermal characterization of surface heat exchangers for turbofan aeroengines". In: International Council of the Aeronautical Sciences. 2022.

[10] J. Sánchez-Dehesa, P. Gao, F. Cervera, A. Broatch, J. García-Tíscar, and A. Felgueroso. "Collimation and redirection of flexural waves in thin elastic plates". In: Proceedings of the 24th International Congress on Acoustics. 2022.

Division of work between authors

The work leading up to this thesis was done in collaboration with other researchers. The respondent is the co-author of all papers on which this thesis is based, with author signatures being in order of seniority in the Institute. The respondent implemented the proposed methodology into the different experimental setups, performed the measurements, processed the experimental results and extracted the presented conclusions. Discussions were also performed in collaboration with supervisor Dr. García-Tíscar and the rest of the co-authors. Numerical simulations were not performed by the respondent, and are thus gratefully acknowledged.

Funding acknowledgements

The respondent wishes to acknowledge the financial support received through the Programa de Apoyo para la Investigación y Desarrollo (PAID) of Universitat Politècnica de València under grant PAID-01-20 n° 21589.

This project has received funding from the Clean Sky 2 Joint Undertaking under the European Unions Horizon 2020 research and innovation programme under grant agreement No 831977 Aerodynamic upgrade of Surface Air-Cooled Oil Coolers (SACOC).

Acknowledgements

If life is a journey, it is in moments like those during the doctorate that one realises that people around you can make the difference between a stairway to heaven or a highway to hell.

Firstly, my more than obvious gratitude and deep respect to Dr Jorge García Tíscar and Prof. Alberto Broatch, my closest advisors during this time. No matter how much one could know beforehand, working with you two has been open-minding to realise how much one needs to learn to reach your competence. I would like to extend my acknowledgements to all the people in our research line but, particularly, to all the technicians I have had the pleasure to work with. Fito, knowing that you had my back was always a relief.

I would like to thank also my all-time friends and very long-time friends. But those I have made during this PhD, those who stood by me for these years, who release the pressure with a beer, hiking, doing some sports or whatever excuse we could think of to hang out, my special thanks go to you. You know who you are, so I will not make an endless list with your names.

Of course, my family. I do not know what I could have achieved without you. All the effort you put to get me where I am now, all conversations (sometimes even monologues) where you did not understand any of my concerns about my daily work, but you kept listening because you knew that it helped me. I am not sure there is enough gratitude inside a person to express what I feel.

And finally, to my wife (still not used to how it sounds), Ángeles Marcelina, the best partner one could have/dream/aspire to. In my journey, knowing that you are going to be there no matter where we go, is my major accomplishment (even above this thesis), so thank you for being there, putting up with me and sharing my dreams.

Valencia, 2023

Contents

List of Figures

List of Tables

List of Symbols

Latin

A	Area	m^2
C_p	Specific heat capacity at constant pressure	$\mathrm{J\,kg^{-1}\,K^{-1}}$
D_h	Hydraulic diameter	m
E	Modulus of elasticity	Pa
f	Fanning friction coefficient or Frequency	— or Hz
g	General variable	—
H	Test section Height	m
h	Convective heat transfer coefficient	$\mathrm{W\,m^{-2}\,K^{-1}}$
j	Colburn factor	—
K	Pressure loss factor	—
k	Thermal conductivity	$\mathrm{W\,m^{-1}\,K^{-1}}$
L	Length	m
$\dot{m}$	Mass flow rate	$\mathrm{kg\,s^{-1}}$
M	Mach number	—
Nu	Nusselt number	—
P	Pressure	Pa
Pr	Prandtl number	—
$\dot{Q}$	Heat rate	W
$\dot{Q}_b$	Baseline heat rate	W
R	Specific gas constant	$\mathrm{J\,kg^{-1}\,K^{-1}}$
R_b	Blend radius	m
Re	Reynolds number	—
S	Porosity	%
T	Temperature	K
t	Thickness	m
U	Overall Heat Transfer coefficient	$\mathrm{W\,m^{-2}\,K^{-1}}$
U_∞	Max. target and reference velocity	$\mathrm{m\,s^{-1}}$
u, v, w	Velocity components	$\mathrm{m\,s^{-1}}$
V	Velocity magnitude	$\mathrm{m\,s^{-1}}$
x, y, z	Spatial coordinates	m
y^+	Non-dimensional boundary layer distance	—

Greek

ΔT_{lm}	Log mean temperature difference	K
δ	Vibration displacement	m
γ	Ratio of specific heats	—
ϵ	Wall roughness	m
η_0	Overall surface efficiency	%
η_f	Fin efficiency	%
θ	Temperature difference	K
Λ	Fin perimeter	m
λ	Panel flow-wise thickness	m
μ	dynamic viscosity	Pa s
ν	kinematic viscosity	$m^2\,s^{-1}$
ρ	Density	$kg\,m^{-3}$
σ	Standard deviation	—

Sub- and superscripts

$\bar{}$	Average value
$'$	Fluctuations
∞	Reference value
$*$	Corrected variable
1	Related to the upstream region
2	Related to the downstream region
a	Related to the air
Al	Related to the aluminium heat exchanger
b	Related to the base
$cell$	Related to a cell
$conv$	Convection
Exp	Variable measured experimentally
f	Related to the fins
i, j	Discrete regions
in	Related to the inlet
IR	Measured with IR thermography
$Kiel$	Measured with Kiel probes
LDA	Measured with LDA
m_1	First mode
max	Maximum value
Num	Variable derived numerically
o	Related to the oil
out	Related to the outlet
PIV	Measured with PIV
s	Related to the solid

Acronyms

1D, 2D, 3D	One- Two- Three-dimensional
3Dp	3D-printed
A_0	Antisymmetric zero-order waves
ABS	Acrylonitrile Butadiene Styrene
AM	Additive Manufacturing
ACOC	Air-Cooled Oil Cooler
ASA	Acrylonitrile Styrene Acrylate
BOS	Background Oriented Schlieren
CAD	Computer-Aided Design
CFD	Computational Fluid Dynamics
CNC	Computer Numerical Control
CW	Continuous-Wave
DAQ	Data Acquisition
DES	Detached Eddy Simulation
DMS1, DMS2	Downstream Measurement Section 1 & 2
FEM	Finite Elements Methods
FDM	Fused Deposition Modelling
FoV	Field of View
FSI	Fluid-Structure Interaction
HMHT	High Mass-flow and High Temperature
HWA	Hot Wire Anemometry
IR	Infrared
LDA	Laser Doppler Anemometry
LDV	Laser Doppler Vibrometry
LES	Large Eddy Simulation
MKE	Mean Kinetic Energy
Nd:YAG	Neodymium-doped Yttrium Aluminium Garnet
NI	National Instruments
ODS	Operational Deflection Shapes
OGV	Outlet Guide Vane
PDF	Probability Density Function
PID	ProportionalIntegralDerivative
PIV	Particle Image Velocimetry
PLIF	Planar Laser-Induced Fluorescent
PZT	Piezoelectric transducer
RANS	Reynolds-Averaged Navier-Stokes
RTD	Resistance Temperature Detector
SACOC	Surface Air-Cooled Oil Cooler
SAF	Sustainable Aviation Fuel
SFC	Specific Fuel Consumption
SLA	Stereolithography
SLS	Selective Laser Sintering
S-PIV	Stereoscopic Particle Image Velocimetry

SST	Shear Stress Transport
TC1 – TC4	Thermocouple locations 1 to 4
TKE	Turbulent Kinetic Energy
TKI	Turbulent Kinetic Intensity
UMS1	Upstream Measurement Section 1
UHBR	Ultra High Bypass Ratio
URANS	Unsteady Reynolds-Averaged Navier-Stokes

CHAPTER 1

Introduction

> "The future of engineering is bright, and heat transfer is a topic that is crucial to address a broad array of technological and environmental challenges."
>
> **T. Bergman, A. Lavine, F. Incropera**. *Fundamentals of Heat and Mass Transfer.*

This conclusion is derived by the authors in the preface of the 7^{th} edition of one of the most relevant books on heat transfer. They were trying to address the impact of the economic recession and new challenging technologies and environmental concerns in the relevance of thermal management. Even though this unease may seem reasonable, it is clear that the relevance and even critical role of heat transfer in many applications turn this field into a key factor to consider for the development of future technologies.

Nowadays, one of the technological challenges that needs more thorough research is the development of advanced thermal management systems for more efficient engine layouts. The present capabilities of new aero engine designs are reaching their limits as typical cold sources.

Not only new generations of aero engines such as ultra-high bypass turbofans or hybrid-electric engines are designed with a considerable increase in thermal loads, but also dissipating this heat is becoming more challenging.

The high usage of composite materials with lower operational temperatures and thermal conductivity limits the amount of heat that the aircraft structure can remove. Besides, these high-temperature sources discard fuel as a safe cold sink which, in addition, is less available in heat exchangers

as a coolant due to the improved efficiency of the engine. As a result, an innovative approach to engine cooling appears to be a growing industry need.

There is also considerable concern about pollution reduction which has been one of the major goals of technology research in the last years. In terms of aviation, an increase of 75% in efficiency in terms of fuel consumption and CO_2 emissions [11] with respect to the early jet age has not been enough to avoid an increase from 88 to 171 million tonnes (+95%) of CO_2 emissions between 1990 and 2016 [12]. Furthermore, global aviation demand is forecasted to quadruple from 2020 to 2050.

Aiming to achieve no net emissions of greenhouse gases in 2050, programs such as Clean Sky, Clean Sky 2 or Clean Aviation were born. The only way to have the necessary impact in terms of a climate-neutral and a sustainable aviation sector is to develop and mature game-changing technologies and ensure their adequate implementation.

This first chapter serves to contextualise the doctoral thesis research. Firstly, the relevance of the powerplant in the development of aircraft and aviation is briefly highlighted. Then, why heat exchangers are a key factor in the thermal management of these devices and the importance of the aerothermal coupling processes is stated. The state of the art and the contribution of this work regarding this technology is presented afterwards. It is followed by a brief contextualisation of the SACOC project, a Clean Sky 2 project that serves as a frame for the development of this doctoral thesis. The next point focuses on explaining the main objectives pursued with this doctoral thesis. Finally, it is explained how the document is structured for clarity.

1.1. Historical evolution of aviation powerplants

One of the critical components in an aircraft is the powerplant. The Wright brothers are historically known for being the first ones able to invent, build, and fly the world's first successful motor-operated aeroplane. Three days before entering the history books with their first flight, Wilbur Wright wrote to his family, referring to an almost successful flight attempt:

"The power is ample, and but for a trifling error due to lack of experience with this machine and this method of starting, the machine would undoubtedly have flown beautifully."

With this statement, it is clear that the amount of power available in the engines was a main concern for the brothers and was, in fact, one of their main contributions.

The evolution of the powerplant goes along with the development and improvements of aircraft. Another very well-known example is the contest between the Japanese and Americans during World War II.

The Mitsubishi A6M2 Zero overcame its American counterpart Grumman F4F Wildcat in speed and manoeuvrability due to its much lighter weight and cleaner aerodynamics. To solve this problem, the Americans basically improved the powerplant of the aircraft, designing the Grumman F6F Hellcat aircraft, which equipped a Pratt & Whitney R-2800 Double Wasp engine, a much more powerful engine which made them gain the aerial domain during the war.

During that time, another revolution in the design of powerplants was taking place: the invention and application of jet engines. Aircraft were reaching a limiting point related to the propellers' efficiency, so this was the solution found: an engine which thrusts the plane by means of compressed air and which is able to extract power from the engine itself.

After several improvements to the original design (patented by Frank Whittle in 1932 [13]), a major milestone was reached in the 60s: the development of the turbofan. The major efficiency of these engines was based on moving large amounts of air at lower velocities with a fan through a secondary bypass duct around the core (which is a jet engine). At first, bypass ratios were quite modest, but they rose steadily as technology advanced.

One of the main concerns while increasing the size of the engines was thermal management. More loads needed to be dissipated and more complex gearboxes and bearings were needed, with their corresponding lubrication and cooling systems.

The maximum and latest exponent of this type of engine is the recently developed UltraFan by Rolls Royce [14]. With more than 3.5 meters in diameter which allows a 15:1 bypass ratio, is the largest aero engine in the world and aims to reduce fuel consumption by up to 25% compared to the Trent family, being able also to run with 100% Sustainable Aviation Fuel (SAF). In addition to this, it also generates 40% less NO_x emissions, 35% less noise and almost zero non-volatile particulate emissions at cruise. It is still in the demonstration phase, but it has already accomplished the aerospace power record in civil aviation of featuring a planetary gearbox that delivered 64 MW of power during tests.

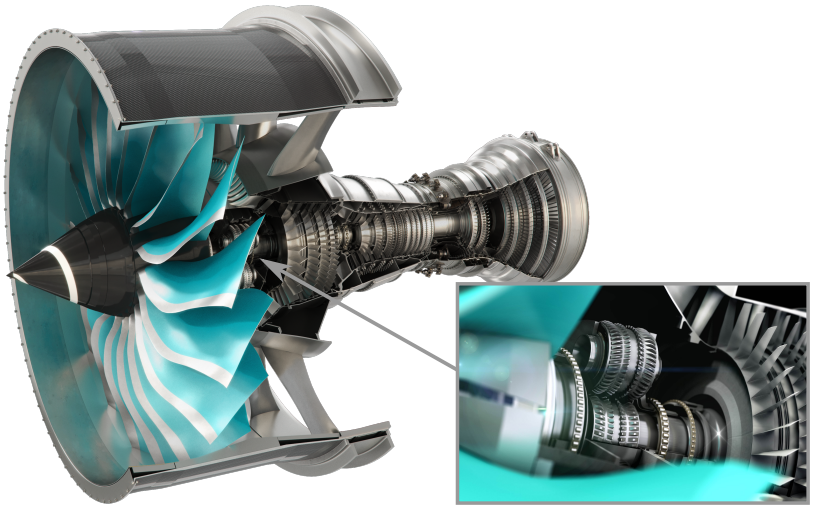

Figure 1.1: UltraFan aero engine designed by Rolls Royce and detail of the planetary gearbox. Images courtesy of Rolls-Royce plc.

1.2. Heat exchangers

As previously explained, the new generation of turbofans is facing a challenge regarding thermal management and, hence, heat exchangers are becoming a key factor in their development. In these types of mechanical systems, where the thermal and aerodynamic components must be properly addressed, there exist complex coupled interactions. Their efficiency is determined by their ability to release the most amount of heat while causing the least amount of pressure loss to the flow. Additionally, it is also desirable to reduce their impact on noise emissions.

In this regard, an investigation of the aerothermal performance of heat exchangers mounted on the inner wall of the secondary duct of a turbofan is of great interest. The available surface is used by these heat exchangers as an interface between air and oil. To extend the contact wet surface, longitudinal fins can be added to the system to boost thermal performance. Such a design implies a significant trade-off between the improvement in heat exchanger thermal performance and the aerodynamic penalties, which are measured by drag or pressure loss.

Although they can be installed in other locations, Surface Air-Cooled Oil Coolers (SACOCs) are typically installed on the lip that divides the engine's bypass flow from the core flow. With little disruption and hence, little effect on specific fuel consumption (SFC), the SACOC is utilised to evacuate

a significant quantity of heat held in the oil into the bypass air stream, contributing to the engine's thrust by the Meredith effect (a typical example of this effect is the P-51 Mustang). The bypass mass flow that the fan delivers serves as a cold sink. This device, if placed between the fan and the downstream guide vane, can also help to de-ice the lip that separates the bypass flow from the core flow by effectively using the heat removed in the process.

SACOCs typically consist of parallel fins installed into the secondary duct of a turbofan's wall. Fins are positioned and geometrically shaped to maximise thermal exchange while minimising aerodynamic impacts (drag and noise increases). Fig. 1.2 shows a typical configuration of a SACOC with fins surrounding the outer wall of the secondary duct in a turbofan.

In comparison with other types of heat exchangers such as plate/tube ones, this arrangement generates fewer aerodynamic disturbances. If no fins are added to the heat exchanger, the measured mean total pressure losses may decrease in the order of 1%, but a considerably larger decrease in heat exchange is also observed [15].

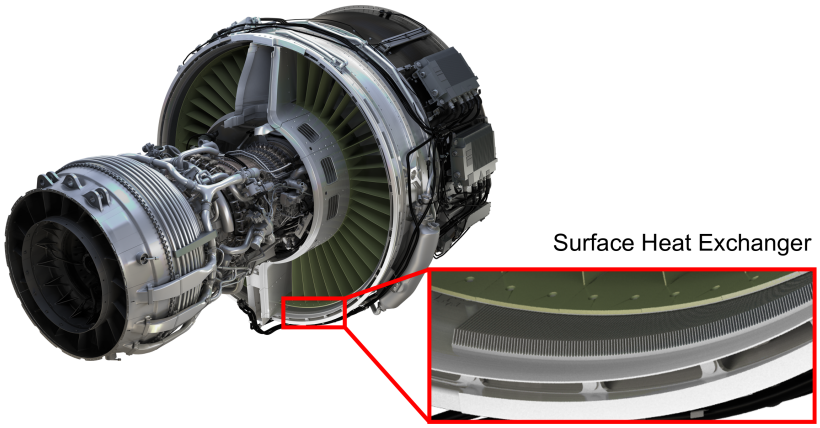

Figure 1.2: Turbofan Leap 1A which employs a SACOC with parallel fins around the outer wall of the secondary duct. Image courtesy of Safran Aircraft Engines.

1.3. State of the art

Considering the technological evolution that aero engines are recently undergoing, research on new ways of thermal management has become one of the main goals in their development.

Some of the studies are focused on numerical simulations and computational modelling to predict the final performance of heat exchangers to be installed in the engines. Additionally, other investigations have tried to address the experimental performance of such devices.

However, a major gap has been found during the development of this thesis regarding available literature, mainly caused by two factors. On one side, literature on turbofans' thermal management devices is rather scarce due to the general confidentiality of these topics, since they represent a key factor for aeroengine companies. On the other side, the complexity to reproduce realistic operational conditions and the high costs associated with in-engine tests make this topic hard to find in public research.

This doctoral thesis contributes to the state of the art of surface heat exchangers by proposing a robust experimental methodology which enables a better understanding of the coupled aerothermal processes that occur in these devices. The design of a specific facility to perform the studies with the possibility of tailoring the air velocity distribution around the heat exchanger, together with measurement procedures to capture relevant features of the cooling system are presented.

1.4. SACOC: A Clean Sky 2 project

The development of this doctoral thesis is linked to the Clean Sky 2 project Aerodynamic upgrade of Surface Air Cooled Oil Cooler (SACOC), Fig. 1.3.

Figure 1.3: SACOC logo

Clean Sky 2 is a European programme in which the European Commission and the EU aviation industry collaborate to lessen aviation's environmental impact by accelerating the development and adoption of cleaner air transport technologies. In this context, the SACOC project was raised by Safran Aircraft Engines, seeking to enhance the thermal management of new generation of turbofans.

The idea behind this project was to develop geometrical models of surface heat exchangers that could be installed in the bypass duct of the new generation of turbofan engines to improve their thermal management.

As previously introduced, thermal loads generated by this type of aero-engines reach values that become a limiting factor for these technologies. New and improved ways of cooling engine lubricants are a key challenge to overcome in order to generate a more sustainable aviation.

The consortium created for this project was composed of Safran and three partners: Universitat Politècnica de València (UPV), Universidad Politécnica de Madrid (UPM) and Purdue University. The main functions of each partner were:

- Safran: Company that proposed the project and defined the roadmap for the development of the technologies. Besides imposing the working conditions for the heat exchanger and defining certain needs for the company, Safran sought to develop a numerical model to predict the aerothermal performance of this type of heat exchangers with in-house tools.
- UPV: Main leader of the project in terms of coordination. The main contribution from UPV consisted of the experimental characterisation of heat exchanger geometries to validate the numerical models.
- UPM: Partner in charge of developing numerical simulations with commercial software to compare with the results obtained by Safran and gain a deeper insight into the aerothermal processes that undergo in these heat exchangers. UPM also contributed by generating a numerically optimised geometry to be analysed.
- Purdue University: Due to the large experience on heat exchangers of the university research group university, Purdue acted as an external consultant which provided feedback and performed complementary experimental tests in a scaled-up facility and parallel numerical modelling.

1.5. Objectives

There are different objectives that this thesis aims to cover which are not only related to obtaining accurate and suitable results, but to developing a robust methodology to experimentally characterise surface heat exchangers. The most relevant objectives are listed below:

- The experimental investigation of surface heat exchangers needs to be carried out in an adequate facility that is able to recreate relevant operating conditions. For this reason, one of the objectives of this thesis is to design a test bench to perform the required experiments under realistic conditions.

- One of the main goals of this research is to develop a complete, reliable and robust experimental methodology which is able to capture the main aerothermal performance of surface air-cooled oil coolers during their characterisation.

- Deriving key aspects of surface heat exchangers for turbofans is the ultimate objective of this investigation, performing a thorough analysis of the results obtained and identifying key performance indicators of these devices that lead to a better comprehension of the aerothermal processes which take place in surface heat exchangers.

- A final objective which is derived from the doctoral thesis development is the contribution to the general knowledge on this topic that has turned out to be rather scarce regarding the specific application of these devices in turbofans.

1.6. Thesis outline

The body of this doctoral thesis is divided into seven chapters and an extended bibliography collection at the end of the document.

This first chapter provides a contextualisation of the work carried out during the doctoral thesis, explaining the actual situation of heat exchangers in the frame of aviation engines and turbofans. The contributions to the state of the art in this regard are presented and the main objectives of this investigation are explained.

Chapter 2 gathers a complete and thorough review of relevant investigations of related topics for this research. It includes works not only on what to consider in a heat exchanger design and how its geometry impacts the results, but also on what kind of techniques are adequate to characterise them experimentally and how to perform correct measurements in wind tunnels.

The following chapter, Chapter 3, explains in detail the methodological procedures used in the experimental characterisation. Firstly, the facilities used are presented, explaining also the reasons behind their design. Then,

the instrumentation employed is introduced, followed by the data acquisition and reduction procedures and the uncertainties associated which each measurement.

After that, Chapter 4 focuses on how to develop an automatised process to generate distortion screens which can modify the velocity distribution in a wind tunnel. The model and how the geometry is generated are firstly explained, followed by numerical simulations which analyse in a first attempt the results obtained. Finally, the model is validated with experimental measurements.

Chapter 5 presents the results obtained when applying intrusive measurements during the aerothermal characterisation of four different geometries of surface air-cooled oil coolers. Aerodynamic and thermal results are compared to determine the impact of the geometry on the results. Also in this chapter, the effect of introducing a distortion screen to reproduce a realistic velocity field around the heat exchanger is assessed.

The next step in the investigation, Chapter 6, consists of applying optical techniques in the characterisation to cross-validate the previously obtained results with intrusive methods, providing also complementary information that is not available otherwise. The outcomes are divided into aerodynamic and thermal results too. The feasibility of using additive manufacturing to perform a rapid and preliminary aerodynamic characterisation of surface heat exchangers is also investigated.

To sum up, Chapter 7 gathers the main conclusions extracted during this doctoral thesis in terms of methodological procedures and results obtained. Moreover, interesting and relevant future works are proposed to complete the results obtained and extend the knowledge on topics related to this investigation.

CHAPTER 2

Literature review

In order to contextualise the work presented here and to gain a deeper insight into the approaches utilised in this area, a literature review is presented in this chapter. Since the major part of the research is from an experimental perspective, special care has been put into the procedures to characterise heat exchangers from an aerodynamic and thermal point of view. It is important to note that the context is related to heat exchangers in turbofans, so a good number of references also deal with problems related to aero-engines.

Furthermore, as previously explained, one should not forget that the presence of a heat exchanger in the bypass duct of a turbofan has an impact on the airflow which may incur a diminishing of the engine's propulsive efficiency. For this reason, a thorough investigation of the impact of the geometry on the performance of a heat exchanger needs to be accomplished.

Complementary, it is important to consider the advantages provided by numerical simulations which give a more complete vision of the physical phenomena that take place in the heat exchanger: flow behaviour, interaction with the studied models, thermodynamic processes... It is nevertheless crucial to validate these results against their experimental counterparts to make sure the outcomes are somehow trustworthy.

Finally, not only operating a wind tunnel and recreating adequate flow conditions is essential in an experimental characterisation, but also different measurement techniques need to be known and understood. Hence, the proper choice can be made when analysing which one is more suitable to determine a particular characteristic of the studied model, as well as its strong points and main limitations compared to other techniques.

2.1. Design and performance of heat exchangers

The design of any heat exchanger should be focused on the specific application it will be used for. Nevertheless, there are always two goals to be accomplished in their performance: on one hand, their most desirable feature is their ability to extract heat from a hot source and deliver it to a cold sink. However, there is a second requirement that is crucial in some circumstances: the pressure drop. The consideration of these two aspects makes the design of heat exchanger geometries a challenge for engineers, as the improvement of one usually implies a worsening of the other.

In the case of the aerospace industry, it becomes a real issue because more complex thermal management systems need to be designed for the new generation of turbofans [16–18], so additional cooling systems have to be implemented, considering though that their impact should be minimum in terms of affecting the propulsive efficiency. In fact, companies are developing patented technologies in this respect [19, 20] to improve the performance of UHBR turbofans.

There is also another concern in the aerospace sector to be aware of: weight. Filburn et al. [21] developed a carbon-carbon finned heat exchanger which reduced the original weight of an aluminium heat exchanger to 53% of its value. The use of additive manufacturing also helps in the design of compact, lightweight and efficient heat exchangers [22]. In this aspect, Klein et al. [23] and Huang et al. [24] carried out a review on printed heat exchangers, focusing on the manufacturing techniques the former and on their performance the latter. 3D printing can be also used to enhance heat transfer [25–28] by adding vortex generators, wavy inserts, complex geometries and so on.

One of the main disadvantages though of this type of manufacturing is the impact of the finishing. Vafadar et al. [29] compared the performance of three pairs of different geometries built by milling and direct metal printing, discovering that the surface finishing plays a key role in the results and finding more discrepancies as the air mass flow increases. Saltzman et al. [30] were able to improve the heat removal by up to 14% by testing an additive manufactured heat exchanger, but with a decrease in its aerodynamic performance, almost doubling the induced pressure drop.

The performance of any heat exchanger need to be addressed adequately, so an appropriate metric should be used. Adams [31] and Doo et al. [32] used factors such as the Colburn j factor and the Fanning friction coefficient f, or the area and volume goodness factors, to examine the aero-thermal performance of surface heat exchangers with different shapes.

Since it is of extreme importance to consider the pressure drop caused by the heat exchanger in some scenarios, Dube et al. [33] developed a statistical model that could predict it depending on the main parameters of the heat exchanger such as fin density, height or thickness, among others. This is because a great part of the energy loss produced by a heat exchanger is closely related to flow-solid interaction. However, the complex mixing of the flow can become very important. Doo et al. [34] assessed the pressure loss mechanism inside a cross-corrugated plate-type heat exchanger using the volumetric entropy generation rate.

In order to obtain a better performance of the exchangers considering the pressure drop, different shapes and arrangements of fins have been investigated. Bonjakovi et al. [35] could raise the heat exchange by 39.3%, reducing 23.8% the mass flow with a star-shaped fin shape instead of regular annular fins. With airfoil-shaped fins instead of zigzag channels, Zhang et al. [36] could reduce by 1/6 the pressure drop. Gong et al. [37] simulated numerically V-shaped oblique wavy surfaces and obtained the best configuration in terms of pressure loss and heat exchange by changing their geometric parameters and obtained an increase in goodness factor of 16% compared to a flat plate. Chávez-Modena et al. [38] were able to gain a pressure drop reduction of 10.6% with a negligible heat transfer variation by topologically optimising the geometry of a heat exchanger with standard trapezoidal fins.

Apart from the two main concerns when considering the design of a heat exchanger, there are other aspects to bear in mind, like the fluid-structure interaction. Zhang et al. [39] proved that the greater thermal and mechanical stress that finned heat exchangers had to withstand were encountered for large fin offsets and thin fins configurations.

Although several fundamental studies on surface heat exchangers have been conducted, they are usually done under ideal heat transfer conditions. Nevertheless, when considering where the heat exchanger is going to be located and the conditions it will be operating under are defined, it is important to take them into account [40, 41]. This is the case of heat exchangers located in the bypass duct of a turbofan.

Focusing on Surface Air-Cooled Oil Coolers (SACOCs) whose main purpose is to be installed in the bypass duct of turbofans for oil refrigeration, there are two possible options: locate them upstream or downstream of the Outlet Guide Vane (OGV) of the engine. For the first case, Villafañe and

Paniagua [42] developed a facility at the von Karman Institute for Fluid Dynamics which can replicate the swirl conditions that are typically encountered downstream of the fan in the splitter region.

With that installation, they could evaluate the aerothermal performance of heat exchangers that featured continuous and interrupted fins. Sousa et al. [15] utilised the same facility to carry out an inverse heat transfer analysis of the extracted heat from the heat exchanger, observing that up to 76% of the take-off cooling demands of a modern turbofan could be achieved with a correct heat exchanger design.

The facility where these investigations took place is shown in Fig. 2.1. It is possible to observe the complex design needed to reproduce the flow swirl upstream of the OGV.

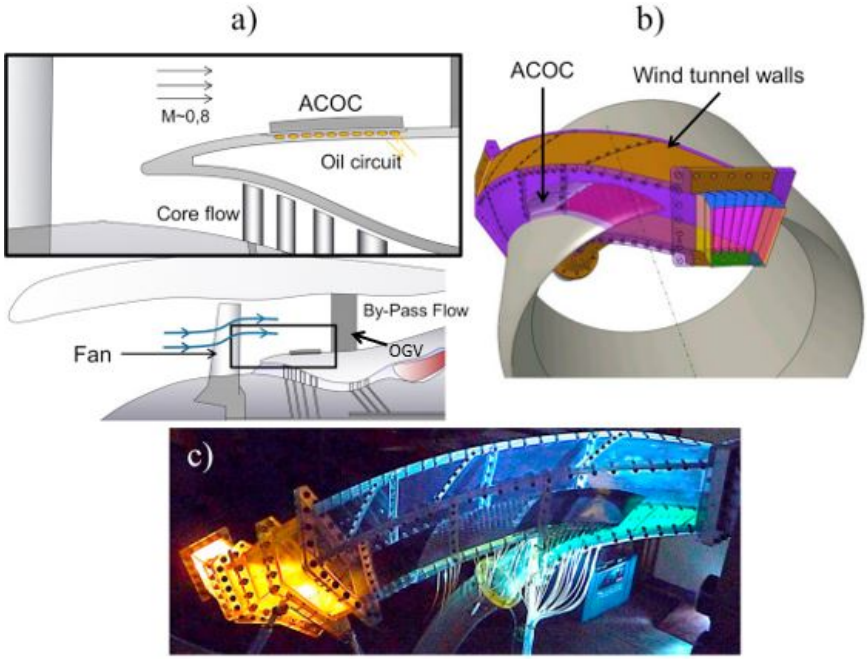

Figure 2.1: Facility to study the aerothermal characterisation of Air-Cooled Oil Coolers (ACOC) upstream of the OGV at the von Karman Institute for Fluid Dynamics [15].

Placing the heat exchangers downstream the OGV of modern high-bypass-ratio turbofans is however more typical, like the cases of the CFM LEAP-1A and the Rolls-Royce Trent XWB. In this regard, Kim et al. [43] performed a numerical analysis which was then experimentally validated with a single-

fin heat exchanger which was placed in different axial positions inside a groove of the duct to determine its thermo- aerodynamic performance. Additionally, the study was extended by Kim et al. [44] analysing the behaviours of different plate- and pin-fin geometries under similar conditions.

Although there is a large number of experimental investigations on finned heat exchangers, the literature on this type of technology to be implemented in turbofans is very scarce. One of the main reasons for this is the large amounts of air mass flows and high speeds required during the experiments. This problem was tackled by Kim et al. [43] by engineering a very narrow wind tunnel and a single-fin heat exchanger, assuming then periodic conditions.

There is nevertheless a major limitation with this approach: SACOCs only occupy a portion of the engine periphery. Besides, the lateral boundary layer control in narrow wind tunnels so the fins can be considered under periodic-like conditions can be complicated. Hence, it might be preferable to study at least a few fins with a certain separation from the lateral walls.

However, this implementation could lead to prohibitive amounts of air mass flows for a complete height of a turbofan, so a scaled wind tunnel with a reduced height is desirable. With this new approach, the issue of reproducing the flow conditions around the heat exchanger becomes a new challenge to tackle. Gelain et al. [45] demonstrated the need of accounting for one-dimensional velocity variations in this type of arrangement to obtain reliable results. For this reason, it is of remarkable importance to be able to modify the incoming airflow field during the experiments and replicate a target velocity distribution.

2.2. Influence of heat exchanger geometry

It seems obvious that the geometry of the heat exchanger plays a key role in its performance. For this reason, it is imperative to determine the conditions it will be working under and the main purpose of its application in order to select the most appropriate. Guo et al. [46] designed an algorithm to select the best design, regarding the volume of the heat exchanger, from a pre-existing device list depending on the concrete application. The principal parameters that define the goodness of a heat exchanger are, on one hand, its ability to exchange as much heat as possible and, on the other hand, inducing the minimum pressure reduction in the working fluids [47]. On many occasions, they can be found as Colburn j factor and Fanning friction coefficient f.

In order to predict these factors, Manglik and Bergles [48] derived a series of empirical models based on the operational Reynolds number and the heat exchanger geometrical parameters, depending if they were working in laminar, turbulent or transitional flows.

The analysis of the geometry impact on the heat exchanger performance has been considered from different approaches. One of the first studies that compared in-line and staggered pin geometries was performed by Sparrow et al. [49] where also different heights of the pins were tested, concluding that the in-line geometries could exchange more heat for a fixed pump power, whereas the staggered configuration was able to reach a certain target exchange with a smaller size. Investigations alike were carried out by De Losier et al. [50], Jeng and Tzeng [51] and Wang et al. [52], where they compared pin sizes, shapes and locations with similar findings: the staggered configuration rises the pressure drop, but also increases the heat exchange. In other similar studies, Soodphakdee et al. [53] and Jonsson and Moshfegh [54] included, among different shapes, heat exchangers with continuous fin configurations and determined that their pressure loss was minimum, but also was the heat release.

Going a step further, Wong et al. [55] introduced Selective Laser Melting manufacturing in order to test innovative and complex structures of heat exchangers. One of the main outcomes of their study is the importance of a careful design for an adequate interaction between the exchanger and the fluid. Besides, as previously commented, the finishing of additively manufactured heat exchangers generally gives rise to a poorer aerodynamic efficiency [29, 30].

Other studies have focused on varying a preexisting geometry in order to improve the performance. Leon et al. [56, 57] analysed in-line and staggered fin geometries, both numerically and experimentally, and determined that, for Reynolds numbers higher than 800, using rounded edges in the leading edge was advisable. The same result was obtained by Limbasiya et al. [58] in an analogous study, but including that a better performance could be achieved with conical geometries in the range of Reynolds between 450 and 900. Krishna and Dineshkumar [59] conducted a numerical investigation that led to a result in which, although employing fins with blended leading and trailing edges improved the performance too, pressure drop and heat exchange presented better results using a dimpling leading edge. Moreover, Saleha et al. [60] proved numerically a rise in heat release in a heated wall-mounted cube by just adding a chamfer to the upper edges of a straight cube.

Doing a topological optimisation of a standard fin geometry, Chávez-Modena et al. [38], in the frame of the SACOC project (section 1.4), found a shape for the fin which maintained the heat exchange specifications of the standard geometry, but improved the pressure loss by 10.6%.

In terms of new geometries, Tang et al. [61, 62] added and optimised an arrangement of vortex generators prior to the heat exchanger that increased the original heat release, but also rose slightly the friction factor, obtaining the best results with long and low vortex generators at high angles. The use of S-shaped interrupted fins for heat exchangers was analysed experimental [63] and numerically [64]. In the experimental work, they determined relations for the pressure drop and the Nusselt number with the Reynolds and Prandtl numbers. Numerically, they parametrically studied the effects of fin angle, guide wing, fin width, fin length, and fin roundness seeing that, with this configuration of fins, rounding both leading and trailing edges caused 30% more of pressure loss. This outcome was also found by Zhang et al. [65] when comparing wavy fins with sharp and rounded edges.

However, it is important to consider that all studies discussed in this section so far (aside from the one by Chávez-Modena et al. [38] performed for the Clean Sky 2 project) were carried out with Reynolds numbers lower than 25 000 (even in the order of 500 sometimes), whereas typical figures in modern turbofan operating conditions can be in the order of 700 000. Furthermore, Michna et al. [66] found that correlations derived from these investigations and the predicted pressure drops and heats exchanged suffer a change in trends above values of Re in the order of 20 000 – 40 000, so no simple extrapolations can be used under these circumstances.

For heat exchangers working at higher Reynolds numbers, Cohen and Bourell [67] carried out a study on the performance of 21-pin geometries with Re up to 48 000. Overall, regarding the heat transfer, the straight geometries performed better, whereas the best pressure drop performance was achieved with tapered configurations. They found that the geometry with the highest aspect-ratio teardrop-shaped fins was the best solution. Another investigation that rose the Reynolds up to 100 000 was performed by Jaswal and Ames [68]. They compared a high solidity pin pedestal with circular pins against one with rounded diamonds in a channel with constant height and another converging one, seeing that the main effect came from the contraction in the section and not particularly from the shape of the fins, with 6% decrease in heat transfer with the converging channel.

2.3. Experimental characterisation of heat exchangers

The use of appropriate experimental techniques for the characterisation of models is essential to obtain reliable conclusions. Typically, when a certain device is being designed, numerical models are employed to determine its performance in a first step, but these models have to be experimentally validated before incorporating the device into complex systems. Besides, there are times in which the characterisation has to be done to confirm the proper functioning of the device during maintenance inspections.

In addition to the aforementioned points and considering ideas stated in this chapter, full-scale engine tests are time-consuming and expensive, so scaled versions to be tested in wind tunnels are desirable. However, it is crucial that the conditions in the wind tunnel match as closely as possible the flow field of the real conditions. In the case considered in this thesis, those in the bypass where the surface heat exchanger would be located.

Depending on how the measuring interacts with what it is measured, techniques can be divided into two groups: intrusive and non-intrusive measurement techniques. Focusing on aero-thermal characterisation, intrusive methods use probes embedded within the fluid they are meant to measure. For instance, to determine the velocity of the flow with a Pitot probe, it has to be introduced in the stream, as well as in the case of thermocouples to determine the temperature.

On the other hand, non-intrusive measurement techniques, also called optical techniques, do not need to physically interact with the object to be measured, but use optical devices (like cameras) able to capture the phenomenon to be determined. Sometimes, these systems need a light source to enhance the visualisation of the effect. Although non-intrusive techniques are typically more complex to configure, more expensive and need optical accesses to perform the measurement, they are widely used since have the great advantage of not interfering with the flow. This gains great importance when scaled-down tests are conducted, since intrusive methods could interact with the measurement and distort the final result.

There are a huge number of measurement techniques that depend on what phenomenon is wanted to analyse. For example, in hypersonic wind tunnels [69–71] it is typical the use of Optical Emission Spectroscopy (OES) with micro-wave diagnostics or Diode Laser infrared Absorption Spectrometry (DLAS) to determine the plasma characteristics, electron number density, velocities and temperatures.

To monitor the flow distribution in multi-phase heat exchangers on duty non-intrusively, Oriol et al. [72] developed a method to characterise the mal-distribution of the flow which used an optical sensor associated with a liquid phase tracer, so fault diagnostics can be produced.

Rightley et al. [73] also used a specific dye to characterise the performance of a direct absorption solar receiver varying the thickness of the particle curtain and analysing their extinction coefficient.

Other laser-based techniques for aerodynamic characterisation have been used by Iungo [74], who employed wind Doppler Light Detection And Ranging (LiDAR) to characterise the wake of a wind turbine in a wind tunnel, or Olson et al. [75], who used Single-component Molecular Tagging Velocimetry (1c-MTV) to analyse the flow separation above airfoils.

There are many techniques which use the Doppler effect as a measuring element, but Laser Doppler Anemometry (LDA) is one of the most popular. It uses the Doppler effect to determine the velocity by intersecting in a punctual region two laser beams that interact with each other and create a fringed pattern in the control volume. Then, as particles pass through that illuminated spot, they blink at a frequency that depends on their velocity and the space between the fringes in the control volume. By creating a known spacing between the fringes, the velocity of the particles can be derived.

Buresti et al. [76] obtained the velocity field and turbulence of a coaxial jet by means of LDA and hot-wire anemometry, applying intrusive and non-intrusive techniques to cross-validate their results and obtain further information on its behaviour. Scrittore et al. [77] used LDA to analyse the flow behaviour in film-cooling when going through dilution holes in combustors. One of the advantages of LDA is the possibility of measuring in precise locations of difficult access, so Lee and Kwon [78] and Dong et al. [79] employed the LDA to characterise the flow field between rods and interrupted fins. Two works of Gertzos and Caouris [80, 81] employed LDA measurements for CFD validation in the aerodynamic characterisation of a collector storage solar water heater. Saltzman and Lynch [82] utilised the capabilities of this technique to locate the region where a printed heat exchanger with large roughness presented the transition between laminar and turbulent regimes, compared with a traditionally manufactured one.

Another even more common technique that is based on a laser is Particle Image Velocimetry, PIV. The idea behind this technique is based on comparing the relative displacement of seeding particles between a couple of frames in a section illuminated by a laser sheet pulse. Thus, considering

the time delay between both pulses and quantifying the displacement between the frames, the velocity field can be derived. It has the advantage, compared to the LDA, that is able to provide the velocity field of a much wider region in a single measurement, although, in general, the acquisition frequencies are lower.

Vitillo et al. [83] combined LDA and PIV measurements to determine mean velocities and fluctuations (along specific profiles the former and in wider regions the latter) and validate hence a numerical model for compact heat exchangers channels of innovative geometry.

Wen et al. [84] determined the flow field around a plate-fin heat exchanger using PIV and were able to design an improved header configuration that enhanced the heat exchanger performance. Yataghene et al. [85] and Yashar et al. [86] conducted similar studies characterising the flow field in heat exchangers with PIV. The nature of the measurement technique allowed Naterer and Adeyinka [87] to employ PIV data to develop a model to determine energy losses and local entropy production.

Particle Image Velocimetry measurements are usually taken together with other complementary techniques at the same time. As some examples, Jaíková et al. [88] and Amiri et al. [89] carried out Planar Laser Induced Fluorescent (PLIF) to track the temperature field in heat exchangers while characterising the flow field with PIV simultaneously. Bencs et al. [90] also completed PIV measurements with a synchronised Background Oriented Schlieren (BOS) to determine the flow field around a heated cylinder.

A more qualitative technique for flow visualisation is Schlieren. It consists of taking advantage of the modifications produced in the refractive index of a fluid when its density changes. Thus, when a region where the refractive index varies is illuminated with parallel light beams, their direction will be shifted, creating shades in the image. Although sudden pressure variations like those produced in shock waves modify the flow refractive index and can be clearly seen with Schlieren [91], the changes in temperature also affect it. A very clear example can be seen in the work of Mullisen and Loehrke [92], that visualised the flow in heat exchangers with interrupted fins.

Since the Schlieren is primarily for qualitative visualisation, it is usually complemented with other techniques. Jarosinski [93] also applied PIV and interferometry to completely characterise the velocity and temperature fields above a heated rib-roughed wall under steady and pulsating flow conditions. Rajput and Srivastava [94] completed their Schlieren measure-

ments with laser-based interferometry to derive the flow thermal boundary layer and heat transfer coefficient at different Reynolds numbers in compact channels.

When a hot source is present in the experiments, it is typical to use infrared (IR) thermography too, characterising thus the temperature distribution of the body surface. Leblay et al. [95] developed a methodology based on IR thermography to determine heat exchangers performance by means of a rapid calculation of the local heat transfer coefficient.

Somasundharam and Reddy [96] characterised the thermal properties of an orthotropic material employing IR measurements. Mobtil et al. [97] utilised IR thermography to inversely derive the heat transfer in transient conditions in a fin and tube heat exchanger.

Table 2.1: Synthesis of different optic measurement techniques for the aerothermal characterisation of heat exchangers found in the literature, including type of measurement and main outcome.

Reference	Measurement	Outcome
Buresti [76]	LDA+HWA	Velocity field and turbulence
Dong [79]	LDA	Flow field between interrupted fins
Gertzos [80]	LDA	Aerodynamic validation of CFD
Saltzman [82]	LDA	Transition laminar - turbulent regimes
Vitillo [83]	LDA+PIV	Mean velocities and fluctuations
Wen [84]	PIV	Flow field to improve header
Yataghene [85]	PIV	Complete flow field inside a SSHE
Jaíková [88]	PIV+PLIF	Track velocity and temperature field
Bencs [90]	PIV+BOS	Flow field visualisation
Mullisen [92]	Schlieren	Flow visualisation between interrupted fins
Jarosinski [93]	PIV+Sch.+Interf.	Velocity and temperature fields
Rajput [94]	Sch.+Interf.	Thermal boundary layer and h
Leblay [95]	IR thermography	Calculation of the local h
Mobtil [97]	IR thermography	Derivation of the inverse heat transfer

Table 2.1 collects the most relevant investigations on the aerothermal characterisation of heat exchangers which employ different non-intrusive techniques. Some of them use a combination of several methods for a more complete characterisation.

2.4. Characterisation in wind tunnel

Experimental characterisation plays a key role in the development of new products, but full-scale tests, for example, in engines, are expensive and time-consuming. For these reasons, the characterisation of models in scaled

wind tunnels is a desirable option during the first steps of their development. However, there can be many situations in which laboratory conditions are no longer representative of the study of an actual application. Regarding internal aerodynamics, for example, not too many scenarios can be reproduced by the uniform flow in a wind tunnel and used to evaluate the aerodynamic performance reliably.

This is because wind tunnels use devices to reduce their turbulence [98, 99] and, thanks to that, certain conditions such as reproducibility [100] can be achieved. According to Barlow et al. [101], the variation from the mean velocity in a test section of a low-speed wind tunnel is typically within the range of 0.2-0.3%.

2.4.1. Flow distortion

One of the areas more susceptible to flow distortion impact is the intake of gas turbine engines. This is because of the distorted velocity distribution effect on the performance of the axial compressors, which are placed in the upstream-most position of the engine. There are two main types of instabilities that may occur in an axial compressor [102]: surge, manifested as annulus-averaged flow oscillations, and rotating stall, which appears as wavelike perturbations which travel circumferentially around the annulus.

Yu and Liu [103] performed S-PIV measurements in a low-speed large-scale axial compressor working under distorted flows to reveal some complex flow features that occur inside. The influence of circumferential distortion was studied by Toge and Pradeep [104], finding that an earlier stall was produced when the flow was distorted and that, due to the interaction between the tip leakage vortex from the first stage and the original distorted flow, the effect was amplified in the second rotor. The radial distortion was investigated by Li et al. [105], introducing two lattice rings in their facility. If the distortion was close to the tip of the blades, it increases the stall inception to longer-length scales. An extensive review of the influence of flow distortion in compressor instabilities can be found in [106]. Moreover, flow distortion is not just a problem related to compressor malfunctioning, but also a source of noise emissions [107], modifying both tonal components and broadband noise.

To be able to detect these instabilities before they induce any type of failure is of high importance. Lin et al. [108] generated a method based on deterministic learning able to identify rotating stall several revolutions before the actual stall happened. Salunkhe et al. [109] did something alike too by developing co- and counter-rotating distortions feedback control strategies.

There is an inclination these days that leads to more integrated systems in aircraft, and a clear example is the installation of embedded propulsion systems within the airframe. However, by doing this, these types of engines present certain disturbances at the aerodynamic interface plane, caused by the complex geometries of their intakes.

Besides, the integration within the airframe also implies a higher interaction between aircraft and engine [110]. As consequence, there are several studies focused on the analysis of the flow behaviour downstream of these intakes [111, 112] and the effects of boundary layer ingestion [113–118] or even vortex ingestion [119, 120]. One example of how to control and reduce the circumferential distortion caused by these situations was provided by Gorton et al. [121], who were able to reduce the DC60 descriptor [122] from 29% to 4.6% using less than 1% of inlet mass flow by means of a mass flow pulsing actuator.

One of the challenges that the new generation of aero-engines are suffering recently, is the need for an improvement in the thermal management systems, so the heat absorbed by the lubrication circuit in geared turbofans can be released [16]. This can be achieved by the addition of surface air-oil heat exchangers in the secondary flow of the turbofans, so the enthalpy available in the oil can be used by the air. Nevertheless, Gelain et al. [45] proved that, in order to reproduce the actual performance of the heat exchanger, the flow conditions in its surroundings needed to be replicated.

Another occasion where flow distortion has great importance is during take-off and landing, the most restrictive periods in the flight envelope of an aircraft. Indeed, the air that enters the engine is strongly affected by the atmospheric boundary layer, so Ameur et al. [123] analysed numerically the impact of this boundary layer on the aerodynamics of the wind-rotor/nacelle interaction.

2.4.2. Means to condition the flowfield

There are several ways to generate a prescribed boundary layer in wind tunnels but generally, flow conditioning can be achieved by three means: roughness elements added to the bottom of the wind tunnel, power control of fan arrays and distortion screens.

In large-scale wind tunnels, it is typical to use roughness elements such as wall-mounted cubes to reproduce atmospheric boundary layers. Maruyama et al. [124, 125] determined the adequate treatment of boundary conditions at the inlet and surface of the roughness elements in LES simulations, capturing the mean flowfield behaviour and low-frequency fluctuations.

Kozmar [126] studied experimentally two different conditions of turbulent boundary layers with different incoming intensities but the same non-dimensional thickness to study the effects of the pressure on the different sides of the cubes.

Hohman et al. [127] generated an artificially thickened boundary layer using a castellated barrier, elliptical vortex generators, and surface roughness in a relatively short wind tunnel. A similar approach was followed by Jafari et al. [128] to determine the correlation between the turbulence intensity created by this type of wind tunnel and the lift generated in a flat plate.

A more complete analysis was performed by Catarelli et al. [129] whose roughness elements, called Terraformer, could be adjusted in height and angle to tailor the atmospheric boundary layer.

Nevertheless, although roughness elements are useful for large-scale wind tunnels, they are limited to only reproducing boundary layers, i.e., the distortion is limited to the low region of the tunnel.

Another way to control the flow field distribution in a wind tunnel is by individually varying the power of the fans in an array configuration. Kikitsu et al. [130] could replicate turbulent flow in a wind tunnel adjusting six fans numerically with fluctuations up to 5 Hz. Nishi et al. [131] replicated not only a turbulent fluctuation, but a velocity distribution in a two-dimensional wind tunnel (eleven fans placed vertically).

This method can modify the flowfield vertically, but also a 2D adjustment can be performed. However, it is only applicable in wind tunnels which feature arrays of fans that can be individually controlled, and the variations with respect to a uniform velocity distribution are few.

Considering the limitations of these two methods, if the flow field to be reproduced is complex and needs to be implemented in a small-scale wind tunnel, the use of distortion screens or distortion panels is the best option. Table 2.2 presents a summary of the main advantages and limitations of the conditioning methods.

Using distortion screens is indeed a widely spread manner to create targeted pressure distributions in flow rigs or wind tunnels. Basically, a distortion panel (or distortion screen) is a mesh placed perpendicular to the flow direction with variable porosity. The fact that the porosity is not uniform causes a total pressure drop which depends on this porosity distribution, generating hence the pursued pressure distribution downstream. For this reason, the relation between the porosity and the pressure drop is one of the most important aspects to consider [132].

Owen and Zienkiewicz [133] reproduced a uniform shear flow by varying the space between parallel rods which was very similar to the predicted theory, finding also that the trend did not decay downstream the screen. Something similar was done more recently by Phillips et al. [134], who employed an array of flat plates vertically separated a specific amount to recreate a determined vertical pressure gradient. A similar approach was taken by Yusoof et al. [135] in ground test facilities for gas turbine engines, where a series of radial and circumferential strips with different widths were used to modify the flow, achieving a root-mean-square error of 5.06% for the Mach distribution.

A series of theoretical approaches to predict the behaviour of distortion panels have been developed. Several of them, which consider the distortion panel as a group of aerodynamic sources with a prescribed strength which interact with the flow and produce the pressure drop, were collected by O'Neil [136]. Steiros and Hultmark [137] extended the Koo and James model [138] to obtain a better reproduction for low porosities when tested in a water channel by means of a base-suction term. Schneck et al. [139] developed later an analytical model that correlates the drag experienced by the flow when going through a cell of the panel with the pressure drop induced, depending on the panel porosity.

In terms of when the modified velocity is settled downstream of the screen, Stephens et al. [140] showed that, at distances of about one hydraulic diameter, the velocity field was already very similar to the final distribution achieved. Sivapragasam [141] conducted a more detailed investigation and determined that the pressure field and its gradients between two and five diameters downstream remained almost unchanged, whereas the variations were larger for shorter distances.

Table 2.2: Comparison of the different flow conditioning methods highlighting their advantages and main limitations.

Method	Advantages	Limitations
Roughness elements	- Applicable in all-size wind tunnels	- Only 1D control
Fan power	- Applicable in all-size wind tunnels - 2D control	- Small variations - Complex control
Distortion screens	- Complex flowfield control - Easy implementation	- Small-scale wind tunnels

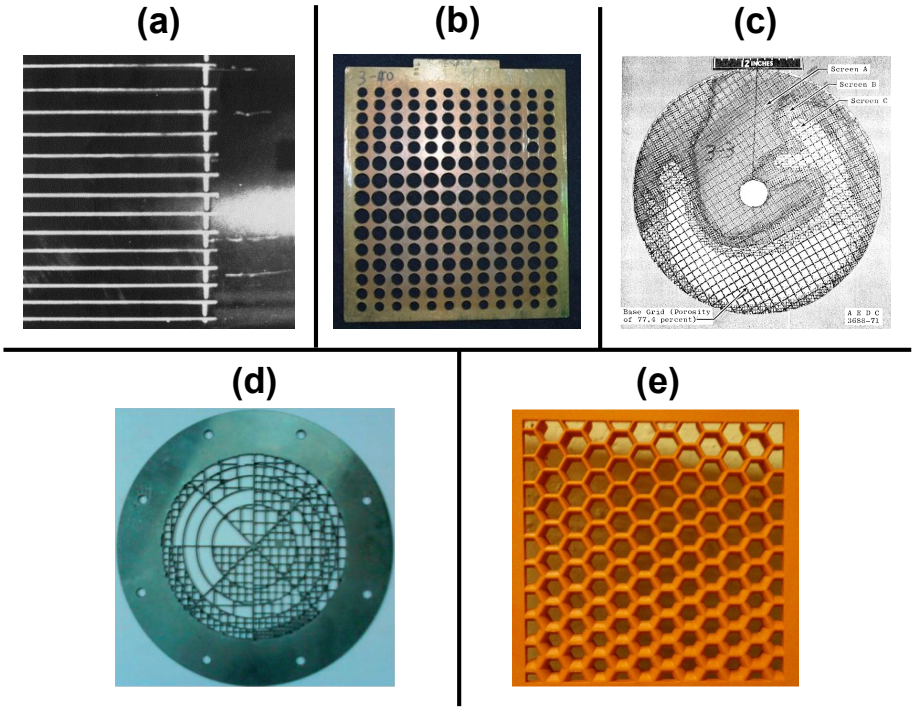

Figure 2.2: Examples of distortion screen manufacturing. (a) Rods with variable spacing [134]; (b) Perforated holes in plates [143]; (c) Superimposing metallic meshes [144]; (d) Water cutting [141]; (e) 3D printing [139]

Distortion screens have been applied to experiments following different manufacturing approaches. Some basic attempts were made using rods with variable spacing [104, 133, 134, 142], perforating plates with holes of different diameters [143] or welding and superimposing metallic meshes of different porosities [144, 145]. Other techniques for circumferential distortion panels are based on water cutting [141]. However, maybe the most complete and easy-to-implement is by 3D printing [112, 113, 120, 139, 140, 146].

Some examples of distortion screens manufactured using these techniques are displayed in Fig. 2.2. The rods with variable spacing were one of the first methods, together with the superimposition of meshes, which was more complex, but allowed finer tailoring in 2D. The water cutting and 3D printing, more modern, facilitate the manufacturing process, providing also a good bi-dimensional velocity distribution fit.

All previous examples consider subsonic conditions, but similar approaches can be taken for supersonic intakes. As some examples, Etheridge et al.[147] studied the effect of flow distortion in supersonic intakes generating shock waves to determine the impact on the mixing or combustion characteristics of premixed combustors, and Yu et al. [148] proposed and demonstrated a design method for direct-connect facilities that replicates the flow distortion in scramjet inlets, eliminating the problems occurring during the starting process of the facility.

2.5. Current knowledge limitations & novelty statement

The open literature presents a considerable amount of research and knowledge on surface heat exchangers, but it also has some limitations when considering their application to turbofans:

- The vast majority of the experimental research is focused on low Reynolds applications.
- Most of the investigations are limited to a single or few characteristics of heat exchangers.
- There is not an experimental facility where typical operating conditions of surface heat exchangers can be reproduced.
- When considering operating conditions at high Reynolds, investigations tend to perform only numerical simulations with no experimental validation.
- To perform flow distortions to match a targeted distribution, reported methods are either complex to manufacture or extrapolate from a specific facility and, in general, only account for boundary layers.

As stated in section 1.5, the present work aims to fill this gap in knowledge by:

- Designing a test bench to perform the required experiments under realistic conditions.
- Developing a complete, reliable and robust experimental methodology to characterise surface air-cooled oil coolers aero-thermally.
- Deriving key aspects of surface heat exchangers for turbofans.

- Generating an automatised method that is able to create velocity distortion screens automatically to alter the flow field bi-dimensionally.

2.6. Summary and conclusions

After reviewing a number of relevant studies related to the experimental characterisation of surface heat exchangers for turbofans, a series of conclusions can be derived:

- The two main characteristics to consider in a heat exchanger are its capacity to exchange heat between the cold and hot source and its induced pressure drop.
- There are different ways to improve the performance of a preexisting surface heat exchanger for its particular application. Typical efforts are focused on modifying the shape of the fins or their parameters such as height, width, number or orientation.
- Several studies have provided a thorough insight into the performance of heat exchangers, but the vast majority of the investigations are carried out under conditions of very low Re numbers compared to the actual specifications of surface heat exchangers for turbofans.
- Although a preliminary numerical characterisation based on CFD or mathematical models can provide a first idea of its performance, they always need to be validated experimentally. However, it seems interesting to develop an affordable methodology that avoids the extremely expensive and time-consuming in-engine campaigns.
- A proper selection of the experimental instrumentation plays a key role in the final results, since each technique features certain strengths and disadvantages compared to others. Besides, the complementary use of intrusive and optical techniques to cross-validate the results is desirable.
- Wind tunnel testing appears as the most obvious solution for experimental testing, but it is important to consider the real conditions the heat exchanger will be working under. In case the wind tunnel presents a smaller size than the real engine, as typically occurs, an adequate conditioning system based on distortions screens is needed.

CHAPTER 3

Methodology for experimental characterisation

One of the main objectives of this work has been the development and implementation of a reliable methodology to experimentally characterise surface heat exchangers for turbofans. In this chapter, the facilities used to carry out the experiments will be presented, together with the instrumentation employed during the characterisation.

Besides, the procedure followed in the data acquisition and reduction will be explained, as well as the uncertainty analysis that determines the accuracy limits of the measurements.

3.1. Facilities

In order to achieve similar airflow conditions to those typically found in turbofans, the High Mass-flow and High Temperature (HMHT) gas stand available at UPV is used to supply airflow in a scaled tunnel with a square test section. This test section is part of a bespoke rig that has been installed in the test room to conduct the experiments.

Work on this chapter has been partly published in the following papers:

- Experimental aerothermal characterisation of surface air-cooled oil coolers for turbofan engines [1]
- Numerical and experimental analysis of thermo-aerodynamic performance in an aero engine surface heat exchanger [7]

The rig includes: a settling chamber that dampens and reduces the turbulence created in the previous circuit, a transition to the test section, modules which generate a desired total pressure distribution, the test section with the heat exchanger, and an exhaust duct. Finally, the room has an extractor with a silencer to evacuate the flow.

There is also an oil conditioning system in the test room that allows full control of the oil circuit and configuring the desired oil mass flow and temperature.

3.1.1. Gas stand

The High Mass-Flow and High Temperature (HMHT) gas stand, Fig. 3.1, installed in the 8P laboratory of UPV, is a multipurpose experimental facility for aerodynamic studies that has been used in both automotive [149–151] and aeronautical engineering [1, 38, 152] research. It is capable of providing mass flows that can exceed 2 kg/s with cold air (between 30°C and 100°C) and hot flows with temperatures that can reach 1000°C with a flow rate of 0.3 kg/s by means of a 1 MW diesel continuous combustor.

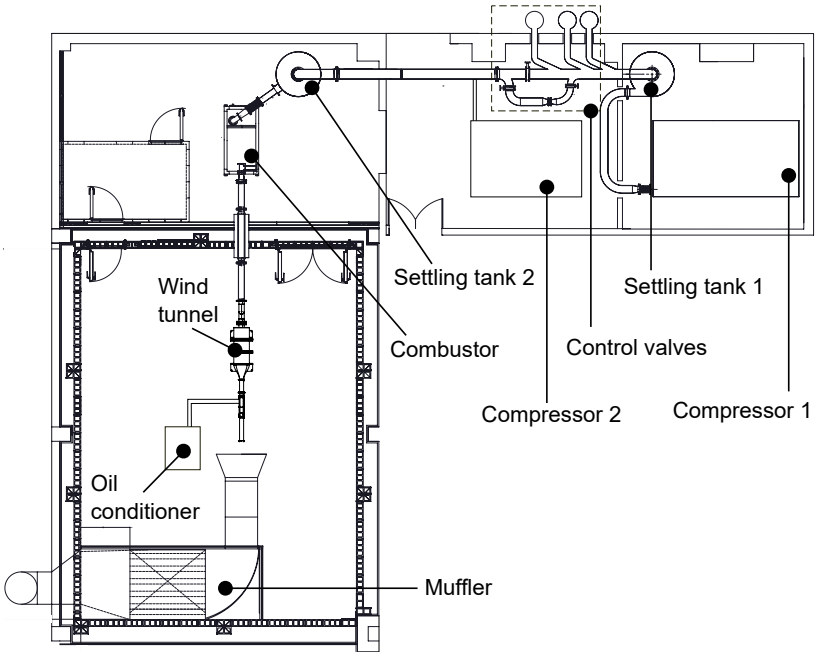

Figure 3.1: Schematic of the HMHT gas stand layout.

The continuous mass flow is delivered by an Atlas COPCO ZH7000-4-4.6 two-stage centrifugal compressor of 500 kW. It is capable of providing 2.15 kg/s with a pressure of up to 3 bar(A) and can reach a maximum discharge pressure of 5 bar(A) with 1.85 kg/s.

In order to regulate the total mass flow delivered to the test room, a series of venting valves are placed at the main pipe between two settling tanks. These reservoirs of 3 m^3 are capable of dampening sudden changes in the operating conditions, which helps to protect different parts of the facility and deliver a more uniform and controlled mass flow to the test room.

Since the air provided by the flow bench will be used as a cold sink to refrigerate the oil, temperatures must be reduced after the compressor. In normal operating conditions, the air leaves the compressor with temperatures around 100°C, so they need to be drastically reduced to reproduce the temperature conditions in the real case. To this end, an intercooler between the two stages of the compressor and an aftercooler downstream reduce the air temperature to ambient values.

Additionally, there is an extra compressor connected to the second settling tank that can deliver 0.5 kg/s with a maximum pressure of 9 bar(A). It can also be routed independently to the test chamber if multi-flow experimental setups are required.

3.1.2. Wind tunnel

A tailored modular rig, depicted in Fig. 3.2 and Fig. 3.3, has been installed in the test room to conduct the experimental characterisation of heat exchangers. At the beginning, a 0.26 m^3 settling chamber is installed, aiming not only to stagnate the fluid and reduce the flow turbulence, but also to straighten the streamlines upstream of the test section.

It is connected to the HMHT stand with an S-shaped pipe that delivers the flow inside the settling chamber through a specially designed pierced ending (based on Purdue's PETAL facility [153]) in a way that an adequate flow distribution in the test chamber is enhanced. Besides, there is a tap to connect a thermocouple and measure the reference temperature in this first stage of the rig.

One of the main features of this measurement is to perform air temperature corrections in the test section. When the conducted experiments take several minutes, or even hours, the air temperature is prone to change over time. This may occur because the air used comes in the first instance from the ambient, which can vary as the day advances.

Figure 3.2: Picture of the wind tunnel.

Another factor which may have a stronger impact on the temperature variations is the continuous functioning of the compressor. As it is running, it gets steadily warmer. Although this process is faster at the beginning (generally, the larger temperature variations occur during the first 30 minutes, approximately), the air does not reach a steady temperature at any moment. Considering this, a certain amount of time is left prior to the beginning of the tests, so variations are relatively low and can be corrected.

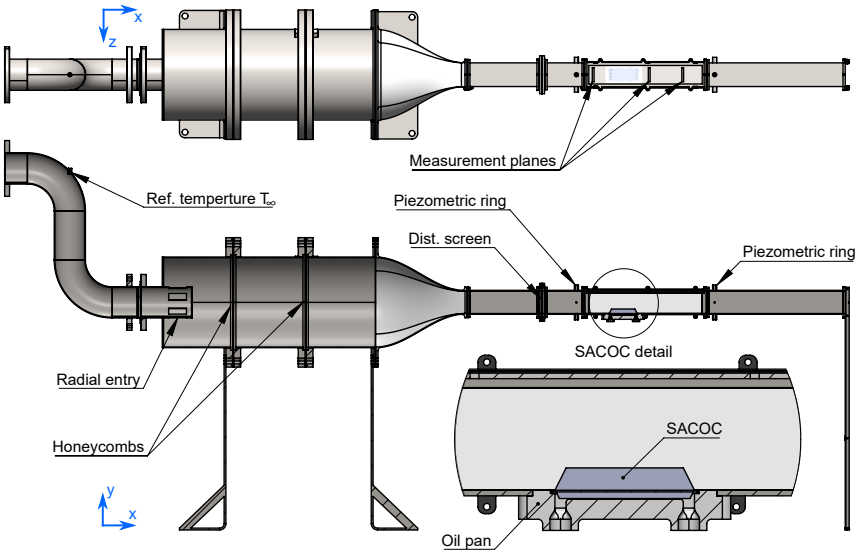

Figure 3.3: Drawing of the wind tunnel with main components and detail of the SACOC.

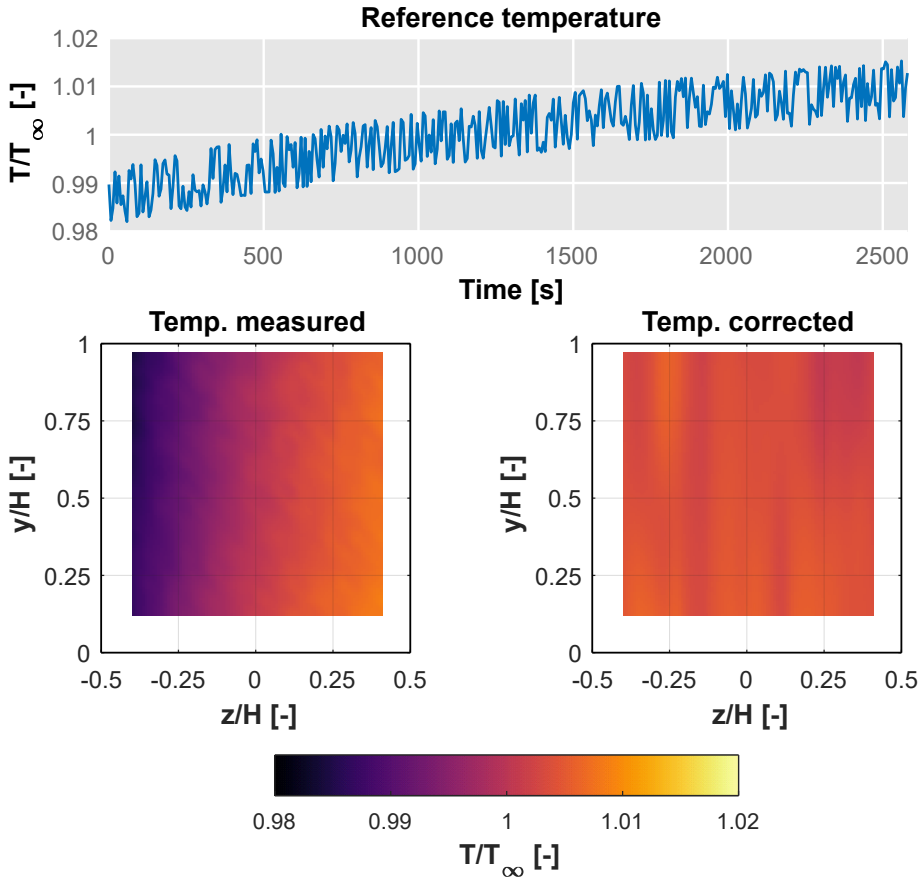

Figure 3.4: Evolution of the air temperature during the measurements. The upper plot represents the evolution of the reference temperature. The lower images display the temperature measured in the test section and the corrected temperature.

An example of how to treat the temperature measurements can be seen in Fig. 3.4. It shows, on the upper side of the figure, the evolution of the temperature values with time. It is possible to see that in a test that lasts more than 40 minutes, the temperature suffers a variation of less than ±2% with respect to the reference value T_∞, defined as the mean temperature during the test.

The figures at the bottom represent the temperature distribution in the test section. On the left, one can observe the actual temperature measured in the test section and how there appears to be a temperature gradient between the left and the right walls.

This is because the procedure to measure the section begins in the top-left corner and advances towards the bottom-left corner. Then, it moves slightly to the right and measures again from the top to the bottom, until it reaches the bottom-right corner, where it finishes.

Considering this and the temperature evolution in time, it is possible to conclude that the gradient observed in the bottom-left image of Fig. 3.4 is caused by the warming of the incoming air rather than by a physical phenomenon in the test section.

For this reason and to insulate the effects of the heat exchangers in the test section, it is possible to correct the measured temperature with the mean value during the tests. The image in the bottom-right of Fig. 3.4 represents the corrected values of the measured temperature (image at its left), showing a rather uniform distribution.

Note that this procedure has been followed when tests last for too long to consider a steady temperature and for comparison purposes. It is not used when the actual air temperature needs to be considered to derive a particular variable (e.g. the convective heat transfer coefficient h).

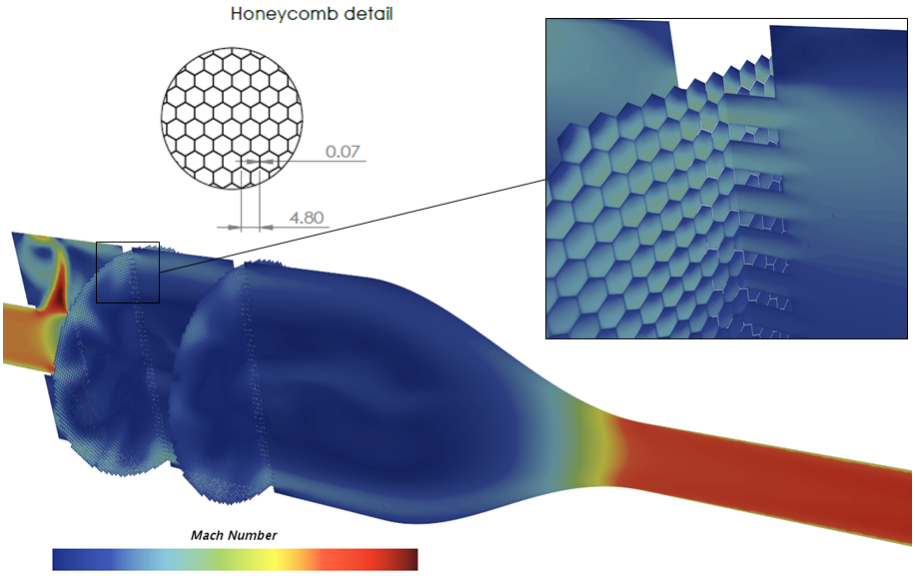

Figure 3.5: Numerical simulation of the velocity in the final configuration of the settling chamber.

In order to achieve better flow conditions in the test section, two honeycomb straighteners are placed downstream of the end of the pipe, being regular hexagons of 2.77 mm of side and 0.07 mm thick. The total thickness in the flowise direction of each honeycomb is 24 mm. The results of the flow velocity field with the final layout obtained by using numerical calculations can be seen in Fig. 3.5.

A 3D-printed transition with an area ratio reduction of 12.57 is set after the settling chamber to gently lead the flow into the squaredpipe upstream of the test section. To avoid flow detachments, the interior surface of the transition has been treated to be as smooth as possible, and the geometry has no sudden changes.

The rest of the wind tunnel maintains this square shape which will be called H. Considering that the equivalent hydraulic diameter of a square pipe is the length of its side, H will be used to non-dimensionalise lengths.

The purpose of the square pipe that follows the transition is to develop the flow to the next section. For this purpose, a length of 3.3 hydraulic diameters is considered sufficient.

A distortion panel capable of transforming a uniform flow profile into the appropriate pressure profile, which must resemble the profile measured at the real engine, can be clamped at the end of this straight pipe. The distortion panel is essentially a 3D-printed screen with varying porosity that causes a certain pressure drop based on that porosity. The hexagonal shape of the pores is structurally sound and results in a lower pressure drop throughout the panel.

A straight pipe is put between the distortion panel and the test section so that the first measurement plane, UMS1 (Upstream Measurement Section 1), is at a proper distance from the panel. Turbulence typically decreases after two hydraulic diameters and also the velocity profile stabilises, therefore the length of this straight segment is enough to ensure a stable flow field in the test section.

The requirement for the distortion panel arises from the fact that the flow inside the turbofan bypass duct is not uniform and has a certain velocity profile. A more detailed explanation and the specifics of the methodology design together with numerical and experimental results related to this distortion screen can be found in Chapter 4.

The test section is a 5.5 H-long square duct with borosilicate lateral and top walls that have been treated for laser wavelength transparency. A sketch showing the main parts and locations of the test section is displayed in Fig. 3.6. It also includes the system of reference used in the thesis.

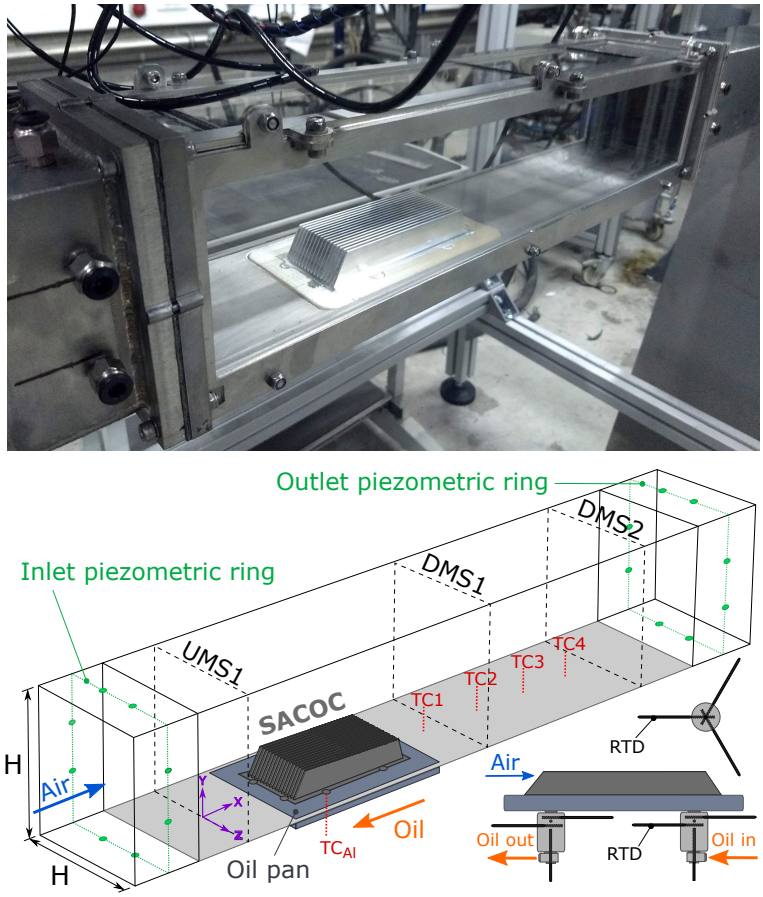

Figure 3.6: Above, picture of the test section. Below, sketch of the test section with different instrumentation locations, together with the system of reference located at the origin of coordinates.

The floor of the test section, where the SACOC is mounted, is made of steel as the rest of the wind tunnel. Piezometric rings are set before and after the test section to monitor the pressure drop caused by the heat exchanger.

Because the bottom wall is steel, and to ensure that the heat is exchanged solely through the SACOC, a 3D printed oil pan is attached to the floor, while the SACOC is mounted onto the oil pan, which is made of ULTEM 1010, a thermoplastic that is suited for long-term heat resistance.

To set up an arrangement as flush as possible, both the heat exchanger and oil pan are attached to the bottom of the tunnel from the outside. A more detailed explanation of the attachments and characteristics of the heat exchanger can be found in Section 5.1.

As with the rest of the wind tunnel, the test section is modular, having both lateral walls and ceiling affixed to a base frame. However, they can be removed and replaced by parts needed for specific measurements. For instance, to carry out infrared thermography measurements, aluminium walls with tailored gaps to screw an insert that features a window transparent to the long-wave infrared radiation can be used.

Furthermore, to perform intrusive measurements, the top wall can be substituted by a series of borosilicate crystals that can be arranged to create slots to introduce probes through.

Three measurement sections have been defined to characterise aerodynamically and thermally the SACOC performance: UMS1, DMS1 and DMS2, which stand for Upstream Measurement Section 1 and Downstream Measurement Section 1 & 2. The first section is placed 0.75 H upstream of the SACOC leading edge whereas DMS1 and DMS2 are located 0.5 H and 2 H downstream of its trailing edge.

Moreover, 4 taps can be mounted on the centre of the floor of the wind tunnel to insert thermocouples in the SACOC wake and determine the evolution of the temperature downstream of the device. These are called TC1, TC2, TC3 and TC4 and are placed every 0.4 H from the heat exchanger trailing edge.

Table 3.1: Axial location of each relevant section

Section	X/H **[-]**
Inlet piezometric ring	-0.65
Inlet test section	-0.36
UMS1	0
Fins leading edge	0.75
TC1	2.4
DMS1	2.5
TC2	2.8
TC3	3.2
TC4	3.6
DMS2	4
Outlet test section	5.11
Outlet piezometric ring	5.4

Figure 3.6 shows the locations of the different instruments used in the characterisation. Stabilising the origin of coordinates on the bottom wall at the centre of UMS1, with the x axis pointing towards the flow direction, y pointing above and z forming a right-handed reference frame (see Fig. 3.6), the relevant axial locations are summed up in Table 3.1.

3.1.3. Oil conditioning system

Although practically any type of lubricant can be used in this circuit, oil that responds to SAE 5W-30 rheological and thermal standards [154, 155] is used. In the first place, a pump takes oil from a storage tank to circulate it throughout the circuit. Before entering the pump, a water-cooled heat exchanger keeps the temperature below 110°C, with an average drop of 40°C.

The pump operates at a constant speed of 1450 rpm and with a power of 370 W, thus a bypass with a manually controlled valve is utilised to manage the mass flow in the circuit. The oil then flows through a heat exchanger dedicated to keep the flow meter temperature at the nominal operating value, which is normally less than 60°C.

Between the heat exchanger and the flow meter, a filter uses a succession of paper walls with micrometric porosity to filter out any contaminants that may have formed along the circuit. The fluid is afterwards sent through a high-precision Coriolis mass flow meter.

An electric heater is then used to raise the temperature of the oil. This component is made up of two in-series electrical resistors rated at 2.6 and 2.5 kW respectively.

After the electric heater, a thermocouple is installed to feed a PID control system, which manages the amount of power required in the resistors to attain the specified fluid temperature. The oil is then transferred to the SACOC oil pan. Two oil reservoirs are installed before and after the exchanger above the oil pan height, to ensure that the pan is filled with oil and that no air bubbles remain below the exchanger.

The lubricant returns to the oil storage tank after leaving the SACOC and the downstream reservoir. The pump draws oil from this tank and passes it through a filter to prevent debris from entering the circuit. In addition, a branch connects the tank to the main circuit after the pump, allowing the valve to open and return fluid to the tank if the pressure exceeds a specified threshold. Figure 3.7 displays a diagram of how this oil conditioner works.

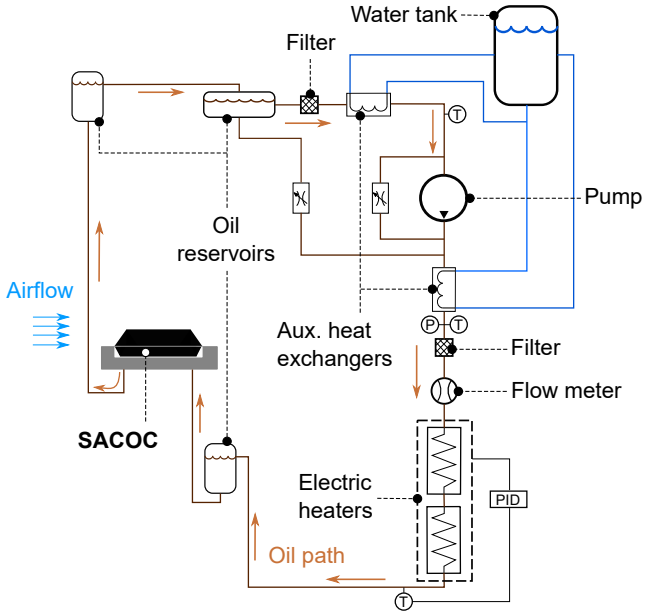

Figure 3.7: Schematic of the oil conditioning system.

3.2. Instrumentation

In order to perform an experimental characterisation, it is important to consider the type of data that is worth knowing and the best way to obtain it. Moreover, each technique has its own advantages and limitations compared to others.

To exploit to its maximum the experimental facility and perform an adequate characterisation of the heat exchangers' performance, the instrumentation used during the measurements, grouped as if they are considered to be intrusive or non-intrusive techniques, will be presented.

3.2.1. Intrusive techniques

Focusing firstly on the intrusive apparatus, although different probes can be used for the aerodynamic characterisation in the measurement sections (pitot, multi-hole...), 3.2-mm-diameter Kiel probes have been selected.

Shortly, a Kiel probe is a probe that acquires total pressure by surrounding the pressure port (that, in this case, has a diameter of Ø 0.82 mm) with a head that works as a shield (see Fig. 3.8).

The interior of this head presents a smooth convergent-divergent channel in which, assuming an isentropic evolution, the flow in the direction of the pressure port is magnified, maintaining the total pressure. For this reason, this type of probe provides better results of total pressure in turbulent flows and they are less susceptible than others to slight misalignments.

The total pressure is read by GE UNIK 5000 piezoresistive sensors that have been calibrated for the operation regime and have a 0.2% accuracy. It is possible to observe the calibration curves for each sensor in Fig. 3.9. The pressure was measured using a Fluke 729 Automatic Pressure Calibrator. The behaviour of each sensor is finely adjusted to reproduce the actual values, presenting almost perfect linear fits with a fraction of unexplained variance lower than 10^{-5}.

Figure 3.8: Detail of the Kiel head.

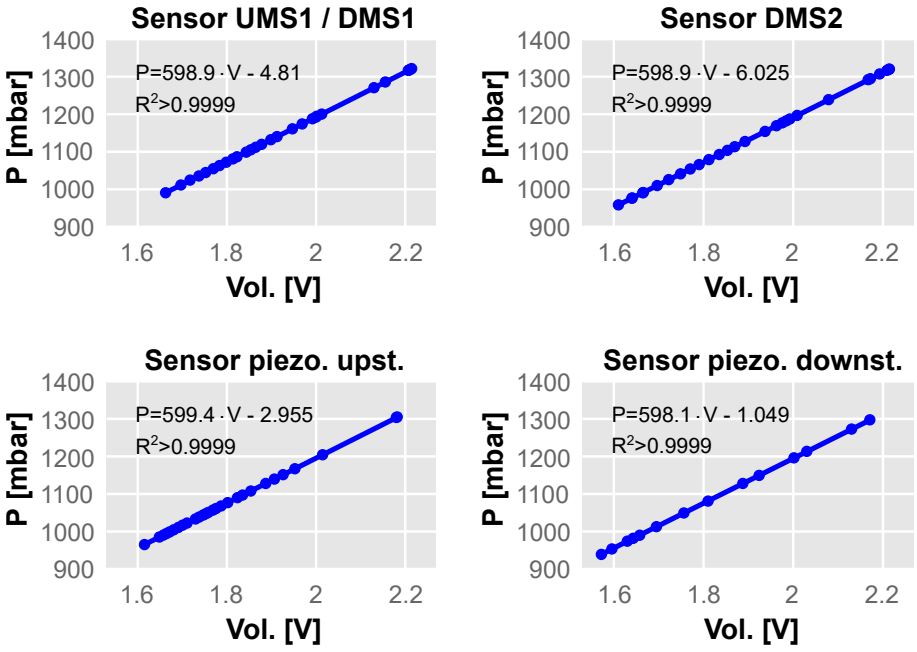

Figure 3.9: Calibration of the GE UNIK 5000 piezoresistive sensors.

In order to derive the velocity in each section, the static pressure is acquired from both piezometric rings upstream and downstream of the test section. Then, after a correction to account for the static pressure in each plane, and assuming it to be constant in the cross-section, the velocity is calculated by applying compressible isentropic flow equations.

Additionally, these Kiel probes also feature a class 1 T-type thermocouple beneath the head, which permits to perform a temperature analysis at the same time as the aerodynamic.

There is, however, a small drawback: since the probes are inserted through slots in the ceiling of the tunnel, when they are at their lowest position (with the head close to the floor of the tunnel), there will be a small gap between the bottom wall and the thermocouple due to the presence of the pressure port. An image of the head of a Kiel probe used can be seen in Fig. 3.8.

The probes are mounted in bi-axial traverse systems that enable to characterise each measurement plane completely. There are three 2D traverses in total – for UMS1, DMS1, and DMS2 – each consisting of two stepper motors synchronised via MATLAB through a microcontroller. In Fig. 3.10 the measurement setup with the Kiel probes mounted in the traverse system can be seen.

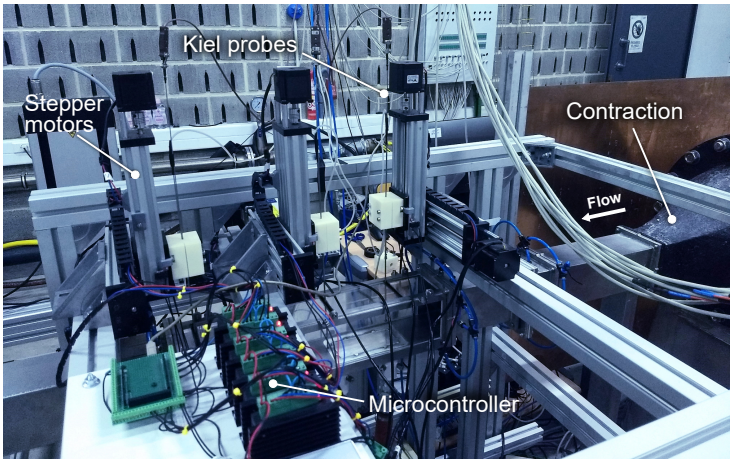

Figure 3.10: Image of the Kiel probes mounted in the stepper motors of the traverse system.

Regarding thermal measurements, besides the thermocouples already present in the Kiel probes, the thermal wake behind the SACOC can be characterised by means of 4 class 1 K-type grounded thermocouples with 3 mm diameter.

They are inserted through the bottom every 0.4 H from the trailing edge of the fins in the centre of the section. An offset of 1 mm in height among each has been set so the wakes from the upstream thermocouples do not affect those downstream. The reference temperature from the incoming air measured prior to the settling chamber is also measured with a K-type grounded thermocouple.

The oil temperature beneath the SACOC is measured with 4 RTDs Pt1000 at the inlet and another 4 at the outlet. Three of them are inserted radially whereas the fourth is placed co-axially with the inlet-outlet duct (see Fig. 3.6) and the temperature of each section is averaged with all the values.

Thermoresistances, unlike thermocouples, need to be immersed up to a certain depth into the fluid they are characterising in order to capture properly its temperature. The physical principle that lies behind this measurement is based on the variation in the value of a resistance with temperature. This resistance occupies a certain space in the tip of the sensor, so the full resistance has to be surrounded by the fluid to adequately capture the temperature. Thermocouples, on the other hand, correlate the voltage generated in a junction of two different materials with the temperature they are exposed, so the measurement can take place in almost a punctual volume.

For this reason, a preliminary test was conducted, prior to the SACOC characterisation, to determine the required depth the RTDs need to be to properly capture the temperature of the fluid. The test consisted of introducing an RTD in a hot bath, generated by a Termotronic-100 thermostat immersion heater.

The immersion heater can control the temperature of a determined volume of water by means of a resistance and a shaker that distributes the temperatures equally in the volume. A thermometer was also placed at the same distance as the RTD to check the temperature value. The resistance from the RTD was then measured with a multimeter to derive the temperature.

The first measurement was with the tip of the RTD at the water surface. The probe was inserted afterwards at different depths, waiting for the temperature to stabilise in the new zone and reading the value in the multimeter. Fig. 3.11 represents the experimental setup for these measurements and the evolution of the temperature read by the RTD. The temperature was set to 49°C and it is possible to observe how this value is steadily measured in depths of 18 mm and deeper.

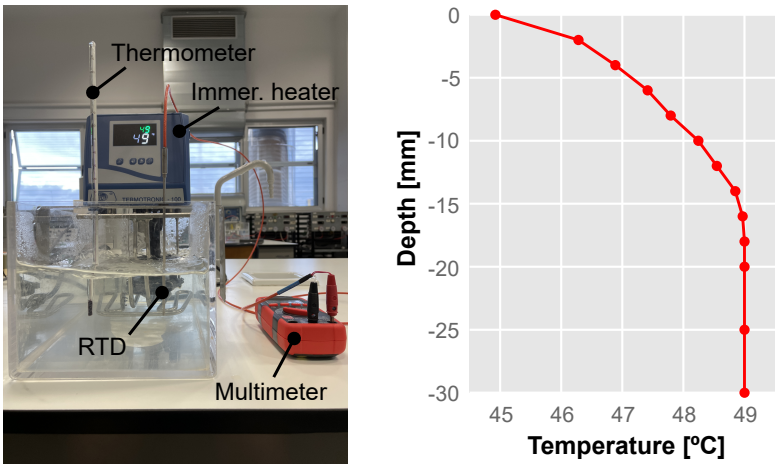

Figure 3.11: Evolution of the temperature measured by an RTD depending on its immersion depth. On the left, the experimental setup. On the right, the temperature evolution.

This implies that the RTDs which are radially inserted in the inlet and outlet of the oil pan to determine the temperature drop between these two locations need to be, at least, 18 mm inside the oil stream to capture its temperature.

Two different ways have been used to determine the mass flows. In the air, a FOX FT2 thermal mass flow meter of 6" with a range between 0 and 10870 Nm^3/h and accuracy within ±1% of the reading or ± 0.2% of the full scale has been employed, whereas a KROHNE Optimass 3300C S04 Coriolis flow meter with a range of up to 130 kg/h and accuracy of ±1% of the actual recorded flow rate has been utilised to control the oil mass flow.

In this aspect, it seems adequate to remark that neither flow meter can be considered strictly intrusive, since they both have no sort of interaction with the fluids in regions close to the test section (the Coriolis mass flow meter does not even disrupt the flow).

Similarly, the static pressure piezometric rings before and after the test section should not be considered intrusive, since the pressure ports are flush on the interior walls, but since they are used simultaneously with the Kiel probes to derive the velocity with the same pressure sensors, it is also convenient to comment them in this section. Besides, for differential pressure measurements, both piezometric rings are connected through a Sensirion SPD2000-L differential pressure sensor with a 3000 Pa range and an average reading accuracy of 1%.

Regarding the pressure drop, it is common to express the value as a non-dimensional coefficient that can be extrapolated to other conditions. In terms of heat exchangers, the Fanning friction coefficient f is typically used. It is defined as the local shear stress and the local flow kinetic energy density and is termed as follows:

$$f = \frac{\Delta p}{2L} \frac{D_h}{V^2 \rho} \tag{3.2.1}$$

being D_h the hydraulic diameter of the section, V the mean flow velocity, ρ its density and L a characteristic length. The pressure loss is evaluated through the term Δp.

3.2.2. Optical techniques

On the air side, many different techniques have been applied to characterise in a non-intrusive way different relevant aspects of the heat exchangers. Velocity has been determined with laser techniques such as High-Speed PIV or Laser Doppler Anemometry (LDA), flow visualisation has also been possible by taking advantage of the temperature gradients in the SACOC wake and using Schlieren visualisation (to which PIV analysis can be applied for a more quantitative value), fluid-structure interaction has been performed too with a Laser Doppler Vibrometer (LDV) and thermal characteristics were determined by means of infrared thermography.

A TSI six-jet atomiser model 9306 has been utilised for those experiments that required seeding. To tune the required amount of seeding, it uses six Laskin nozzles controlled by three valves, as well as a pressure regulator and a dilution system. To introduce the particles, a rod is inserted in the settling chamber between both honeycombs so the seeding is as uniform as possible and the presence of the rod is unnoticed in the test section.

3.2.2.1. Aerodynamics: PIV

Particle Image Velocimetry (PIV) is one of the most widely utilised laser techniques. To determine the velocity flow field of a region, this method uses the relative displacement between two frames. A rapid camera is synchronised with a laser sheet that lights a plane of the flow that has been seeded for a period of time. During this time, light is scattered by particles lit by the laser, and the fast camera records numerous pairs of frames.

As a result, the velocity can be simply calculated by correlating the displacement of the particles between frames and knowing the frequency at which they are taken. Fig. 3.12 represents a typical PIV measurement. In [156] a full description of PIV can be found.

A PIV system from Dantec Dynamics has been employed in this characterisation. An LD30-527 Litron laser, a Phantom VEO 640 high-speed camera, a BNC 575 pulse generator, and DynamicStudio software make up the system.

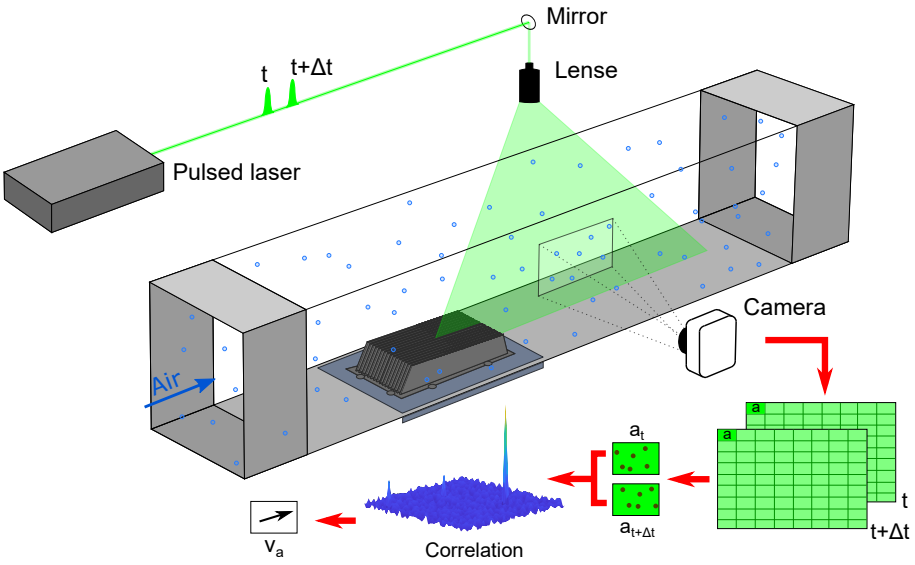

Figure 3.12: Schematic of a typical PIV measurement with the associated post-processing to derive the velocity field.

In the laser, two CW-pumped Q-switched Nd:YLF DPSS laser resonators produce infrared laser light at 1053 nm, which is subsequently transformed to visible light at 527 nm by an intra-cavity Harmonic Generation Assembly. Because the laser consists of two light sources, it is ideal for PIV because pairs of pulses can be much closer than half the acquisition frequency.

The laser beams are redirected through a series of mirrors into an optic device made up of three lenses that convert the entering beam into a laser sheet with an adjustable thickness that goes from 1 to 2 millimetres in the test area.

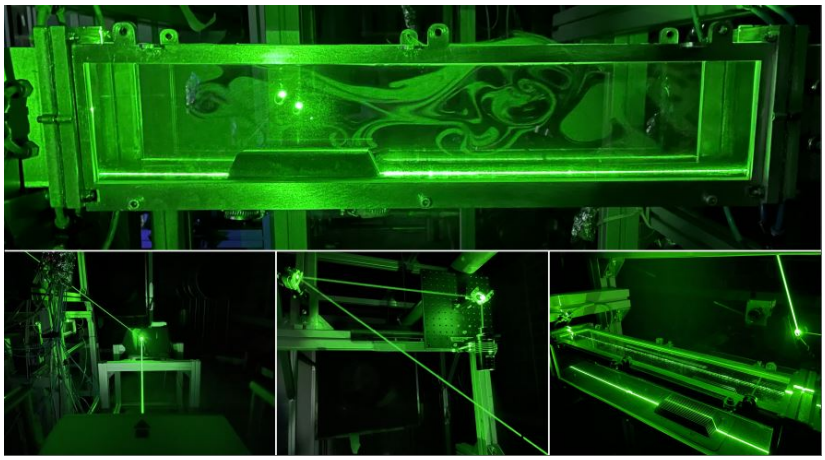

Figure 3.13: Images of the PIV setup during measurements.

A 60 mm Zeiss Planar T*1.4/50,mm ZF.2 lens with a green filter for 532±5 nm wavelengths is included in the Phantom camera. The camera's peak acquisition frequency with the maximum resolution (4 MPx) is 1400 frames per second.

This camera model has the ability to record in double frame, which is better for PIV measurements. Finally, the BNC 575 serves as a synchroniser for the laser and camera. It essentially triggers TTL signals across distinct channels with a software-defined delay.

Figure 3.13 collects some pictures of the PIV arrangement during measurements. The top image represents a view of the test section with seeding particles from the perspective of the camera. The bottom images display the path of the laser beam until it goes through the lens and reaches the test section as a laser sheet.

An important feature to consider when performing PIV measurements is the number of pairs of images needed to derive an accurate velocity field. Fig. 3.14 represents the average value of the longitudinal velocity component and its standard deviation. The values obtained for images over 500 pairs vary in less than 0.2%, which indicates that results with more than this amount of images can be considered accurate enough. The subindex PIV represents the value towards the variable converges measured with PIV, assumed to be the actual value of the variable for a number of images sufficiently large.

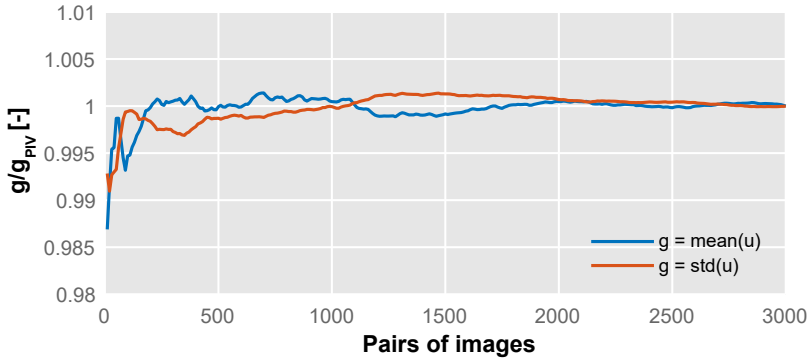

Figure 3.14: Values of the mean velocity and its standard deviation as a function of the pairs of images selected for their computation.

The system records images which can correlate and analyse the pixel's displacement of a determined particle. In order to convert these pixel displacements into actual velocity values, images have to be calibrated against a target.

Although there are many types of targets that allow automatic detection by the system, one of the most common and easy to implement is the Dotted pattern. It consists of a matrix of dots equispaced. Four features of these types of calibration targets need to be considered:

1. Dot spacing: it is the regular space between dots.

2. Zero marker: is the marker used to reference the centre of the target. It is always larger than the rest of the dots, and typically in the order of 50% the dot spacing.

3. Axis markers: the four nearest neighbours around the zero marker point out the direction of the calibration target axis. They are the smallest dots with typical diameters of 25% of the dot spacing.

4. Main markers: they are the dots that complete the extension of the target plate. Diameters in the order of 33% the dot spacing are typically used.

The PIV explanation presented in this section can also be used in the Stereoscopic PIV configuration. Essentially, the main difference is that two cameras are used (instead of one) and since the region evaluated by both cameras is the same, the differences in the outcomes of each camera can be used to reconstruct a three-dimensional velocity field.

There are some other differences between PIV and S-PIV. For instance, during S-PIV calibration, the target needs to be moved throughout the laser sheet thickness (which is slightly larger than in PIV to allow the fastest particles to be captured within the laser sheet), so the cameras can be calibrated in the three dimensions. Thus, typically around five images are taken during S-PIV calibration: one at the centre of the laser sheet, two upstream of the centre and two downstream.

Figure 3.15 shows an image of the S-PIV configuration during measurements at UMS1. It is possible to observe the laser path, the laser sheet (perpendicular to the flow direction) and both cameras, one on each side of the test section.

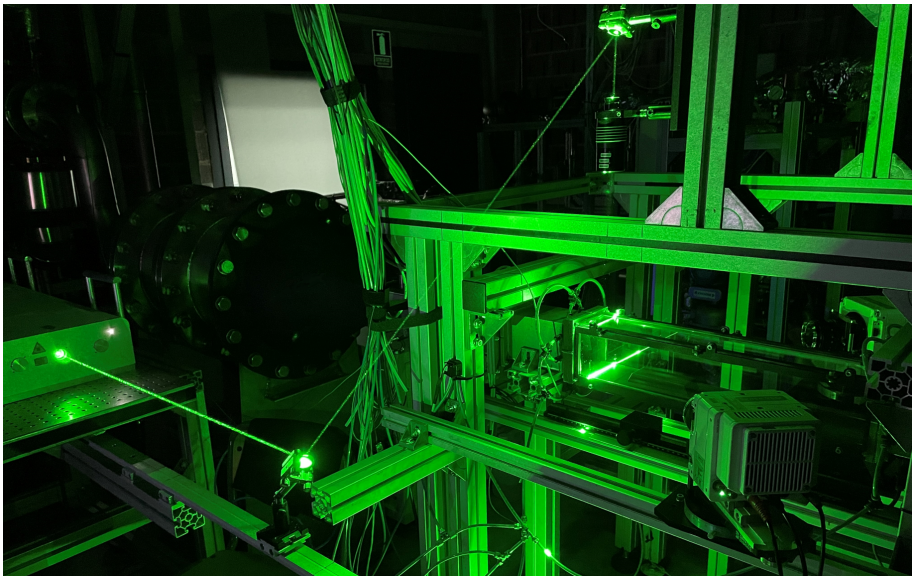

Figure 3.15: Stereoscopic PIV setup during measurements at UMS1.

As aforementioned, the laser sheet should be thicker in S-PIV than in PIV. This is especially necessary in cases such as the ones presented here: the laser sheet in PIV is placed in the flow direction (as shown in Fig. 3.12), but in the stereo configuration, the laser is rotated 90 degrees to illuminate a region perpendicular to the flow direction.

This implies that the residence time of the particles inside the laser sheet is considerably reduced, so the increase in thickness allows being able to capture particles for longer times. There are, nevertheless, two trade-offs to consider when doing this.

On one hand, it is important to note that the thicker the laser sheet is, the more distributed the energy of the light. It makes the image darker and is possible to lose information about particles that are not captured.

On the other hand, there is a trade-off in the time delay between frames. It is obvious that the faster the second frame is captured, the less the particles have moved, being more likely to remain in the laser sheet during the second photo and favouring that the thickness of the laser sheet does not have to be increased (getting rid of the previous problem of low intensity). However, if the fastest particles do not move a lot, the slowest ones may remain almost unchanged, not being able to capture any displacement. Very short times between pulses can lead to what is called frozen flow for some velocity components.

Therefore, it is important to determine the laser sheet thickness and the time delay between pulses so enough light illuminates the particles and all velocity components are captured, being fast or slow.

During stereoscopic measurements, the cameras cannot be placed perpendicular to the laser sheet as in standard PIV. Actually, this fact is what makes it possible to derive the third velocity component. Nevertheless, camera systems are prepared to focus on planes which are parallel to their lens and sensor.

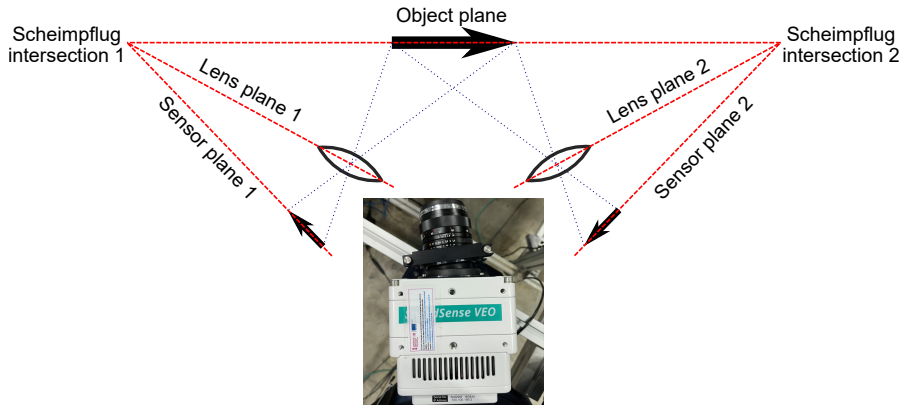

Figure 3.16: Scheimpflug angles in an S-PIV measurement setup, highlighting the object plane, the lens planes and the sensor planes. Each respective Scheimpflug intersection is marked. An image of the camera 1 (according to the sketch) with the lens tilted with respect to the sensor is also included.

In order to avoid this, a Scheimpflug correction is needed. Scheimpflug's principle is a description of the geometric relationship between the orientation of the plane of focus, the lens plane, and the object plane of an optical system (such as a camera) when the lens plane is not parallel to the plane from the object.

Figure 3.16 represents the typical configuration in S-PIV to correct the focus issue. It is possible to observe how the correction is performed by changing the orientation between the lens and the sensor. To accomplish this, the cameras and lenses are mounted in a device that allows the free tilting of the lens with the body of the camera fixed. By doing this, instead of rotating the sensor plane, the linear perspective remains unaltered.

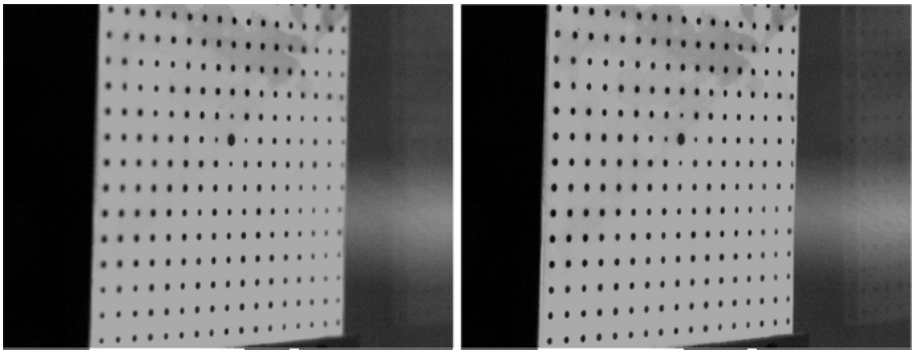

Figure 3.17: Example of how the Scheimpflug correction works. On the left, an image of the calibration target directly taken with a camera in S-PIV configuration. On the right, the same image after applying the Scheimplug correction.

An example of a practical application of a Scheimpflug correction is shown in Fig. 3.17. In both pictures, the calibration target is recorded. It is placed centred in the laser sheet, so it is a representation of how the camera would see the particles during acquisition.

The picture on the left was taken with a standard configuration, i.e., with the lens and sensor planes parallel to each other. Although the centre of the image is in focus, it is possible to observe that getting closer to the lateral dots the image losses sharpness as it gets out of focus. However, the picture on the right was taken with Scheimpflug correction, and the whole calibration target is seen in focus.

3.2.2.2. Aerodynamics: LDA

LDA (Laser Doppler Anemometry) is an optical technique that utilises the Doppler effect of a flickering particle. Another very common way of calling it is Laser Doppler Velocimetry (LDV), but in order to avoid confusion with another technique employed in the characterisation that also uses the acronym LDV (Laser Doppler Vibrometry), the name LDA is preferable in this case.

When a pair of laser beams collide at a point, the frequency of both lights interacts with each other. A precise fringed volume with high-brightness fringes will be formed in the small volume of their intersection if the frequency shift between them is set suitably. As a result, when a particle scattering laser light travels through that fringed space, it will flick at a frequency determined by the particle velocity and the distance between the light fringes. Boutier and Most [157] provide a comprehensive description of the principles underlying this method.

A picture of the LDA configuration during measurements at UMS1 is displayed in Fig. 3.18. It is possible to observe the measurement volume created by the four laser beams just upstream the SACOC in the test section.

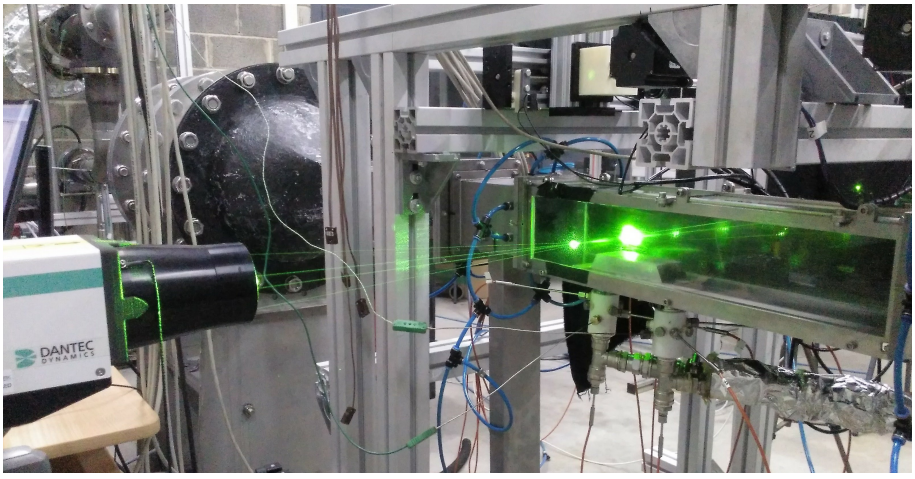

Figure 3.18: Image of the LDA setup during a measurement in the Upstream Measurement Section.

A Dantec FlowExplorer DPSS 500 2D system with a 64 mm diameter optic lens and a 500 mm focal length has been utilised for the characterisation, which was handled by the BSA Flow software. The accuracy of this LDA to determine the velocity is 0.11%. One of the unique features of this system is

its ability to quantify 2 velocity components by emitting two pairs of laser beams, each with a wavelength of 532 nm for the horizontal component and 561 nm for the vertical component. Each pair of beams' polarisation is perpendicular to the plane they create, and so perpendicular to the polarisation of the other pair as well. When creating each fringed pattern, this allows the two pairs to intersect in the same volume without interfering.

A Bragg cell operating at 80 MHz is used to divide an initial continuous beam into two, one with the original frequency and the other with the shifted one, in order to generate each pair of lasers and set a prescribed frequency shift between them. The ambiguity in velocity direction is eliminated by generating movable fringes in the volume, so particles with zero velocity can also be caught.

This is particularly important when, for example, a data quality validation process demands the system to capture a particle in both dimensions, but the particle has unidirectional velocity values.

Prior to the beginning of the measurements, it is important to make sure the laser beams are correctly aligned. To do so, a pinhole is placed at the focal point of the device, The focal point is found by introducing light through the signal-out port. Once the spot is located, the mirrors that guide each one of the laser beams are tilted, so each beam passes through the pinhole. The correct mirror configuration is achieved when the four beams exhibit a diffraction pattern after the pinhole.

Figure 3.19 depicts, on one hand, the alignment process to orientate the mirrors in the laser head and, on the other hand, the diffraction pattern that is sought after the pinhole for the four laser beams.

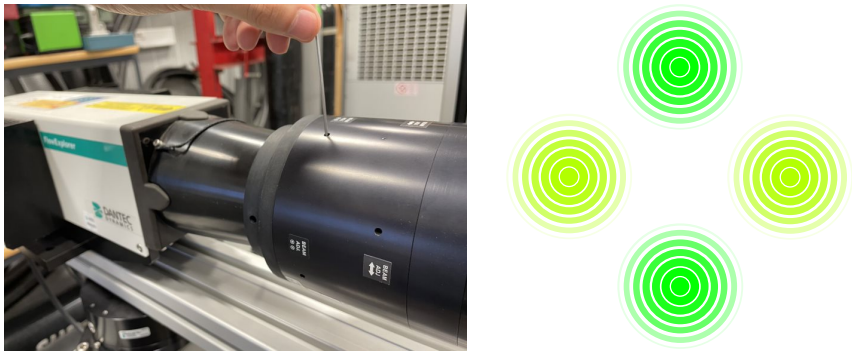

Figure 3.19: Process to align the LDA lasers. On the left, an image of the mirrors in the laser head being adjusted. On the right, the diffraction pattern sought for the four laser beams.

3.2.2.3. Flow visualisation: Schlieren

The Schlieren technique is based on changes in a fluid's refractive index as its density is changed by pressure or temperature changes. As a result, if a section of the fluid is appropriately lighted and recorded, those regions with a different refractive index will tilt the light beams that pass through, resulting in darker areas in the image recorded due to the lack of light. As a result, unlike earlier methodologies, it does not require the fluid to be seeded in order to visualise the flow.

Part of the light can be blocked to increase the contrast between the lighter and darker zones by placing a thin object in the focal point of a concave mirror that receives the experiment's light. The physics behind the Schlieren are explained in detail by Settles [158].

If a heat exchange occurs between oil and air through the fins, in this case, the air in contact with the heat exchanger will be hotter than the freestream, resulting in a temperature gradient that Schlieren technique can visualise.

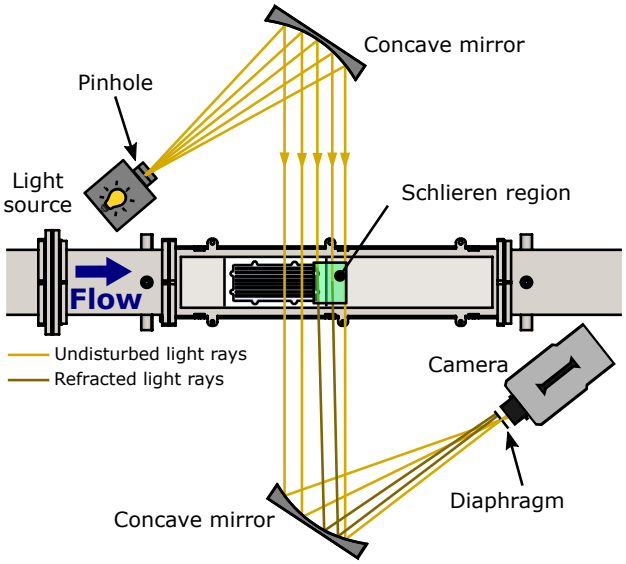

Figure 3.20: Schematic of a typical Z arrangement to perform Schlieren measurements.

A Z setup has been set up to conduct the research. In Fig. 3.20, a schematic that depicts the setup can be observed. This is the most frequent design because it offers benefits such as the ability to examine vast test sections and the absence of coma aberrations.

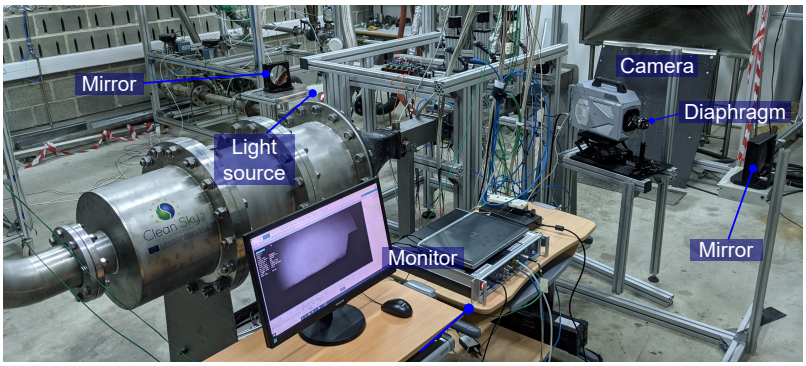

Figure 3.21: Set up for Schlieren visualisation. It is possible to observe the trailing edge of the SACOC in the monitor.

The light source with a diaphragm to simulate a punctual source has been placed at the focal distance of a concave mirror, which reflected the light with parallel light beams illuminating the region downstream of the heat exchanger. Another concave mirror collected the light and focused it on a point where another diaphragm was located, while a camera recorded all of the passing light. Figure 3.21 represents the experimental configuration in the wind tunnel. The elements involved in the Schlieren visualisation are highlighted in the image.

Although it is possible to visualise the airflow downstream of the heat exchanger, it is important to note the operating conditions of the device. Fig. 3.22 represents two frames of the SACOC working under two different conditions: the top figure corresponds to an air mass flow much lower than the nominal (in the order of ∼3%), whereas the bottom figure shows the results for nominal mass flows.

It is possible to observe that the airflow behind the heat exchanger is easily identifiable for low mass flows, because of temperature, and hence, density gradients are larger as the flow is heated for a longer period of time.

Nevertheless, the flowfield downstream of the SACOC for nominal conditions is not that evident in nominal conditions because these gradients are not that large. Anyhow, in the video, it is possible to see the airflow behind the fins. When presenting the results, no images are included because single frames are not very representative. However, as the flow can be seen, quantitative results from PIV analysis of this region are included.

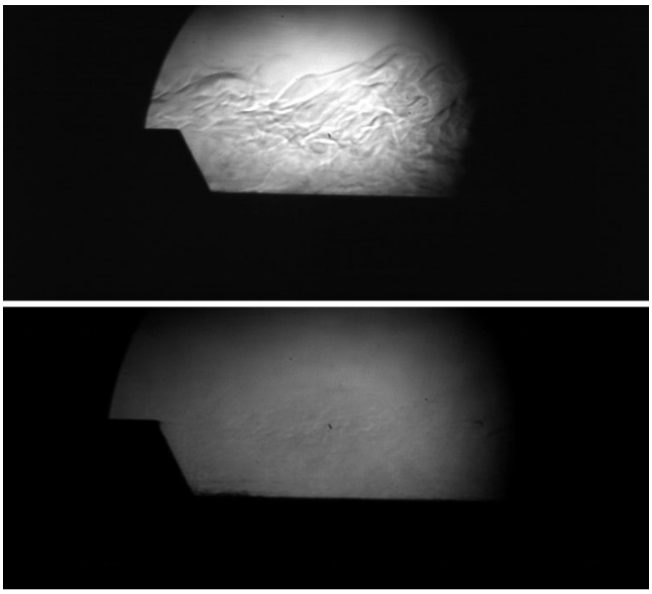

Figure 3.22: Schematic frames for two different operating conditions. At the top, with very low mass flow (∼3% of the nominal conditions). At the bottom, with nominal conditions. Air flows from left to right.

3.2.2.4. Fluid-structure interaction: LDV

Apart from the aerodynamic measurements that only consider the flow behaviour, its interaction with the fins of the heat exchanger is also an interesting aspect to study. With this purpose, Laser Doppler Vibrometry (LDV) allows the measurement of the vibrations in the lateral fin induced by the air. Chiariotti et al. [159] explain the theory behind the principle in addition to potentials, issues, and best practice approaches. For this technique, a Polytec PSV-500 system has been used. It uses laser that is fired and divided into two beams, where one of them undergoes a frequency shift process through a 40 MHz Bragg cell. This will eliminate the ambiguity of the measurement. One of them is directed towards the object to be measured and oriented with a series of mirrors, whereas the other one is led to a detector.

The beam that hits the object will rebound and suffer a frequency change that depends on the velocity of the object (a velocity associated with the vibration). The light is then collected and sent to the detector together with the original beam.

The interaction between both beams creates a typical light / dark interferometry pattern that depends on the frequency shift between them. Since the pattern created would be independent of the velocity direction if both lasers had the same frequency originally, the change in frequency induced by the Bragg cell generates a default pattern which does consider the direction of the velocity.

The vibrometer can achieve a resolution of 2 nm using appropriate interpolation techniques, and this may be increased as far as the pm range using digital demodulation techniques.

A preliminary evaluation of the experimental setup was carried out before the measurements were made. In order to do this, the group velocity propagation of Lamb waves in a one-millimetre thick aluminium plate (600 x 250 mm^2) was determined.

Lamb waves are those elastic waves that propagate in a plate with traction-free boundaries. There are two different types: symmetric or extensional (S) and antisymmetric or flexural (A). The symmetric waves propagate in the plane of the plate, whereas the antisymmetric ones propagate in the direction perpendicular to the plate.

The Polytec PSV-500 system can only detect vibrations perpendicular to its head, so only the flexural waves are going to be analysed. They move slower than the extensional waves, which allows the emitted vibration to be isolated from the boundary reflections.

A piezoelectric transducer (PZT) was used to excite the plate with a sinusoidal signal with a 2 Vpp amplitude, 24-bit resolution, and 48 Hz sampling frequency produced by a laptop's audio card and amplified by a 200 W Samson signal amplifier.

The plate's surface was discretised into 3589 points one roughly every 5 mm and some of them were chosen to determine the group velocity propagation attending to their alignment with the PZT's location. With this, besides determining the group velocity, it is possible to observe the advancement of the wavefront in the plate, as well as the reflections from the boundaries. The discretisation of the plate surface is shown in Fig. 3.23, with the PZT's placement and the spots from where the propagation of velocity was determined highlighted.

Several 15-kHz bursts were sent through the PZT to measure the group velocity. Each one of them had a length of 0.5 ms and the time left between two consecutive signals was long enough to guarantee that the plate vibra-

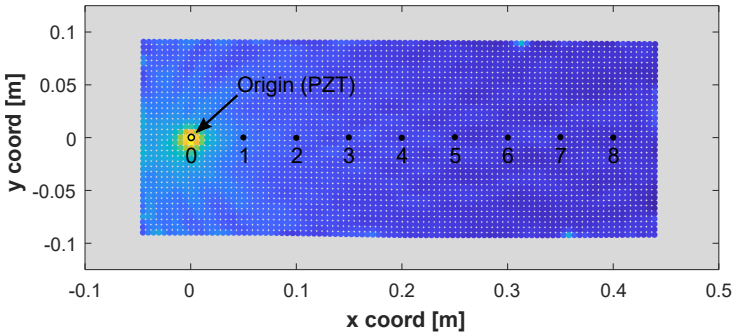

Figure 3.23: Discretisation of the aluminium flat plate used to determine the Lamb waves velocity. The location of the PZT actuator and the points used to determine the velocity are highlighted.

tion was totally over. The signal was also sent to the LDV system to keep the phase reference. With this configuration, it served as both a reference signal and a trigger for the system to start a 10 ms measurement.

To specifically capture the group velocity, slightly modified acquisition parameters were used. The LDV was triggered with the analogue output from the audio card, recording a pre-trigger sample of 2 ms (20% of the sample duration), in order to characterise each point of the discretised surface. A bandpass filter between 12.5 and 17.5 kHz was used to isolate the burst from other potential vibrational sources. With a sampling frequency of 250 kHz during the acquisition, a 4 μs temporal resolution can be achieved.

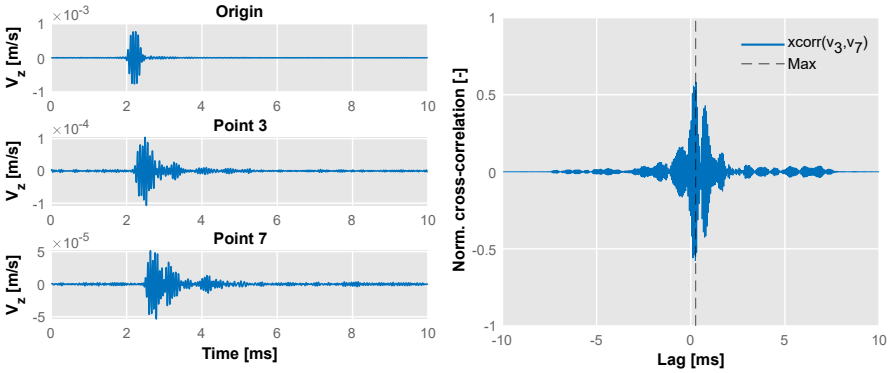

Figure 3.24: On the left, the signals in time of three different measurement points: Origin (point 0), Point 3 and Point 7. On the right, the normalised cross-correlation between the signals from Point 3 and Point 7. The lag at which the maximum cross-correlation occurs is marked.

Nine sample points were utilised to calculate the group velocity: the origin (point 0), where the PZT was positioned, and an additional eight sites located in line with the transducer (points 1 to 8).

The 10 ms signals from each point were examined and contrasted with each other. As a result, point 0 was compared with points 1, 2 and so on up to point 8. After that, point 1 was compared with points 2 to 8, point 2 with points 3 to 8... In the end, a total of 36 different samples were compared.

The two signals' cross-correlation was computed, and their peak-to-peak lag was calculated to do the comparison. In Fig. 3.24, the time signals from points 0 (Origin), 3, and 7 are displayed in the left graphics. The burst signal at the source can be seen, as well as how the vibration intensity decreases

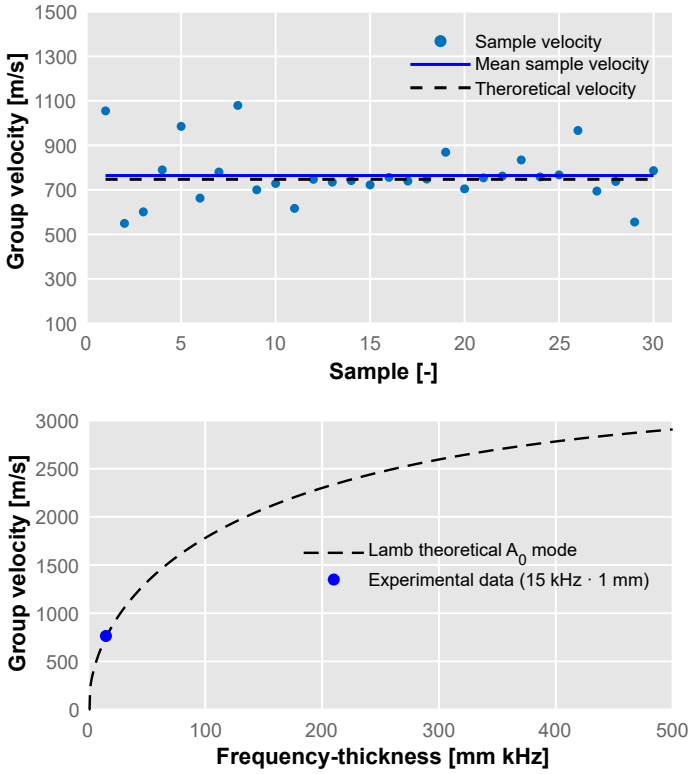

Figure 3.25: Measured and theoretical group velocity of Lamb waves in an aluminium plate 1 mm thick. At the top, the comparison between the mean velocity obtained from the 30 sample comparisons and the theoretical velocity. At the bottom, the measured velocity highlighted in the theoretical curve for different excitation frequencies and thicknesses.

away from the PZT. The right-hand side of the picture shows the normalised cross-correlation between the signals at points 3 and 7, marking the lag of the greatest correlation value.

The separation between sample locations was known, so the computed lag permits to determine the group velocity of the Lamb waves. After eliminating the outliers, 30 samples for comparison were chosen (Fig. 3.25). These samples' mean group velocity was 764.24 m/s, with a standard deviation of approximately 8.25%. The theoretical value for Lamb waves propagation in the A_0 mode under these conditions (one-millimetre aluminium plate with a 15 kHz vibration source) is 747.5 m/s, which only differs by 2.23% from the experimental data.

The bottom of Fig. 3.25 illustrates the actual experimentally measured data in the theoretical A_0 lamb wave velocity curve, whereas the upper part of the figure displays the individual velocity samples along with the mean and theoretical values.

3.2.2.5. Thermal measurements: IR thermography

Infrared (IR) thermography is based on the principle that any body with a certain temperature above absolute zero emits radiation. Although radiation depends on temperature, typical ranges of temperature values associated with this study (and almost any case below extremely high temperatures) radiate light in the range between 9 and 14 μm, which is in the long-infrared range of the electromagnetic spectrum.

Nevertheless, each surface has different efficiencies to emit thermal energy. This efficiency is referred to as emissivity and ranges from 0 (perfect mirror) to 1 (black body). In other words, it expresses the actual amount of energy an object is able to emit compared to the theoretical energy a black body with that temperature could emit. The emissivity value depends on several factors such as material, colour, texture and even temperature, so it has to be adjusted for each case.

In order to bypass this inconvenience, the emissivity of the SACOC and its surroundings has been tailored with a specific black graphite-based paint with high conductivity which does not alter the temperature on the surface.

Borosilicate walls present the problem of not being transparent to these wavelengths between 9 and 14 μm so, in order to perform thermography measurements, these walls can be substituted by others that incorporate an IR window. To cover the whole region of interest, the window can be affixed in different positions so the full image of the heat exchanger can be recomposed.

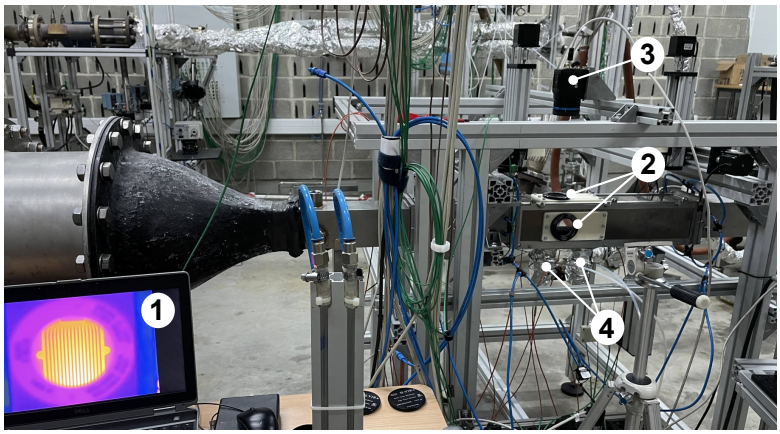

Figure 3.26: Infrared measurement setup. (1) Data acquisition, (2) IR windows, (3) thermographic camera, (4) oil system connections.

The surface temperature distribution has been determined using a FLIR A400 thermographic camera with an accuracy of ±2 K. Surface K-type thermocouples have been inserted through the bottom screw holes to measure the aluminium temperature at various locations, adjust the emissivity values of the specimen and validate the data obtained with the IR camera. The setup employed during the characterisation is displayed in Fig. 3.26.

These results from the IR camera can be used to calculate the base temperature of the heat exchanger and derive a typical dimensionless number called Colburn j factor that relates the Nusselt, Reynolds and Prandtl numbers in the following way:

$$j = \frac{Nu}{Re\ Pr^{1/3}} \tag{3.2.2}$$

3.3. Data acquisition and reduction

During the measurements, data were acquired and reduced following different procedures depending on the technique used. Besides, since the oil temperature was found not to have any impact on the aerodynamic results, during most of the aerodynamic characterisation methods, the oil circuit was disconnected.

In cases where thermal interactions take place, the facility is set up by running the oil through the circuit and gradually increasing the temperature and adjusting the mass flow until the desired values are achieved. The

compressor is then turned on, and the air begins to flow through the tunnel, regulated by venting and throttle valves. Air and oil conditions are modified iteratively until stationary conditions are attained, which usually takes around 20 minutes.

The control of most of the acquisition equipment is centralised using a MATLAB routine, but alternative arrangements are employed depending on the measurement:

- Regarding the oil temperature measurements, the temperatures read by the 8 RTDs beneath the SACOC are acquired at 1 Hz through an Agilent 34972A data logger and averaged afterwards, assuming that the inlet temperature is the mean measured by the four RTDs in that location and following the same reasoning for the outlet temperature.

- During intrusive characterisation with Kiel probes, in order to prevent the influence of those inserted upstream, each section is measured separately. Sections are divided into 400 points in a 20×20 grid, with the measurement starting at the top leftmost point (looking in the flow direction). The Kiel probe goes towards the tunnel's bottom and then to the next column, restarting the measurement at the top. The voltage from the pressure sensors (Kiel and both piezometric rings), air and oil mass flow meters, and temperatures from the reference thermocouple and the Kiel thermocouple are read by an NI PXI DAQ system. A total of 100 samples are captured at a frequency rate of 50 Hz for each position.

- To perform the thermal wake measurements, because the bottom thermocouples downstream of the SACOC are all inserted at the same time, particular care is taken to avoid the sensing tip of each thermocouple being impacted by the wake of preceding ones, hence the thermocouples are placed with 1 mm increments in height. In these experiments, 27 points in the central ($Z = 0$) plane are acquired, and three readings are taken for each point over the course of 45 seconds at the same data rate of 50 Hz.

- The pressure drop experiments are conducted by adjusting the air mass flow until stationary conditions are achieved. The air mass flow, reference temperature, and differential pressure between the intake and outlet piezometric rings are then measured at a data rate of 25 Hz for one minute.

- During the thermographic measurements, the camera is set in position focusing on a specific region of the SACOC and when stationary conditions are reached, air mass flow, the reference temperature and the aluminium temperature are acquired simultaneously at 50 Hz for one minute, ensuring that the position of the aluminium thermocouple (in contact with the SACOC) is within the field of view of the camera snapshot to facilitate calibration. Note that the camera needs to be located at different positions to obtain a complete picture of the SACOC, and the results from each camera position is the average of a total of eight readings.

- Regarding the PIV characterisation, the camera is placed one meter away from the light sheet (which is around 1 mm thick) and focuses a region of 1792×1000 pixels. The acquisition mode is set to double frame at a frequency of 1 kHz with a time delay between pulses of 10 μs and an exposure time for each frame of 0.5 ms. Results are averaged over 2000-3000 pairs of images, performing an adaptive process that analyses interrogation windows which range from 64×64 to 32×32 pixels, with 16×16 steps. A peak validation ratio of 1.15 and universal outlier detection in a neighbourhood of 5 × 5 vectors are used with a detection threshold of 2 and a normalisation level of 0.1 Px.

- In the Stereoscopic PIV, the laser sheet is rotated to illuminate each of the perpendicular measurement planes, and its thickness is extended to roughly 4 mm. The second camera, necessary for the stereoscopic reconstruction, is placed on the other side of the test section. To catch the quick out-of-plane particles, the time delay between pulses is decreased to 8 μs. The results have been averaged after executing the same processing as in the bi-dimensional PIV and including the stereoscopic reconstruction on 1000 pairs of images (ensuring sample independence) at 1 kHz.

- The laser beams from the LDA system are focused with a 500 mm focal length lens and the control volume, with a size of $0.2 \times 0.2 \times 3.2$ mm, is moved via a 3D traverse system. The data collection mode is based on burst validations in both laser components at the same time. The velocity values are derived from the acquisition of several hundreds of bursts, and each burst is considered after detecting more than 30 particles. The laser current and the photomultiplier sensitivity and gain

are adjusted to improve the measurements, with a signal-to-noise ratio of 3 dB and a peak ratio validation of 3 to 1 between the first and second detection.

- In the Schlieren acquisition, a Photron FASTCAM SA-Z camera with a frame rate of 100 000 fps and a spatial resolution of 640 by 280 pixels has been employed. The mirrors used are elliptical, with a focal length of 620 mm. A pseudo-PIV analysis can be used to perform a more quantitative investigation of the velocity field, in addition to the flow visualisation, by using PIVlab [160]. It is important to note, nevertheless, that the pixel displacement will rely on the location of the particle throughout the width of the section, increasing the level of uncertainty produced from the calibration.

- The Laser Doppler Vibrometer head was 1.5 meters away from the fin, and a grid discretisation with a spatial resolution of 2.5 millimetres was performed. The LDV incorporates interpolation and demodulation algorithms that allow for displacements on the order of picometers. The bandwidth ranged from 0 to 12.5 kHz, with a frequency resolution of less than 1 Hz. The sampling rate was set to 31.25 kHz, with the final output averaging 5 times the measured displacement.

Magnitudes are presented in the results chapters as non-dimensional parameters for two reasons: on one hand, referring the results to nominal values makes comparisons to be more clear and, on the other hand, confidential data have been used during some stages of the study.

In general, data from the air at nominal conditions are used for non-dimensionalisation. Table 3.2 collects the values used in the process and the variables they apply to.

Table 3.2: Reference parameters used for non-dimensionalising magnitudes.

Magnitude	**Value**	**Definition**
Length	H	Test section height
Velocity	U_∞	Max. target velocity
Mass flow	$\dot{m}_\infty$	Nominal air mass flow
Density	ρ_∞	Nominal air density
Temperature	T_∞	Nominal air temperature

3.4. Post-processing metrics definition

In order to carry out a complete analysis and be able to make proper comparisons, it is necessary to derive some key parameters that indicate how well a heat exchanger performs. This section aims to define a series of metrics that will be used during the post-processing from a theoretical point of view, but also explaining how they will be implemented.

3.4.1. Aerodynamic metrics

The most critical metrics in terms of aerodynamic performance used during this thesis are the Fanning friction coefficient f and the Turbulent Kinetic Intensity.

3.4.1.1. Fanning friction coefficient

This term is a widely used non-dimensional figure to represent the aerodynamic impact of a heat exchanger in terms of pressure loss. It is defined as the local shear stress and the local flow kinetic energy density of the fluid around the heat exchanger.

From a pragmatic point of view, the equation that defines the Fanning friction coefficient is as follows:

$$f = \frac{\Delta p}{2L} \frac{D_h}{V^2 \rho} \tag{3.4.1}$$

Hence, in a test section with a hydraulic diameter D_h, being the heat exchanger L-long and operating in a fluid with a speed and density V and ρ, the coefficient f can be straightforwardly derived after measuring the pressure drop induced Δp. It is measured between both piezometric rings.

3.4.1.2. Turbulent Kinetic Intensity

Turbulence is a key factor in the design of fluid systems for heat or mass transfer, dispersion, mixing, and related processes. Basically, it can be understood as eddies that are created in the flow which take energy from the stream.

The quantitative way to express the amount of turbulence in a given flow is called turbulent kinetic energy. It is calculated as the kinetic energy associated with the velocity variations in a flow, assuming that the velocity field is composed of a mean value and these fluctuations. Hence, for a given velocity field, the associated turbulent energy (per unit of mass) is:

$$TKE = \frac{1}{2}\left(u'^2 + v'^2 + w'^2\right) \tag{3.4.2}$$

A more relevant parameter though that is closely related to turbulent kinetic energy is turbulent kinetic intensity. It puts into perspective the turbulent energy comparing it to the mean kinetic energy. Its definition is the ratio between the root-mean-square of the turbulent velocity fluctuations and the mean velocity. Thus,

$$TKI = \frac{\sqrt{1/3\left(u'^2 + v'^2 + w'^2\right)}}{\sqrt{u^2 + v^2 + w^2}} \tag{3.4.3}$$

And considering the definitions of TKE, equation 3.4.3 can be expressed as:

$$TKI = \frac{1}{V}\sqrt{\frac{2}{3}TKE} \tag{3.4.4}$$

3.4.2. Thermal metrics

Different figures can be used to determine the thermal performance of a surface heat exchanger. In this work, the most relevant are: heat transfer, overall heat transfer coefficient U and Colburn j factor. Other metrics such as heat transfer coefficient h or Nusselt number Nu are also typically used. They have been included in the definition of the Colburn factor since they are needed to derive it.

3.4.2.1. Heat transfer

The most straightforward parameter to characterise the thermal performance of a heat exchanger is heat transfer. Basically, it extracts heat from the oil section and delivers it to the air stream. Considering that the oil pan is made of ULTEM, which is a thermally insulating material, it can be assumed that the heat is only dissipated through the aluminium model.

The heat transfer between both fluids can be computed by determining the difference in enthalpy on the oil side. Thus,

$$\dot{Q} = \dot{m}_o \Delta i_o = \dot{m}_o C_{p,o} \Delta T_o = \frac{\dot{m}_o C_{p,o}}{4}\left(\sum_{i=1}^{4} T_{\text{in}_i} - \sum_{i=1}^{4} T_{\text{out}_i}\right) \tag{3.4.5}$$

where $\dot{Q}$ refers to the heat and i_o is the oil enthalpy. The oil mass flow $\dot{m}_o$ is measured with the flow meter installed in the oil conditioning system. The oil specific heat $C_{p,o}$ is derived from the rheological properties of the SAE 5W-30 at its working temperature and is assumed to be constant. Finally, the oil temperature difference is carefully determined by a complete measurement of inlet and outlet temperatures with 8 RTDs (four in each region), located as depicted in Fig. 3.6.

3.4.2.2. Overall heat transfer coefficient

A term that is typically used in heat exchangers is the overall heat transfer coefficient U, which is defined as the total thermal resistance between two fluids during a heat exchange process. It can be understood as a parameter that evidences how permeable a heat exchanger is in terms of energy transfer from the hot fluid to the cold one. Hence, the expression that defines the overall heat transfer coefficient is

$$\dot{Q} = UA\Delta T_{lm} \tag{3.4.6}$$

where ΔT_{lm} is an appropriate mean temperature difference, known as the log mean temperature difference.

The term ΔT_{lm} can be calculated using the energy balance in differential elements across the heat transfer area, being dx and dA the length and surface of a differential element. A schematic of the heat transfer process and typical temperature distributions in a counterflow heat exchanger can be seen in Fig. 3.27. Subscripts 1 and 2 refer to opposite terminations of the exchanger, corresponding 1 in this case to the air inlet and oil outlet, and subscript 2 to the air outlet and oil inlet.

In the energy balance analysis, the following assumptions are made:

- The only exchange is produced between oil and air, considering the heat exchanger is insulated from its surroundings.
- Kinetic and potential energy variations are negligible.
- Axial conduction along the heat transfer area is negligible.
- The overall heat transfer coefficient and the fluid specific heats are constant.

Applying the energy balance to a differential element like the one in Fig. 3.27, it is derived that

$$d\dot{Q} = \dot{m}_o C_{p,o} dT_o = C_o dT_o \tag{3.4.7}$$

and

$$d\dot{Q} = \dot{m}_a C_{p,a} dT_a = C_a dT_a \tag{3.4.8}$$

being C_o and C_a the oil and air heat capacity rates, respectively. The heat transfer across a differential surface can be also termed as

$$d\dot{Q} = U \Delta T dA \tag{3.4.9}$$

where $\Delta T = T_o - T_a$ (see Fig. 3.27). Combining Eqs. 3.4.7 and 3.4.8 into the differential form of ΔT,

$$d(\Delta T) = dT_o - dT_a = d\dot{Q}\left(\frac{1}{C_o} - \frac{1}{C_a}\right) \tag{3.4.10}$$

Introducing Eq. 3.4.9 in the term $\dot{Q}$, rearranging and integrating across the heat exchanger, it is possible to see that

$$\int_1^2 \frac{d(\Delta T)}{\Delta T} = U\left(\frac{1}{C_o} - \frac{1}{C_a}\right)\int_1^2 dA \tag{3.4.11}$$

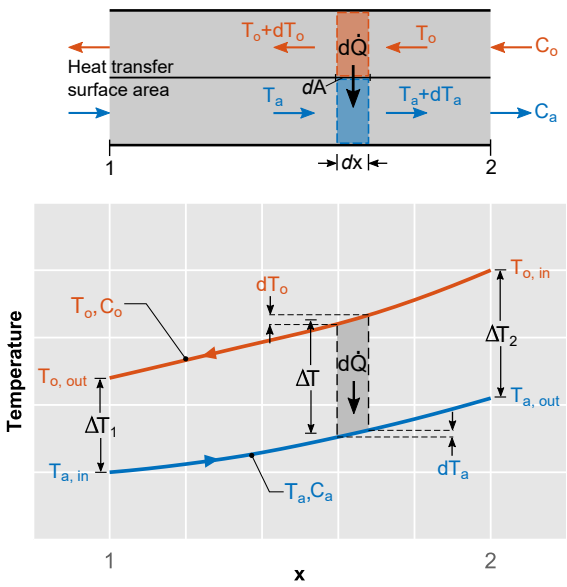

Figure 3.27: Schematic of the heat transfer process and typical air and oil temperature distributions in a counterflow heat exchanger.

which leads to

$$\begin{aligned}\ln\left(\frac{\Delta T_2}{\Delta T_1}\right) &= UA\left(\frac{1}{C_o}-\frac{1}{C_a}\right)\\ &= UA\left(\frac{T_{o,in}-T_{o,out}}{\dot{Q}}-\frac{T_{a,out}-T_{a,in}}{\dot{Q}}\right)\\ &= \frac{UA}{\dot{Q}}\left[\left(T_{o,in}-T_{a,out}\right)-\left(T_{o,out}-T_{a,in}\right)\right]\end{aligned} \tag{3.4.12}$$

Considering the flow locations in Fig. 3.27, it is possible to see that $\Delta T_1 = T_{o,out} - T_{a,in}$ and $\Delta T_2 = T_{o,in} - T_{a,out}$. Hence, the heat transfer equation can be expressed as

$$\dot{Q} = UA\frac{\Delta T_2 - \Delta T_1}{\ln(\Delta T_2/\Delta T_1)} = UA\Delta T_{lm} \tag{3.4.13}$$

Now that the log mean temperature difference is defined, it is important to derive its value from the experimental measurements. As previously explained, temperatures are well characterised in the oil inlet and outlet and these, together with the mass flow, are used to derive the heat.

Assuming stationary conditions and a complete heat transfer to the air, it follows that

$$\dot{Q} = \dot{m}_o C_{p,o}\Delta T_o = \dot{m}_a C_{p,a}\Delta T_a \tag{3.4.14}$$

The only unknown in Eq. 3.4.14 is ΔT_a and, since the incoming air temperature is also measured and assumed uniform across the section, the air temperature downstream of the SACOC can be calculated. With this last value, ΔT_{lm} is already experimentally defined.

Note that the product UA is not specified to belong either to the air or the oil side. This is because there is not a single value for U, but it depends on the reference area used and, in general, it can be said that $U_o \neq U_a$ as long as $A_o \neq A_a$. A common approach when comparing the performance of different heat exchangers is to use a reference area to derive the U coefficient.

3.4.2.3. Colburn factor

One of the most common non-dimensional factors used to determine the heat exchange capacity of a heat exchanger is the Colburn j factor. The definition of this factor relates the heat transfer and the momentum of a fluid and is termed as

$$j = \frac{Nu}{Re\ Pr^{1/3}} \tag{3.4.15}$$

where Nu, Re and Pr are the non-dimensional parameters Nusselt ($Nu = hL/k$), Reynolds ($Re = VL\rho/\mu$) and Prandtl ($Pr = C_p\mu/k$). The parameter L is the length of the fin on the base, defined as the characteristic length in the calculations. The rest of the parameters, ρ, C_p, μ, and k, are air density, specific heat, viscosity, and conductivity, respectively. The velocity V is proportional to the mass flow for a fixed geometry and constant temperature. Finally, the h represents the convective heat transfer coefficient.

The nature of the convective heat transfer coefficient h is well understood, in terms of being the coefficient that adjusts the heat transfer between a fluid, with moving particles, and a solid which have different temperatures. Thus, for a reference area A, the convection heat transfer can be expressed as

$$\dot{Q} = hA(T_s - T_\infty) \tag{3.4.16}$$

being T_s and T_∞ the solid and fluid bulk temperatures.

Beyond the clear definition of the convective heat transfer coefficient, the experimental characterisation of this figure is far from obvious. The first step for its determination is to calculate the heat transfer, using equation 3.4.5, measuring the oil mass flow and the temperature difference between the inlet and outlet.

Equation 3.4.16 defines the convection heat exchange between a solid with a temperature T_s and a fluid with a temperature T_∞. In the case of a finned heat exchanger, the reference temperature used in the solid is its base temperature T_b. However, it is obvious that when fins are added, the temperature along them is not as high as in the base. For this reason, a parameter that accounts for the overall surface efficiency η_0 has to be included in the equation 3.4.16. Thus,

$$\dot{Q} = \eta_0 h A_{tot}\,(T_b - T_a) \tag{3.4.17}$$

being the term A_{tot} the total surface, considering base and fins, and T_a is the mean air temperature, calculated as the average between inlet and outlet temperatures. The overall surface efficiency can be modelled as

$$\eta_0 = 1 - \frac{A_f}{A_{tot}}\left(1 - \eta_f\right) \tag{3.4.18}$$

where A_f is the total fin surface and η_f is the efficiency associated to a fin. This parameter can be understood as the ratio between the heat that is dissipated by the fin compared to the value it could dissipate if the surface were at the same temperature as the base.

In this case, the resistance associated with conduction along the fins needs to be considered.

The general equation that defines the energy balance in generic extended surfaces under steady-state conditions, according to the terminology in Fig. 3.28, is

$$\dot{Q}_y = \dot{Q}_{y+dy} + d\dot{Q}_{conv} = \dot{Q}_y + \frac{d\dot{Q}_y}{dy} + d\dot{Q}_{conv} \tag{3.4.19}$$

Using Fourier's law to determine the conduction heat and Newton's law of convection cooling, equation 3.4.19 can be expressed as

$$0 = \frac{d^2T}{dy^2} + \left(\frac{1}{A_n}\frac{dA_n}{dy}\right)\frac{dT}{dy} - \left(\frac{1}{A_n}\frac{h}{k}\frac{dA_s}{dy}\right)(T - T_a) \tag{3.4.20}$$

A reasonable assumption that will allow an affordable analytical procedure is to consider that the geometry of the fins is rectangular, instead of trapezoidal, so the area does not change with the height.

In this case, $dA_n/dy = 0$ and $dA_s/dy = 2(L + t) = \Lambda$ is the perimeter of a constant height section of the fin. Thus, applying a transformation of the dependent variable T to $\theta(y) = T(y) - T_a$, equation 3.4.20 can be rearranged to:

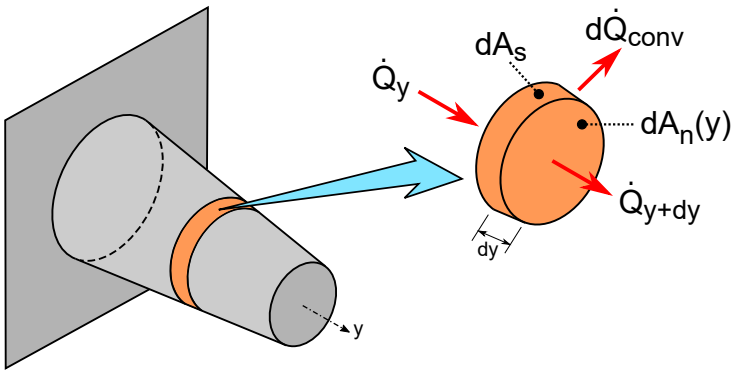

Figure 3.28: Energy balance in steady-state conditions in a generic extended surface.

$$\frac{d^2\theta}{dy^2} - m^2\theta = 0 \tag{3.4.21}$$

where

$$m^2 = \frac{h\Lambda}{kA_n} \tag{3.4.22}$$

Equation 3.4.21 is a linear, homogeneous, second-order differential equation with constant coefficients. The general solution of this equation is of the form:

$$\theta(y) = C_1 e^{my} + C_2 e^{-my} \tag{3.4.23}$$

It needs two boundary conditions to be solved. One of them is the temperature at the base of the extended surface, which is the same as the base temperature.

The second condition is imposed at the tip. Typically, it can be assumed that the heat exchange through the tip is negligible, so it can be considered adiabatic. Thus, the boundary conditions are:

$$\theta(0) = T_b - T_a = \theta_b \tag{3.4.24}$$

$$\left.\frac{d\theta}{dy}\right|_{y=H_f} = 0 \tag{3.4.25}$$

Solving equation 3.4.23 with these boundary conditions, the temperature distribution along the fin can be expressed as:

$$\frac{\theta}{\theta_b} = \frac{\cosh\left(m\left(H_f - y\right)\right)}{\cosh\left(mH_f\right)} \tag{3.4.26}$$

The specific interest of this procedure is to determine the total amount of heat that is exchanged by the whole fin. It is possible to derive from Fig. 3.28 that this value can be calculated with the amount of heat that enters through the base of the fin. Applying Fourier's law:

$$\begin{aligned}\dot{Q}_f = \dot{Q}_b &= -kA_f \left.\frac{dT}{dy}\right|_{y=0} = -kA_f \left.\frac{d\theta}{dy}\right|_{y=0} \\ &= \sqrt{hPkA_n}\,\theta_b \tanh\left(mH_f\right)\end{aligned} \tag{3.4.27}$$

Now that the heat dissipation through the fin has been defined, it is possible to establish the fin efficiency η_f from equation 3.4.18. As previously explained, the fin efficiency is the ratio between the actual dissipation rate and the possible maximum, which is equivalent to having a temperature equal to the base temperature in the whole fin surface. Hence,

$$\eta_f = \frac{\dot{Q}_f}{\dot{Q}_{max}} = \frac{\dot{Q}_f}{hA_f\theta_b} = \frac{\tanh\left(mH_f\right)}{mH_f} \tag{3.4.28}$$

Note that the assumptions made to determine the fin efficiency were that the fin is rectangular instead of trapezoidal and the heat released by the tip is negligible, so it can be considered adiabatic. Harper and Brown [161] proposed to modify the height of the fins in order to correct this last assumption.

The modification introduces a corrected height which is $H_c = H_f + t/2$, being t the fin thickness. This correction states that the heat transfer from an actual fin is equivalent to the dissipation in a fin which is slightly longer but has an adiabatic tip. As long as $(ht/k) \leq 0.0625$, this approach can be considered valid with negligible errors [162]. Therefore,

$$\eta_f = \frac{\tanh\left(mH_c\right)}{mH_c} \tag{3.4.29}$$

This procedure has been performed considering conditions on the air side, but an identical approach can be followed for the oil, which also features trapezoidal fins. The only difference is the energy flow, since the oil is hotter than the SACOC. Hence, equation 3.4.17 should be substituted by

$$\dot{Q} = \eta_0 h A_{tot}\left(T_o - T_b\right) \tag{3.4.30}$$

Now that the convective heat transfer has been defined, it is possible to analyse the heat transfer from a global perspective. A typical approach consists of assuming that the heat flux has to overcome a series of thermal resistances in order to be transmitted (when a one-dimensional condition is considered and no internal energy is generated).

Thermal resistance can be defined as the ratio between a driving potential that generates a temperature difference and the corresponding transfer rate. Therefore:

$$R_t = \frac{T_{hot} - T_{cold}}{\dot{Q}} \tag{3.4.31}$$

This is also applicable when there are several exchange processes that occur in series. In this case, schematised in Fig. 3.29, the heat is firstly transferred from the oil to the base of the heat exchanger by convection, then it is conducted within the exchanger to be finally transmitted to the air by convection. In the case depicted in Fig. 3.29:

$$\begin{aligned}\dot{Q} &= \frac{T_o - T_{o,b}}{1/\eta_0 h_o A} = \frac{T_{o,b} - T_{a,b}}{t_b/k_b A} = \frac{T_{a,b} - T_a}{1/\eta_0 h_a A} \\ &= \frac{T_o - T_a}{(1/\eta_0 h_o A) + (t_b/k_b A) + (1/\eta_0 h_a A)}\end{aligned} \tag{3.4.32}$$

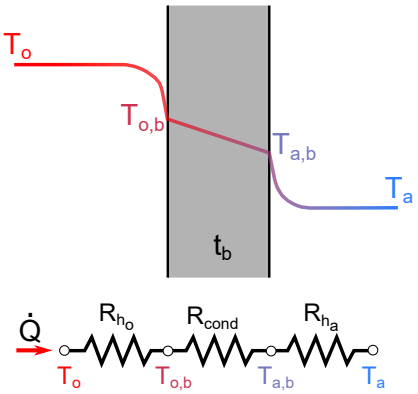

Figure 3.29: Thermal resistance analogy with the equivalent resistance circuit.

In these types of devices, it is convenient to define a term that embraces the whole thermal resistance and accounts for all terms. Thus, the overall heat transfer coefficient U can be understood as the complete thermal resistance of a heat exchanger:

$$U = \frac{1}{R_t A} = \frac{1}{(1/\eta_0 h_o) + (t_b/k_b) + (1/\eta_0 h_a)} \tag{3.4.33}$$

In order to determine the adequate performance of the heat transfer in a heat exchanger, the overall heat transfer coefficient has to be used carefully. Indeed, as the temperature difference between the hot and cold fluids varies with the location, the ΔT associated with this coefficient needs to be a rate of temperatures called Log Mean temperature difference ΔT_{lm}, explained in Section 3.4.2.2, and defined as

$$\dot{Q} = U A \Delta T_{lm} = UA \frac{(T_{2o} - T_{2a}) - (T_{1o} - T_{1a})}{\ln \frac{T_{2o} - T_{2a}}{T_{1o} - T_{1a}}} \tag{3.4.34}$$

Following the same criteria as in Section 3.4.2.2, subindices 1 and 2 refer to fins leading and trailing edge (from the air perspective), and o and a stand for the oil (hot fluid) and the air (cold fluid).

Equations 3.4.17, 3.4.33 and 3.4.34 can now be solved iteratively. The result will be a series of pairs of possible heat transfer coefficients (one for the air and one for the oil) as functions of the base temperature that satisfy the heat exchange conditions. Figure 3.30 represents these pairs of values as functions of the base temperature. Thus, with the base temperature measured with the IR camera, the problem can be closed and the Nusselt number and the Colburn j factor can be straightforwardly derived.

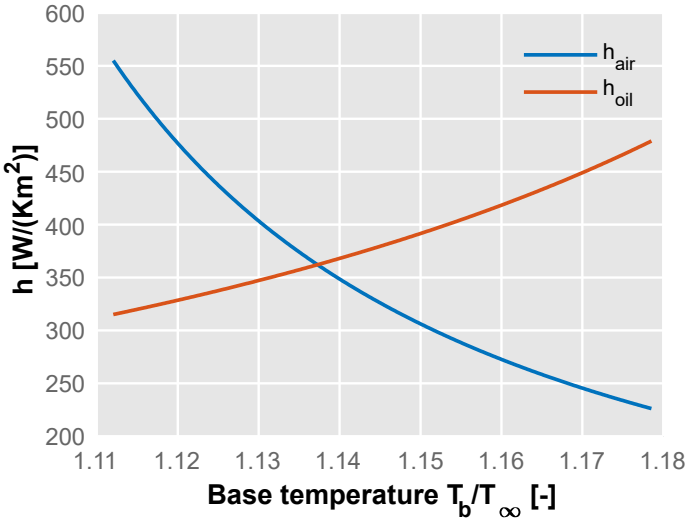

Figure 3.30: Pairs of convective heat transfer coefficients which depend on the base temperature and satisfy the equations.

3.5. Uncertainty analysis

During an experimental characterisation, there are several sources of uncertainty that lead to not being able to guarantee the absolute truthfulness of a value. The main sources of uncertainty are generally caused by [163]:

1. Spatial and temporal variability.

2. Statistical error/random variation of replicate measurements.
3. Uncertainty in the form of the function that relates the quantity of interest with other quantities.
4. Systematic error (bias).
5. Imprecise definition or unrepresentativeness of samples.

The last three sources cannot be captured by any general approach, so they have to be worked on to be reduced as much as possible and they can be assumed to be negligible compared to the other two.

Anyhow, calculating the uncertainties of a derived quantity can be very complicated. Some considerations can be made in order to simplify the procedure without losing generality [164]. As long as the standard deviation σ is small compared to the mean value, orders above the σ^2 can be neglected, and if the number of samples is large enough, the data distribution can be assumed to be normal (at least, bell-shaped). Moreover, if the derived quantity depends on different variables, they are considered not to be correlated.

With these considerations in mind, the standard deviation of a derived quantity g that depends on n different variables x can be defined as:

$$\sigma_g = \sqrt{\left[\sum_{i=1}^{n} \frac{\partial g}{\partial x_i} \sigma_{x_i}\right]^2} \tag{3.5.1}$$

Hence, Table 3.3 collects the typical values of the uncertainties from direct and derived measurements. The sub-indices refer to the measurement technique applied or serve as a distinction between air and oil.

Table 3.3: Summary of estimated experimental uncertainties.

Primary measurements		**Derived quantities**	
Parameter	Uncertainty	Parameter	Uncertainty
Δp	1%	f	1.1%
P_{Kiel}	0.2%	V	2.3%
V_{LDA}	0.11%	Re	1.5%
$\dot{m}_a$	1.47%	$\dot{Q}$	1.56%
$\dot{m}_o$	1%	U	2.05%
T_a	0.5 K	Nu	6.47%
T_o	0.1 K	j	6.55%
T_{IR}	2 K		

3.6. Summary and conclusions

This chapter has explored the methodology to be used in the experimental determination of heat exchangers' performance. Overall:

- The facilities have been introduced, presenting the HMHT flow bench used to deliver a controlled amount of air, the specifics of the wind tunnel design (providing a detailed explanation of the test section) and the oil conditioning system operations. This facilitates the understanding of the actual physical phenomena that take place during the characterisation.
- An extended explanation of the techniques applied has been presented divided into intrusive and optical techniques, commenting on the principles behind the methods. This section highlights the main advantages and limitations of each technique.
- The data acquisition and reduction procedures have been explained. There are different approaches depending on the technique applied and the main purpose of the measurement.
- Besides, several metrics used during the post-processing have been introduced. These metrics will allow the performance of different heat exchangers to be accurately evaluated.
- The uncertainties of each parameter have been commented on, either if they are directly measured or derived from others, explaining the main sources of uncertainty and how to compute them.

The main outcome of the chapter is the possibility to experimentally characterise heat exchangers by applying the correct methodology to adequately derive the main parameters of their performance with reasonable uncertainty levels.

CHAPTER 4

Velocity distribution generation

The use of a wind tunnel for experimental characterisation of heat exchangers is a much more reasonable option than performing in-engine measurements thanks to its adaptability, the possibility of introducing specific instrumentation and, of course, the much lower operating costs as well as a reduced duration of the test campaigns.

Nevertheless, as previously commented, the main problem with testing in small-scale wind tunnels is the difference in the typical velocity distribution around the heat exchanger under real operating conditions.

In light of these considerations, the design and application of accurate distortion screens during tests appear to be a necessity. Furthermore, as wind tunnels typically present tight time slots (and keeping in mind always the cost), it is desirable to develop a procedure that automatically designs the distortion panel once the target pressure distribution is known.

In this chapter, an automatised procedure for the design of distortion screens is proposed. To this end, a mathematical model to derive the final geometry of the panel that produces the desired velocity distribution is presented, followed by three target examples: two 1D distributions to prove the feasibility of replicating different velocity profiles, and one 2D distribution to exploit the complexity that can be achieved with distortion screens. Then, a preliminary CFD analysis is performed to confirm the theoretical predictions and finally, the results are experimentally validated.

Work on this chapter has been partly published in the following paper:

- An automatized methodology to generate velocity distortion panels for wind tunnel testing [3]

4.1. Methodology for an automatic geometry generation

There are several different ways to generate a desired flow pattern in wind tunnels. However, when a relatively small wind tunnel is considered, the application of distortion screens is highly versatile as it can generate complex velocity distributions.

In order to design a distortion screen, the geometrical parameters are derived using a methodology based on the work of Overall [144]. Assuming that the flow is isentropic, a mathematical algorithm calculates the required panel porosity distribution, considering certain input conditions selected by the user. Then, the final geometry is derived from that porosity, considering hexagonal pores in the mesh.

This is because this type of geometry discretisation produces the lowest pressure drop across the screen [165] (which avoids excessive pressure loads that might turn into the failing of the panel during tests [166]). Finally, the resultant geometry can be easily manufactured via 3D printing (AM), automating hence the whole process.

4.1.1. Pressure drop model

Prior to the development of the design methodology, there are certain assumptions that need to be clarified. The flow field upstream of the panel is considered to be uniform and with constant velocity and pressure in the whole section. Besides, the air is assumed to undergo an isentropic evolution through the holes, presenting a constant and uniform static pressure downstream.

The hexagonal patterns of the grid begin with a base of regular hexagons uniformly distributed with the same side. Then, the screen is divided into a certain number of identical cells and, depending on the porosity S of each of these cells, the final locations of the pores vertices are determined. The thicknesses t of the walls need to be considered to end up with the desired flow area A_f in each cell. This can be seen in Fig. 4.1.

Thus, there are four inputs required to determine the geometry:

1. Static pressure downstream of the panel p_2.
2. Height and width of the wind tunnel cross-section H.
3. Number of cells along the vertical length.
4. Maximum porosity S_{max}.

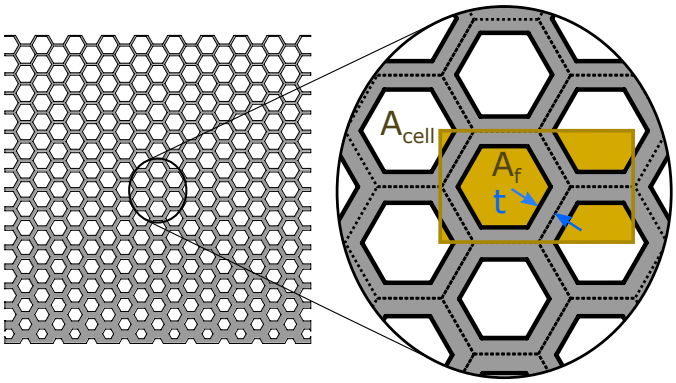

Figure 4.1: Example of hexagonal distortion screen geometry and detail with nomenclature.

Since the final goal of this procedure is to generate a specific total pressure drop that implies a certain velocity distribution, this target velocity distribution V_2 has to be provided too as input. The algorithm selects the values of the velocity for the calculation from the data contour based on the discretisation selected.

Once the discretised velocity $v_{2_{i,j}}$ is known, and with the input static pressure, the total pressure and the correspondent mass flow through each cell can be computed through the well-known isentropic, compressible flow relations:

$$P_{02_{i,j}} = p_2 \left(1 + \frac{\gamma - 1}{2} \frac{v_{2_{i,j}}^2}{\gamma R \left(T - \frac{v_{2_{i,j}}^2}{2C_p} \right)} \right)^{\frac{\gamma}{\gamma - 1}} \tag{4.1.1}$$

$$\dot{m}_{i,j} = A_{cell} P_{02_{i,j}} \sqrt{\frac{2\gamma}{RT(\gamma - 1)} \left[\left(\frac{p_2}{P_{02_{i,j}}} \right)^{\frac{2}{\gamma}} - \left(\frac{p_2}{P_{02_{i,j}}} \right)^{\frac{\gamma+1}{\gamma}} \right]} \tag{4.1.2}$$

Here, P_{02} and p_2 are the total and the static pressure downstream the panel respectively, $\dot{m}$ is the mass flow, A_{cell} is the area of the cell (uniform for all the panel), and the subscripts i, j represent each one of the cells in the z and y directions. As commented in the model assumptions, the static pressure is uniform across the section. The total mass flow will obviously be the sum of that of each cell:

$$\dot{m} = \sum_i \sum_j \dot{m}_{i,j} \tag{4.1.3}$$

From this point, an iterative process begins. Firstly, one needs to guess an average porosity of the screen. An empirical method was proposed by Ecker et al. [132], which estimates the total pressure loss K through thin honeycomb systems. Thus,

$$K = 0.214\left(\frac{\epsilon}{D_h}\right)^{0.4}\left(3+\frac{\lambda}{D_h}\right)\frac{1}{\bar{S}^2}+\left(\frac{1-\bar{S}}{\bar{S}}\right)^2 \tag{4.1.4}$$

where ϵ is the absolute roughness of the panel walls, D_h is the hydraulic diameter of the hexagonal cells, λ is the thickness of the panel in the flow direction and $\bar{S}$ is the average porosity.

The next step consists of guessing the static pressure upstream of the screen and deriving the total pressure with the calculated maximum mass flow:

$$\dot{m}_{max} = A_{free,max}\, p_1 \frac{\sqrt{\frac{2}{RT}\frac{\gamma}{\gamma-1}\left[1-\left(\frac{p_1}{P_{01}}\right)^{\frac{\gamma-1}{\gamma}}\right]}}{\left(\frac{p_1}{P_{01}}\right)^{\frac{\gamma-1}{\gamma}}} \tag{4.1.5}$$

being the $A_{free,max}$ the largest free area, which will be the place where the maximum amount of mass flow is going through. It is derived from the maximum selected porosity S_{max}:

$$A_{free,max} = A_{cell}\, S_{max} \tag{4.1.6}$$

It is indeed critical to select an adequate maximum porosity, since the higher the porosity the higher the free area of the whole screen will be, presenting hence a lower pressure loss.

However, a value which is too high may result in problems related to structural integrity such as vibrations or cracks, that could ultimately lead to its breakage. Moreover, the resolution of the printer to be used during the manufacturing is something that also needs to be considered when choosing the maximum porosity.

With both pressures upstream of the screen and using the isentropic equations for compressible flow, the velocity in this region and, therefore, the dynamic pressure, can be calculated:

$$\frac{P_{01}}{p_1} = \left[1 + \frac{\gamma - 1}{2} \frac{v_1^2}{\gamma R\left(T - \frac{v_1^2}{2C_p}\right)}\right]^{\frac{\gamma}{\gamma - 1}} \tag{4.1.7}$$

Now, the inner iteration loop is checked by comparing the new total pressure loss with the one obtained from the empirical model. The new total pressure loss is defined as:

$$K' = \frac{P_{01} - \bar{P}_{02}}{P_{01}} \tag{4.1.8}$$

Since the total pressure downstream of the panel varies depending on the local porosity, the average $\bar{P}_{02}$ is used for the computation. The new static pressure upstream of the screen considered, if a certain convergence criterion is not reached, is calculated from:

$$p_1 = \frac{\bar{P}_{02}}{\left[1 + \frac{\gamma - 1}{2} \frac{v_1^2}{\gamma R\left(T - \frac{v_1^2}{2C_p}\right)}\right]^{\frac{\gamma}{\gamma - 1}}} - \frac{K v_1^2}{2R\left(T - \frac{v_1^2}{2C_p}\right)} \tag{4.1.9}$$

After achieving the convergence in the pressure loss factor, the individual porosity of each cell can be computed straightforward:

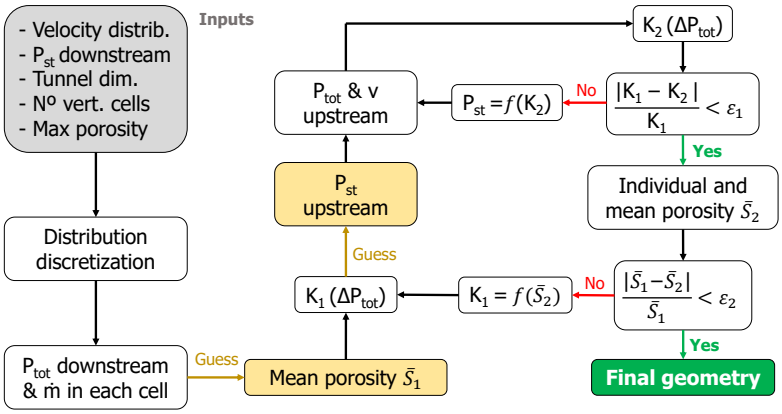

Figure 4.2: Flow diagram of the pressure drop model that generates the geometry.

$$S_{i,j} = \frac{\frac{\dot{m}_{i,j}\sqrt{T}}{A_{cell}\,P_{01}}}{\sqrt{\frac{2\gamma}{RT(\gamma-1)}\left[\left(\frac{p_2}{P_{02_{i,j}}}\right)^{\frac{2}{\gamma}} - \left(\frac{p_2}{P_{02_{i,j}}}\right)^{\frac{\gamma+1}{\gamma}}\right]}} \tag{4.1.10}$$

The last check is now performed for the first loop. The average porosity is computed and compared against the guess used in the first place. If a convergence criterion is met, the algorithm generates the geometry automatically. Otherwise, the whole process is restarted with the new averaged porosity. This process is summarised in Fig. 4.2.

4.1.2. Geometry generation

Once the pressure model is converged, the proposed algorithm generates the mesh that reproduces the calculated porosity distribution $S_{i,j}$. A cloud of points is distributed on the surface of the screen, representing the location of the vertices from the base regular hexagons the panel has been discretised into.

The horizontal and vertical coordinates of the points follow a repetitive pattern that responds to the equations:

$$x_i = x_{i-1} + l_{cell}\frac{1-(-1)^i + \cos 60^\circ\left[1+(-1)^i\right]}{2} \tag{4.1.11}$$

$$y_j = y_{j-1} + \frac{h_{cell}}{2} \tag{4.1.12}$$

where l_{cell} and h_{cell} are the horizontal length and height of the cell. It is important to notice that all y_j coordinates are the same in each column and so are the x_i in every row. It has been considered that $x_1 = y_1 = 0$.

Note that, in this context, the x and y coordinates do not correspond to those used in the wind tunnel, but to a specific frame of reference associated with the distortion screen.

From this basic geometry distribution, the new location of the vertices from the interior side of the hexagons (that correspond to the pores to be manufactured) can be found, considering the relative thickness of each cell $t_{i,j}$. Fig. 4.3 represents a sketch that illustrates how the final geometry is generated from the base vertices depending on the thickness of each cell.

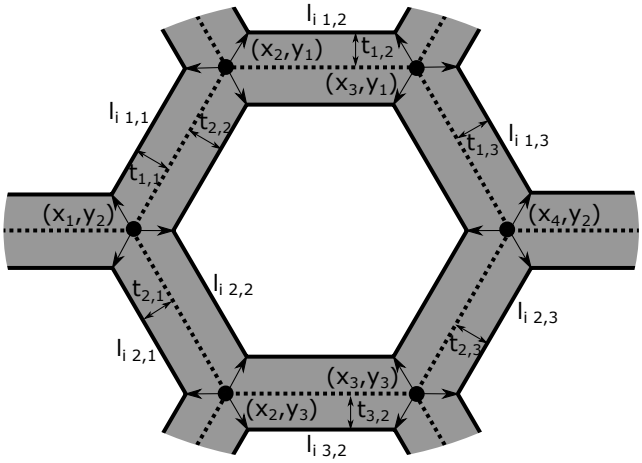

Figure 4.3: Sketch of the movement from the base grid vertices distribution to their final location depending on the thickness of each cell.

Once all vertices have been distributed along the surface, the x and y coordinates are stored in two different matrices where each column represents each hole, e.g. the first pore will have its vertices coordinates $(x_i, y_i)_1$ in the first column of each one of the matrices. Of course, the number of columns will be the same as the number of pores.

Both matrices are exported then as a DXF file, which can be read by most CAD software and imported as curves in a plane. The last step consists of extruding and cutting the geometry, in addition to tailoring the panel to be fixed in the wind tunnel.

There are two aspects to consider in the design process. On one hand, the height of each repetitive cell is obtained by dividing the height of the tunnel into the specified number of discrete cells. For this reason, as the aspect ratio of the cells is necessarily fixed, the horizontal length of the cells may not perfectly fit the horizontal side of the tunnel, so the whole pattern is shifted to be centred in the section. This implies that the cells close to the lateral walls may not have the exact porosity as calculated, but this effect is considered to be negligible.

On the other hand, one can consider the existence of two types of hexagons, which appear in Fig. 4.1. The left hexagon, that is completely inside the cell, and two half-hexagons, which are included in different cells on the right. Obviously, the hexagons that are completely included in the cell present the calculated thickness of that cell.

However, in order to generate regular hexagons, those that are included in several cells present an average thickness of those cells they are included in. This assumption is valid as long as the contours of the velocity are smooth.

4.1.3. Distortion screen manufacturing

At the end of the day, the final purpose of the automatic design is to be implemented experimentally, so one of the main steps to consider is the manufacturing of the final geometry. The availability and maturity of additive manufacturing technologies [167], together with its many advantages, puts this type of manufacturing at the top of the list.

Although there are several options for AM, maybe the most extended principle is Fused Deposition Modelling (FDM), where an extruder head fuses and deposits filaments of thermoplastic layer after layer. Professional-grade FDM 3D printers are not particularly expensive and can be easily found in many research laboratories and workshops.

There are other popular AM techniques, such as Stereolithography (SLA) or Selective Laser Sintering (SLS), but professional or industrial-grade machines of these types are still less readily available at workshops.

For this case, a Stratasys F170 professional-grade FDM printer was used to manufacture the geometry in thermoplastic, specifically, ABSplus. The minimum layer height to which this printer is capable to operate is 0.13 mm, which can also be considered as the minimum thickness of the wall.

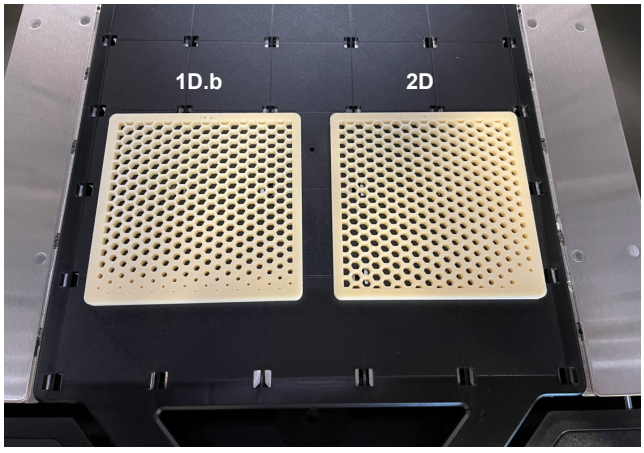

Figure 4.4: Two of the distortion screens 3D-printed in ABS using FDM. These correspond to geometries 1D.b and 2D described in subsection 4.1.4.

This value needs to be taken into account when deciding the maximum porosity of the distortion panel and the resolution in the thickness variation. It is recommended that confined, temperature-controlled build chambers are used to avoid warping when using ABS-type materials. Two sample distortion screens are shown in Fig. 4.4 once the AM process is completed.

Considering the properties of the AM material, the printing principle and the available resolution, a trade-off between pressure loss and mechanical performance must be reached. In this respect, due to the intrinsic anisotropy of FDM printing, the stresses need to be adequately aligned with the corresponding axes in order to avoid delamination and to ensure optimum load bearing.

Other aspects to consider are heat deflection and chemical resistance, particularly in closed wind tunnels with smoke-based streamline visualisation or seeding for laser instrumentation. Under these circumstances, some other techniques could be applied such as CNC machining or laser/water cutting. In any case, AM typically provides good results in a fast and affordable way.

4.1.4. Velocity distribution targets

Three different velocity distributions are going to be evaluated in order to verify the proposed methodology. Two of them are 1D velocity variations which intend to replicate certain velocity profiles associated with a developed boundary layer, whereas the third one consists of a 2D velocity distribution.

Briefly described, the one-dimensional cases are 1D.a and 1D.b, being the former a relatively smooth boundary layer still in development and the latter a more severe boundary layer that is already developed in the uppermost region. For the bi-dimensional case, a diagonal velocity gradient from one corner to the opposite one has been chosen.

Figure 4.5 represents the target velocity distributions (the contour in the left-most image and the profile in the centre) and the obtained geometries for each case. The velocity values are non-dimensionalised with the maximum velocity U_∞ of the velocity profile 1D.a. It is important to notice that the velocity distributions are idealised, i.e., there is no consideration of boundary layers close to the walls. The actual 3D printed screens to replicate the 1D.b and 2D targets were shown in Fig. 4.4.

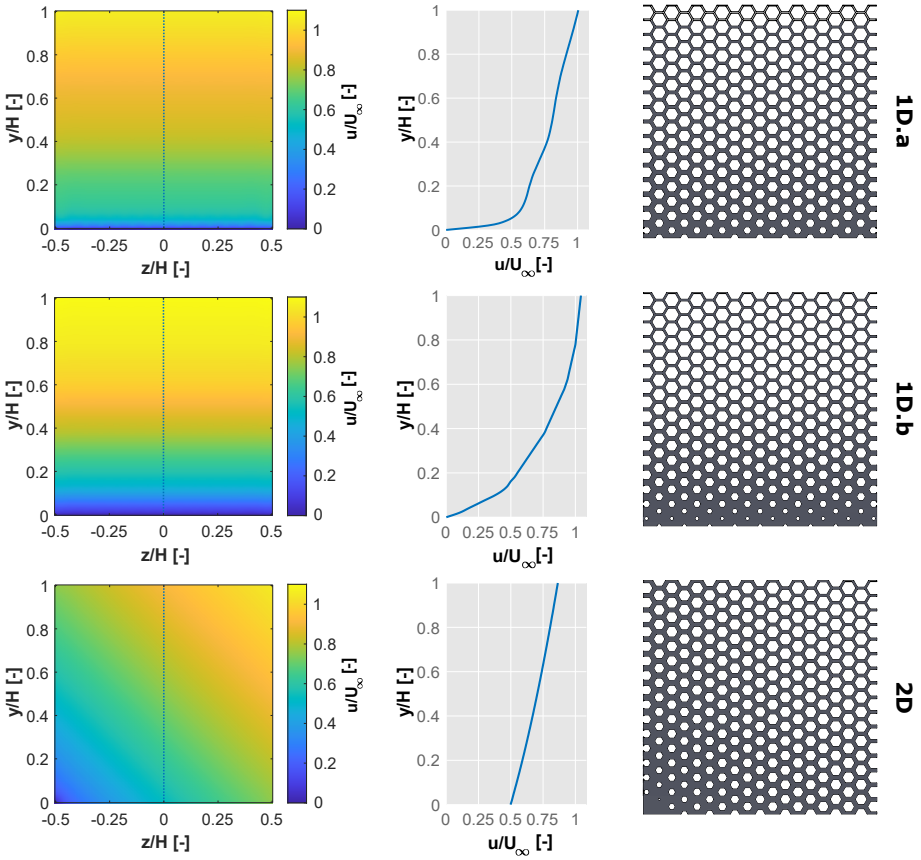

Figure 4.5: On the left, velocity distributions targeted in the cases 1D.a, 1D.b and 2D. Centred, magnitude of the axial velocity along the vertical centre line (displayed as a dotted line in the contours). On the right, the outcome geometry from the analytical process to generate each velocity distribution.

4.2. Numerical simulations

A numerical analysis is carried out using CFD to determine the accuracy of the analytical design process and to better understand the behaviour of the flow downstream of the proposed distortion screens. The three different targets of velocity distribution indicated earlier will all be taken into account using the same numerical setup.

4.2.1. CFD setup

The simulation is run using the finite volume method-based CFD solver STAR-CCM+. Conservation of mass, momentum, and energy are the equations that determine the flow characteristics. The remaining non-dimensional equations that need to be solved are the following, presuming that air is an ideal compressible gas in steady-state and turbulent conditions:

$$\frac{\partial \rho u_i}{\partial x_i} = 0, \tag{4.2.1}$$

$$\frac{\partial \rho u_i u_j}{\partial x_j} = -\frac{\partial p}{\partial x_i} + \frac{\partial}{\partial x_j}\left[\frac{1}{Re}\left(\frac{\partial u_i}{\partial x_j} + \frac{\partial u_j}{\partial x_i}\right) - \rho\overline{u_i' u_j'}\right], \tag{4.2.2}$$

$$\frac{\partial \rho u_i T}{\partial x_i} = \frac{\partial}{\partial x_i}\left(\frac{1}{RePr}\frac{\partial T}{\partial x_i} - \rho\overline{u_i' T}\right) \tag{4.2.3}$$

where Re and Pr are the Reynolds and the Prandtl number, defined as $Re = V_1 H/\nu$ and $Pr = C_p \mu / k_f$, being H, ν, C_p, μ and k_f the height of the tunnel, the kinematic viscosity, the specific heat coefficient, the dynamic viscosity and the conductivity, respectively.

The turbulence in the control volume is modelled using a Reynolds-Averaged Navier Stokes (RANS) method. For this, a $k-\omega$ SST [168] with a Gamma turbulent transition scheme is chosen. This particular model was selected because it employs a pure $k-\omega$ approach in the inner boundary layer, regarded as a Low-Re turbulence model, and does not require any damping function close to the walls.

In order to eliminate the normal susceptibility of $k-\omega$ models to the freestream turbulence features, it switches to a k—ϵ model as the flow moves away from the walls. Additionally, the model predicts a better behaviour when the boundary layer is exposed to unfavourable pressure gradients by assuming that the primary shear stress is proportional to the turbulent kinetic energy.

The Gamma transition model reduces the complexity of the GammaRe-Theta transition, which has two equations: one for the transition momentum thickness Reynolds number and another for intermittency. However, some coefficients must be specifically calibrated in a time-consuming process, so the simplified model avoids the Re_θ equation and is calibrated against a sizeable number of Falkner-Skan flows under various test conditions [169]. An implicit second-order upwind discretisation approach has been employed with a coupled flow solver.

The control volume is a square duct 6-hydraulic-diameters long that extends 4 diameters downstream from the panel and begins 2 hydraulic diameters upstream of it. By doing this, the incoming flow can develop before it reaches the screen, and the panel's impact can also be taken into account upstream. Additionally, the distance downstream of the gauze makes it possible to estimate how long the influence will last in the distorted flow.

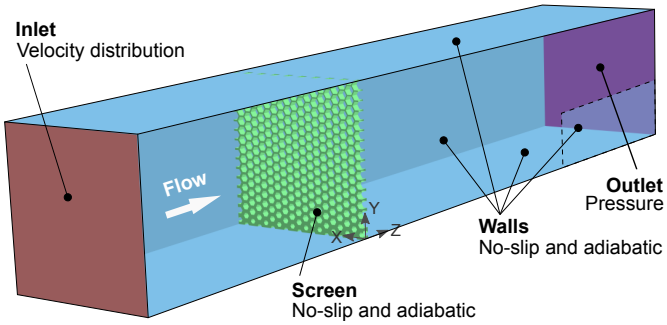

Figure 4.6: Schematic of the computational domain with its boundary conditions.

The boundary conditions that are used to validate the simulation were chosen to replicate the experimental settings. The static pressure used for the outlet condition is the ambient pressure frequently found during the experiments, and the velocity distribution measured without the distortion screen is imposed in the inlet. Since there are no heating sources in the problem, it is assumed that the case is adiabatic and the temperature is adjusted to 300 K at the inlet and outflow. No-slip conditions are used on all of the domain's walls, including those from the tunnel and those related to the distortion screen. In Fig. 4.6, a sketch representing the simulation domain as well as the imposed boundary conditions can be seen.

The initial stage in a CFD setup is to carry out a mesh independence investigation. To do this, the 1D.a case is used, and the outcomes obtained in terms of independent mesh parameters and properties are used in the other two cases. Depending on the number of cells utilised, Figure 4.7 shows the values of the mass flow and the pressure drop between the domain's inlet and outlet. It is apparent that the pressure decrease in the instances of 2 and 3 million cells is essentially the same. Additionally, the results obtained in those circumstances are constant in terms of mass flow.

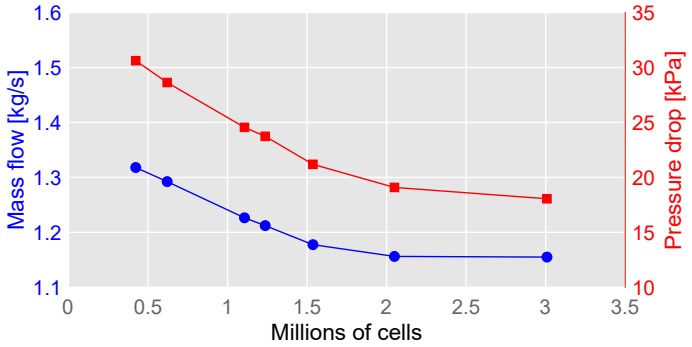

Figure 4.7: Mesh convergence study comparing values of mass flow (blue points, left axis) and pressure drop (red squares, right axis) as a function of the number of cells.

The final mesh layout contains slightly more than 2 million cells as a result of this analysis. In the final configuration, three distinct volumetric control regions in the screen's vicinity adjust the mesh size. Although the majority of the final mesh is made up of polyhedral unstructured cells, there is a transition towards prismatic cells parallel to the walls adjacent to the walls in order to solve the boundary layer more effectively.

In order to resolve the viscous sublayer adequately, which has a major impact on the operation of the distortion panel (particularly for the smaller holes), the size of the cells is reduced close to the walls aiming to obtain values of $y^+ \leq 1$ on all walls and, in particular, on the screen. It is important to note that values in the range of 25% of the base size are attained near the screen using the three distinct volumes employed to refine the size of the cells.

These volumes are imposed to provide a smooth transition to the narrower mesh and to improve spatial resolution, mostly in the region downstream of the panel (since the wake generates turbulence on small scales) but also

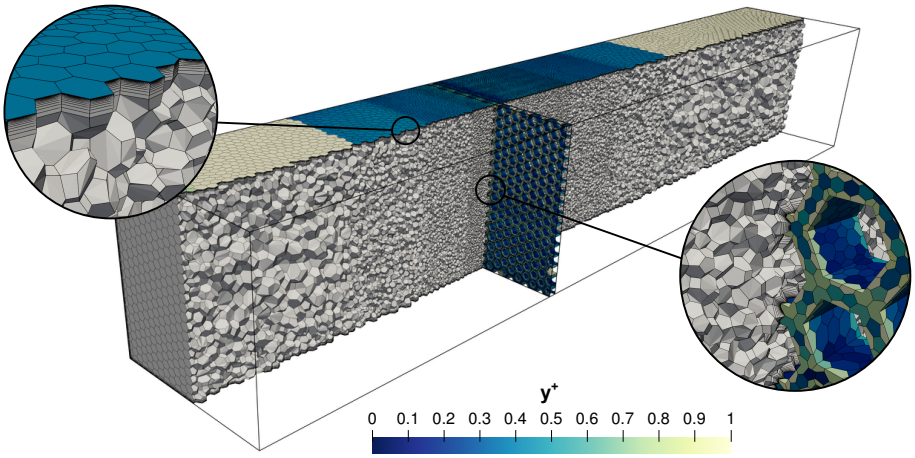

Figure 4.8: Final 2-million-cell mesh with mesh details close to the tunnel walls and around the distortion screen, coloured by y^+.

in the upstream region because the flow field is also slightly disturbed as it approaches the screen. The finished mesh layout with details in the walls and the area around the distortion screen is shown in Fig. 4.8.

4.2.2. Numerical results and discussion

Results will first be analysed along the centre line and evaluated against the targets. After the screen, the turbulent and mixing region must settle and achieve uniform conditions in order to capture adequate steady values. Typically, this scenario is reached two hydraulic diameters downstream of the panel, so from that point on is where the data is analysed.

The velocity profiles for the different situations are shown in Fig. 4.9 along with their deviation when comparing the CFD results with the targets. It should be noted that all profiles exhibit large deviations from the objective in the higher and lower areas.

This happens because the theoretical tops of the profiles do not take into account that velocity approaches zero close to the walls and inevitably forms a boundary layer with low velocities. In the lower part, the fact that velocities are low has an impact on the deviation because, as a result, a tiny difference from a slow target results in a high percentage deviation. Additionally, it is not taken into account in the theoretical target for the 2D case that velocity will be zero at the bottom.

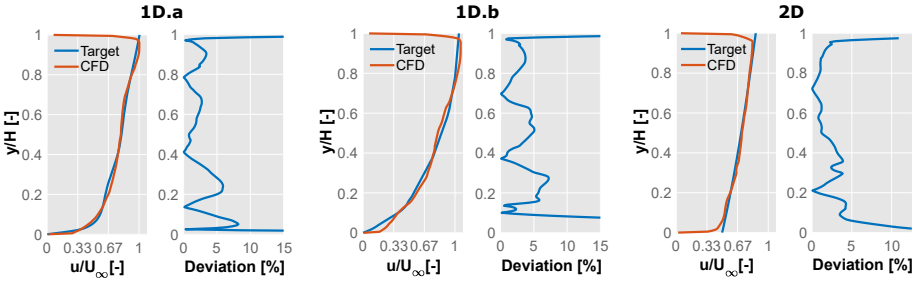

Figure 4.9: Comparison of the target velocity profiles and the results obtained in CFD two hydraulic diameters downstream of the distortion screen with the deviation between them.

With only a small amount of oscillation around the target values, the 1D.a scenario exhibits a very good match for the whole channel height. Anyway, as the deviation graph demonstrates, the differences between the two profiles are normally less than 3%, with the exception of a few locations near the bottom where they can reach 7%.

While still following the target trend, the CFD results for the 1D.b scenario exhibit greater swings than those for the first case. This is also evident in the larger deviation levels, which can reach values of 5%. Furthermore, the simulation outcomes in the bottommost region do not follow with high accuracy the trend, presenting higher values, which results in larger deviation values at higher values away from the bottom.

Last but not least, the profile in the 2D case is reproduced with great accuracy throughout nearly the entire height and is relatively stable. This translates into extremely low deviations always under 5% excluding the region's top and bottom, as the CFD takes into account the presence of a boundary layer that the theoretical target does not.

The velocity contours downstream of the screen are also worth analysing. It is clear that in the case of the 2D distribution, an accurate reproduction of the centre velocity profile (as shown in Fig. 4.9) is desirable, but its crucial feature is its capacity to reliably reproduce a bi-dimensional velocity distribution. Additionally, it is also interesting to analyse how the velocity profiles in the one-dimensional situations behave over the entire section.

For this reason, the values of the target velocity distributions and the numerically obtained velocity distributions are shown in the first two columns of Fig. 4.10, and the values of the deviations between the two are shown in the last column. In order to see the distribution in the majority of the section, it must be noted that the deviation values are capped at 10%.

It is important to mention that the screen's behaviour and, consequently, its performance are significantly influenced by the distribution of the incoming flow. This means that the CFD model may consider the real velocity that was observed in the experimental wind tunnel as opposed to the analytical model's assumption of an idealised, constant inlet velocity distribution.

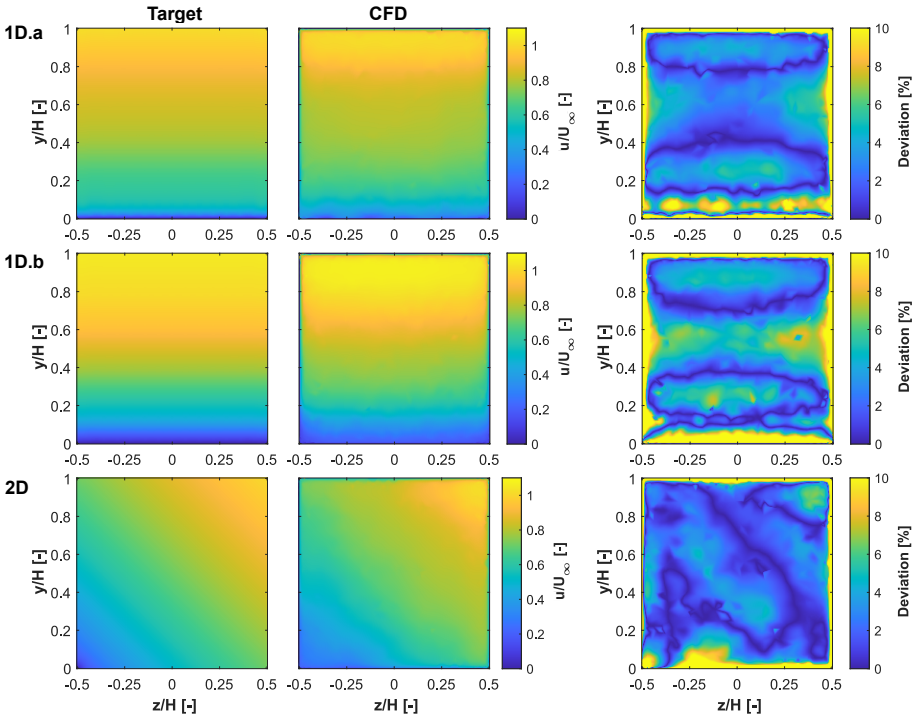

Figure 4.10: Comparison of the target velocity contours and the results obtained in CFD two hydraulic diameters downstream of the distortion screen with the deviation between them.

The first velocity distribution of Fig. 4.10, the 1D.a case, is considerably similar to the target, and the values appear to be uniformly distributed along the horizontal axis, though it is possible to see that the changes in velocity do not happen as uniformly as they do in the target but rather in a blurrier transition. Because of the boundary layer, the deviation in this case is also rather constant horizontally, with values typically under 4%, with the largest values near the bottom and in the vicinity of the walls.

The outcomes in the 1D.b case are very similar. The numerical findings show reasonably high horizontal uniformity and are fairly similar to the target, with slightly quicker velocities in the bottom as seen in Fig. 4.9. The deviation is a little higher here, although it is generally around 6%, with the exception of the lower zone and areas along the walls, where it is higher.

Anyhow, the most interesting case to analyse is the 2D distortion screen. The estimated velocity shows a bi-dimensional distribution that closely resembles the target, with its clear diagonal pattern created by the distortion screen. In fact, when examining the deviation contour, the values are often in the range of 3 to 4%, with the exception of the area in the lower-left corner of the section where lower target velocities are sought. It is important to keep in mind that the velocity distribution has limitations with regard to spatial changes in velocity and may not function properly if these changes are too abrupt or if, as in this instance, there is a difference of two orders of magnitude between one corner and the opposite one.

A final comment to make about Fig. 4.10 is the distribution of regions with identical or highly comparable deviation values. These iso-deviation values are distributed primarily in horizontal patterns in the one-dimensional cases and mainly in diagonals in the two-dimensional case.

After considering the resultant velocity distribution, it is crucial to ascertain how long this disruption will last. The development of the velocity profile produced along the centre line at different hydraulic diameters (D_h) is shown in Fig. 4.11. The closest distances exhibit a tendency to mimic the final velocity profile (left plot), but the disturbances brought on by the screen and the mixing region are still fairly noticeable.

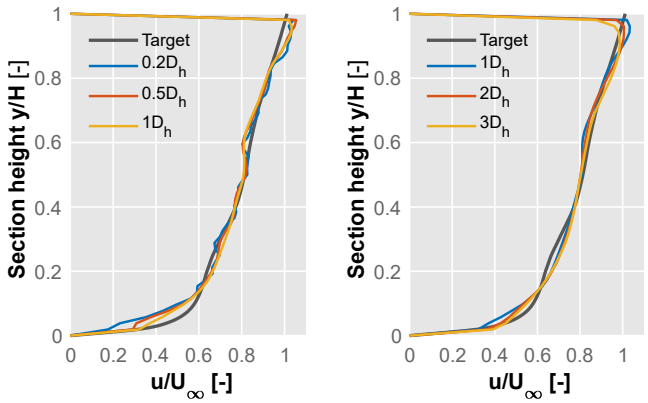

Figure 4.11: Evolution of the velocity profile at different hydraulic diameters downstream the distortion screen.

However, the results are significantly smoother when looking at the profiles located more downstream (see right plot), and the final distribution is practically settled after one hydraulic diameter. On the other hand, the distorted velocity seems to be stable and keeps its shape downstream after two and three hydraulic diameters.

Turbulence is created by the distortion screen's interaction with the fluid in addition to the velocity field being modified by variations in the pressure drop. The evolution of the turbulent kinetic intensity (TKI) in the domain for each case is shown in Fig. 4.12. As can be observed, the downstream flow has higher TKI values in the area where the gauze porosity is lower (smaller orifices) while the incoming flow displays a rather low and uniform field.

In fact, the larger values can be detected in the 1D.b scenario, where there is a considerable zone of low porosity. A region of very low porosity can also be distinguished in the 2D case, which has huge TKI values downstream of the region where the speed reduces significantly. However, when the flow moves further away from the distortion panel, the turbulent peaks diminish to values that are more evenly distributed throughout the section.

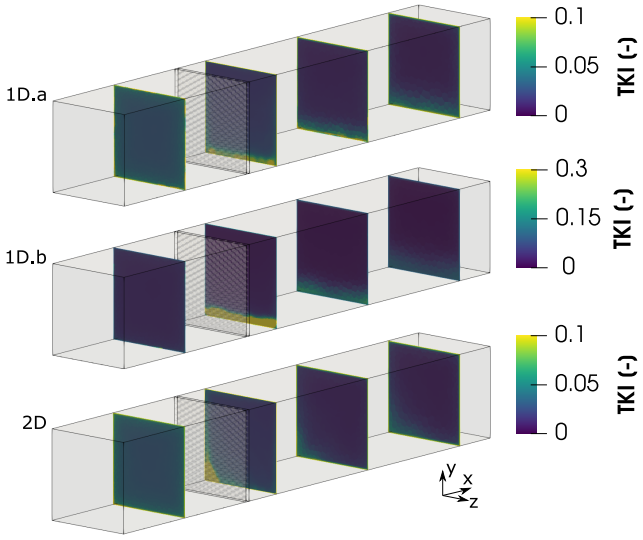

Figure 4.12: Evolution of the turbulent kinetic intensity (TKI) across the numerical domain.

A honeycomb straightener-like behaviour of the screen is found in zones with large porosity since the turbulence after the panel is reduced relative to upstream values. This is a consequence of the velocity distortion process that can be useful in some circumstances.

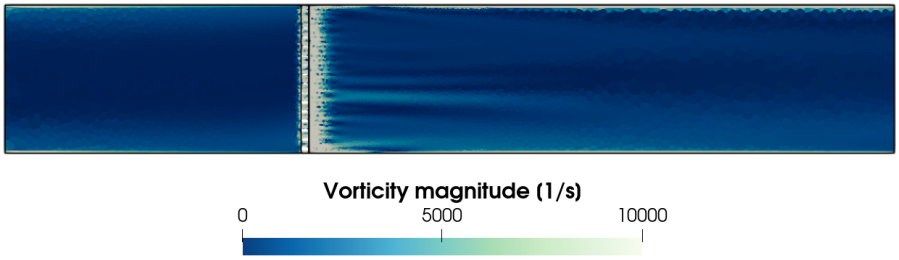

Figure 4.13: Evolution of the vorticity in the longitudinal central plane across the numerical domain.

Additionally, it emphasises how crucial it is to leave enough space downstream after the distortion screen so that the flow may develop properly. It can also be seen by plotting the vorticity magnitude (Fig. 4.13) that it increases just downstream of the screen relative to the initial freestream conditions, but that by the time the flow reaches the domain's outlet, these vortical structures have dissipated and the flow has returned to vorticity conditions similar to those at the inlet.

4.3. Experimental validation

Although CFD analysis may offer a precise understanding of the behaviour of the flow, it is critical to evaluate them against experimental counterparts because models and significant assumptions are made when creating a simulation. To do this, the three suggested geometries have been manufactured and set up in the wind tunnel.

The velocity fields have been measured in the UMS1 section, which is 2.3 hydraulic diameters downstream of the distortion panel. Kiel probes have been used for the experimental characterisation, moved with the 2D traverse system in a grid of 20 × 20 points.

With this configuration, all three distortion screens were tested at their respective nominal flow rates.Note that the input boundary condition for the numerical simulations is the velocity distribution that was obtained in this section without distortion screens, following the same procedure.

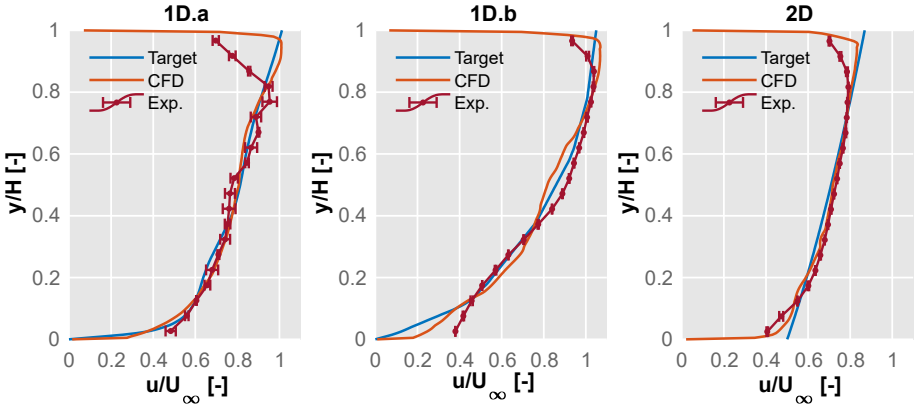

Figure 4.14: Experimental validation of the velocity profiles, comparing the values from the experiments, the numerical simulation and the target for each case. Error bars in the experimental data show the standard deviation for different measurement runs (two for each panel).

The three experimental results along the centre line are compared against the CFD simulation in Fig. 4.14. The profile from the 1D.a velocity distribution, as shown in the figure, is nearly identical to both numerical estimation and target for the majority of the height. The higher region shows a small deviation from the prediction, which may be the result of interactions between the distortion screen and the upper boundary layer.

The 1D.b distribution results, on the other hand, behave the opposite way: while there is generally good agreement amongst the three profiles (target, numerical and experimental), the lower region recorded in the tunnel exhibits an excess of velocity in comparison to the target. Since the CFD shows an increase in velocity with a similar slope to that of the experiments in that zone, this behaviour appears to be somewhat caught by it.

Despite the small portions at the top and bottom of the section in the last case (bi-dimensional distribution), the velocity profile is nearly equal to the numerical simulation and the target. Those regions, however, cannot be replicated because they do not reproduce realistic physical conditions due to the boundary layer presence, as was already noted.

Additionally, two Kiel probes farther downstream of the duct were utilised with the reference 1D.a geometry to evaluate the assumption of distortion conservation.

The distance between the additional probes and the distortion screen is 4.8 and 6.3 hydraulic diameters, respectively, corresponding to the DMS1 and DMS2 sections. The results of these downstream measurements are displayed in Fig. 4.15, showing how the target velocity distribution is successfully maintained throughout the test section of the wind tunnel.

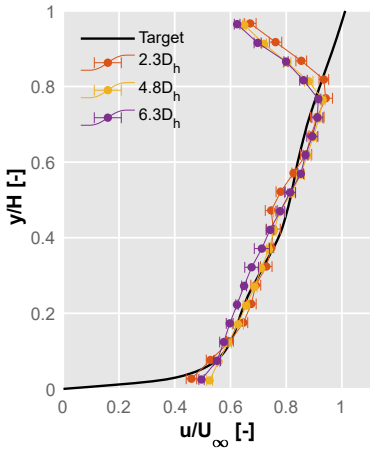

Figure 4.15: Evolution of the velocity profile for the 1D.a case at different hydraulic diameters D_h downstream of the panel. Error bars show standard deviation.

Finally, Fig. 4.16 shows the data from the measurements made in the cross-section for each of the cases. The zones very close to the top and bottom, as well as those that are closest to the lateral walls, cannot be accessed by the probe due to physical restrictions. In general, it may be claimed that the distributions and the objectives are fairly similar.

In the 1D.a case, the difference with the objective is approximately 4% over the majority of the section, with bigger deviation values in the bottom-right zone. The accelerated flow of the 1D.b case, already seen in the profile of Fig. 4.14 causes a zone in the lowest half of the distribution, near the centre, where the deviation grows. The rest of the section displays figures that are also in the range of 4%.

Even under challenging circumstances, such as differences of two orders of magnitude between two opposite corners, the 2D distortion screen can satisfactorily reproduce the diagonal pattern, without the obvious exceptions of values other than zero on the walls. The variation from the target values is slightly higher than in the 1D examples, albeit they still hover around 5%.

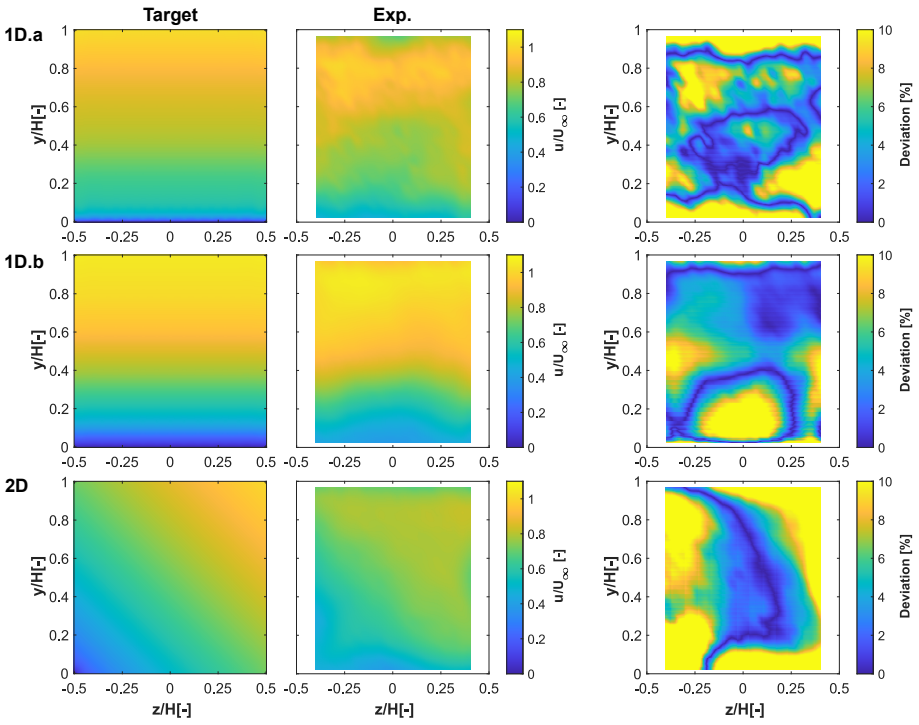

Figure 4.16: Experimental validation of the velocity contours, comparing the values from the experiments against the target for each case.

A more in-depth analysis of the deviation of the actual measurements compared to the target is presented as probability distribution functions (PDF) in Fig. 4.17, showing the percentage difference between the actual and desired velocity distributions.

The curves represent Γ fits for each distribution, whereas the dots show the actual values. It is possible to observe that the 1D.a case, which has a mean value of 5.72% and a skewness of 1.79, exhibits its maximum earlier than any other case. Despite an area of relatively high deviation values on the 1D.b screen, this distribution presents the minimum average deviation with a value of 4.57% (and a skewness of 1.63). Higher deviation values are found in the 2D case, with a mean of 8.04% and a skewness of 1.8.

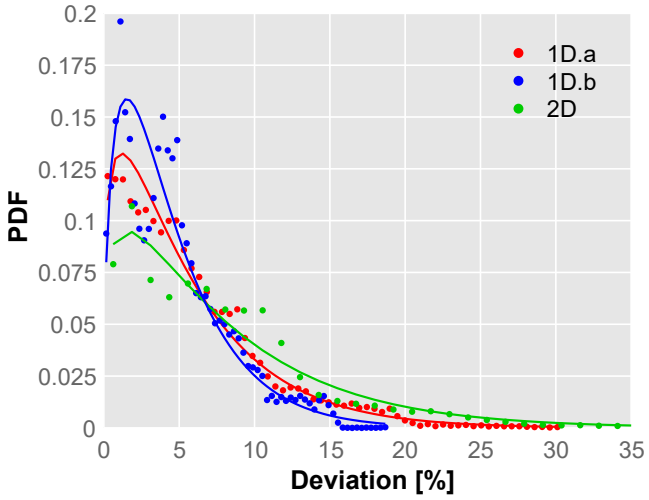

Figure 4.17: Probability Density Function of the deviation in the section comparing the target and the measured distribution for the three different cases. The continuous lines represent Γ distribution fits.

4.4. Summary and conclusions

In this chapter, a technique to recreate target velocity distributions by means of distortion panels has been demonstrated:

- An analytical model that automatically generates distortion screens with variable porosity has been introduced. The values of this variable porosity cause a controlled total pressure drop which generates the velocity distribution.
- Three distinct situations, two 1D velocity distributions and a bi-dimensional field, have been numerically first and then experimentally analysed.
- In the numerical study, a $k-\omega$ SST RANS model has been utilised, providing results quite similar to the targets. It was also observed that the induced velocity distribution was maintained far from the distortion panel and that it generated relatively high amounts of turbulence immediately downstream of the zones with the smallest pores, functioning however as a flow straightener in the remaining portion of the section.

- Additionally, the CFD findings showed that vorticity propagates downstream with large values close to the screen, which supports the requirement to maintain a certain gap between the distortion panel and the measurement section.

- It was demonstrated experimentally that, even under very constrained conditions, the actual distributions obtained in the wind tunnel are consistent with the target ones, with variances typically in the order of 4-5% (below 8% for most of the measured section). Up to 6 hydraulic diameters downstream of the distortion screen, the conservation of the velocity profile has also been probed.

- The model's main flaw is shown when non-physical aspects of velocity are included, such as non-zero velocity too close to walls or abrupt changes in speed over short distances. Furthermore, because the entering flow may include irregularities and a boundary layer close to the walls, actual measurements may deviate from the theoretical targets as the model assumes a constant and uniform incoming velocity. A possible solution may be to develop a new design procedure which includes a loop where the automated design is further improved using the experimental results, creating thus a so-called digital twin.

In summary, it can be said that the suggested technology has the ability to automatically produce a geometry that is simple to manufacture by AM and can accurately reproduce a target velocity distribution in a single run. This will help to shorten the expensive setup periods for wind tunnel aerodynamic tests where this kind of flow distortion is necessary, such as for studies on turbomachinery, engine inlets, internal aerodynamics, civil engineering and architecture, among others.

CHAPTER 5

Experimental characterisation of surface heat exchangers

Thermal management in new turbofan generations will be one of the major challenges to tackle in order to develop promising technologies. For this reason, determining the performances of surface heat exchangers becomes one of the key aspects of the research process.

The methodology proposed in Chapter 3, together with the reproduction of tailored conditions explained in Chapter 4, are implemented in order to experimentally determine the behaviour of different geometries of Surface Air-Cooled Oil Coolers (SACOCs). In particular, the flow distribution resulting downstream of the distortion panel 1D.a is used.

In this chapter, the geometries studied are described firstly, introducing the four heat exchangers. Then, the results obtained during the characterisation are presented and compared against each other. These outcomes are obtained mainly through intrusive measurements. Both their aerodynamic and thermal performances are analysed in order to determine the advantages and limitations inherent to each geometry.

Work on this chapter has been partly published in the following papers:

- Experimental aerothermal characterisation of surface air-cooled oil coolers for turbofan engines [1]
- Experimental and numerical methodology for the aero-thermal analysis of a SACOC heat exchanger [4]
- Numerical and experimental analysis of rounded fins for high speed air-cooled heat exchangers [5]

5.1. Geometries

As previously mentioned, four different geometries are going to be studied: a baseline geometry, which consists basically of a flat plate that serves as a reference; a standard geometry that adds fins with a standard trapezoidal geometry on top of the flat plate to improve the heat transfer; an optimised geometry, which is the result of a topological optimisation process that seeks to reduce the pressure drop induced by the fins; and a rounded geometry which simply incorporates a blended radius to the sharp-edged of the standard geometry.

5.1.1. Baseline geometry

To establish the baseline for the experimental setup with regard to pressure drop and heat transfer, a flat plate heat exchanger geometry has been first examined. This makes it possible to evaluate the performance of the finned SACOCs more clearly against a reference.

The baseline geometry (see Fig. 5.1), on the air side, consists of an AW7075 T651 aluminium [170] flat plate that is 1.5×10^{-2} H thick. It is connected on top of an oil pan constructed of ULTEM 1010, a thermoplastic that can endure high temperatures. The plastic oil pan's main goal is to thermally insulate the oil from both, the ambient and the steel wind tunnel as much as possible. This will allow the heat to be transferred to the airstream exclusively through the aluminium exchanger and prevent conduction losses to the wind tunnel floor.

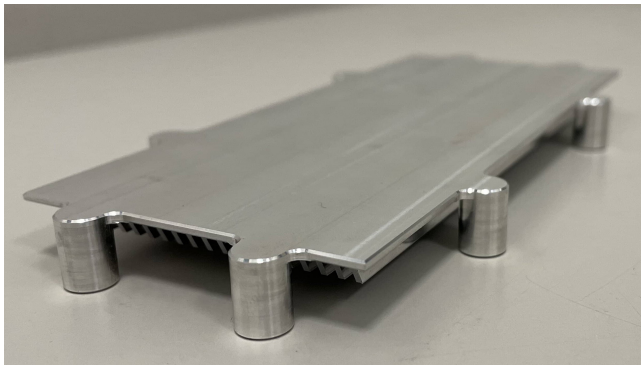

Figure 5.1: Photo of the heat exchanger baseline geometry. The fins of the oil side can be seen underneath

The surface in contact with the oil has a $1.25\,H \times 0.5\,H$ rectangular shape, featuring 18 fins with a standard isosceles trapezoidal shape. They go from the SACOC base to the floor of the oil pan, to ensure a contact surface with the oil as large as possible. The oil circuit is in counterflow, which means that the oil flows beneath the SACOC in the opposite direction to the airstream above, improving heat transmission. There are eight circular stubs to provide a good attachment from the bottom of the oil pan. The rectangular base in contact with the air is only a little bit larger than the surface in contact with the oil to prevent leakages.

5.1.2. Standard geometry

The air side of the design is given a set of isosceles trapezoidal fins in the second iteration. In order to enhance the surface area in contact with the air and improve convective heat exchange [171], it is equipped with a total of 16 fins, each measuring $10^{-2}\,H$ and $0.2\,H$ in width and height, respectively. This form was chosen because it is typical of modern turbofan SACOCs.

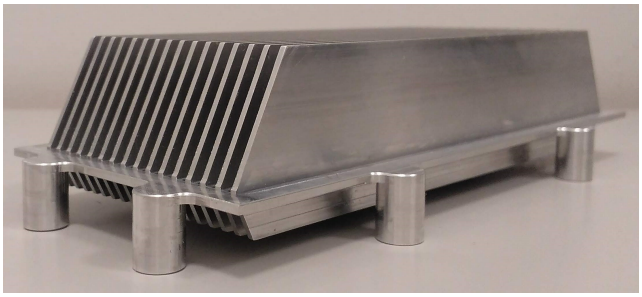

Figure 5.2: Photo of the heat exchanger with standard fins.

With 18 fins and oil flowing in counterflow on the oil side, the configuration is the same as the baseline, ensuring that any differences in the heat exchange are reduced to the interaction of the fins with the air. A picture of this geometry is displayed in Fig. 5.2.

5.1.3. Optimised geometry

In a previous study [38], the geometric design of the fin shape on the XY plane was optimised computationally using a CFD solver. The procedure used the pressure drop per lateral fin surface area $\Delta p/A_{xy}$ as the objective function and monitored the heat exchanged to keep it as constant as feasible.

The optimisation was based on the adjoint method [172, 173]. The criterion of maintaining the heat exchange constant was chosen since this property in aircraft engines is an operability specification, and it is not intended to be changed. The pressure drop, however, is a loss worth lowering.

The adjoint method is a quick way to anticipate how an input design geometry, **D**, will affect a particular engineering cost function, **L**, which, in this case, is based on the pressure drop produced by the SACOC divided by the area of the lateral fins: $\Delta p/A_{xy}$. There are two main steps to the process.

First, on a starting grid with control points $\mathbf{X}^0$, a steady state solution, also known as primal solution, **Q**, is generated. The adjoint problem, based on the prior numerical solution, is assessed in the second stage. The cost function's sensitivity to the various design factors is calculated in the evaluation:

$$\frac{d\mathbf{L}}{d\mathbf{D}} = \left[\frac{\partial \mathbf{L}}{\partial \mathbf{X}} + \frac{\partial \mathbf{L}}{\partial \mathbf{Q}}\frac{\partial \mathbf{Q}}{\partial \mathbf{X}}\right]\frac{d\mathbf{X}}{d\mathbf{D}} \tag{5.1.1}$$

where $\frac{d\mathbf{X}}{d\mathbf{D}}$ is the Jacobian matrix. As a result, the points of the geometry grid where the sensitivity is higher are recognised.

This sensitivity map's gradient shows the direction in which the grid points should be moved through the control points to produce an optimum cost function. A detailed sample of the computational outcomes of this optimisation procedure can be found in [38].

In accordance with the previous optimisation stage, the control points are adjusted. As a result, the geometry and mesh are changed, and a new iteration is carried out until an optimum geometry is attained.

The improved geometry's shape, shown in Fig. 5.3, eliminates the fin's sharp corners and smooths its perimeter. The bow's notorious bulb shape, which advances upstream and upward toward the high-pressure point and enhances aerodynamic performance, is also significant.

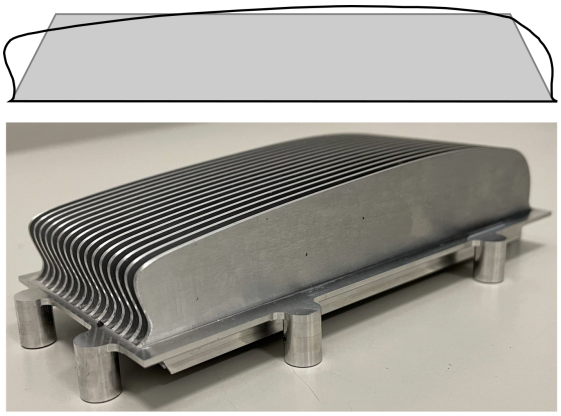

Figure 5.3: On the top, comparison between the lateral shape of the standard and the optimised fins. On the bottom, a photo of the topologically optimised heat exchanger.

A minimum height of 0.12 H at the leading edge tip and a maximum height of 0.22 H at around 68% of the fins' length, the optimised geometry is fairly comparable to the standard fins in height.

The final geometry presents the same number of fins as the standard SACOC on the air side and the geometry beneath them is the same as the baseline.

5.1.4. Rounded geometry

The last version of the geometries consists of a modification of the standard fins that presents sharp edges (the same as in the optimised version) where a blend radius computationally determined is employed to improve the aerodynamics of the heat exchanger.

To do so, a parametric study with a periodic single-fin geometry is employed. A similar approach was employed and reported in the optimisation study [38], since fewer cells than a complete simulation implies hence less computing effort. The five cases considered are collected in Table 5.1.

The temperature distribution imposed at the base of the fin matches the experimental measurement's centre line with the standard finned SACOC. This condition may not be strictly accurate, but it is reasonable for a preliminary study. The fin thickness limits the blend radius to a maximum value ($R_b^{max} = 5 \times 10^{-3}\ H$). As a result, the blend radius range employed for the parametric analysis is from 0 to $5 \times 10^{-3}\ H$.

Table 5.1: Comparison of the variation of the pressure drop Δp and the total heat transfer $\dot{Q}$ with respect the geometry with sharp edges ($R_b/H = 0$)

R_b/H	Δp [%]	$\dot{Q}$ [%]
0	-	-
1×10^{-3}	-11.1	-1.2
2×10^{-3}	-13.9	-1.3
3×10^{-3}	-15.3	-1.7
4×10^{-3}	-16.1	-1.9
5×10^{-3}	-16.5	-2.0

Figure 5.4 illustrates the vorticity contours for four different radii. It displays how the detached area in the leading section of the SACOC is diminished by increasing the blend radius. It seems to cause the velocity between the fins to drop, which has an impact on heat transfer and somewhat lowers thermal efficiency.

The relative fluctuations of the pressure drop Δp and the total heat transfer $\dot{Q}$ compared to the geometry with sharp edges ($R_b/H = 0$) are shown in Table 5.1 at various blend radius values.

Generally speaking, the SACOC benefits from having rounded corners. In comparison to the SACOC with sharp edges, the pressure drop is decreased by 11-16% while heat transfer is only slightly reduced by 1-2%. Both relative variations exhibit a logarithmic decrease, with the variation peaking at the maximum blend radius.

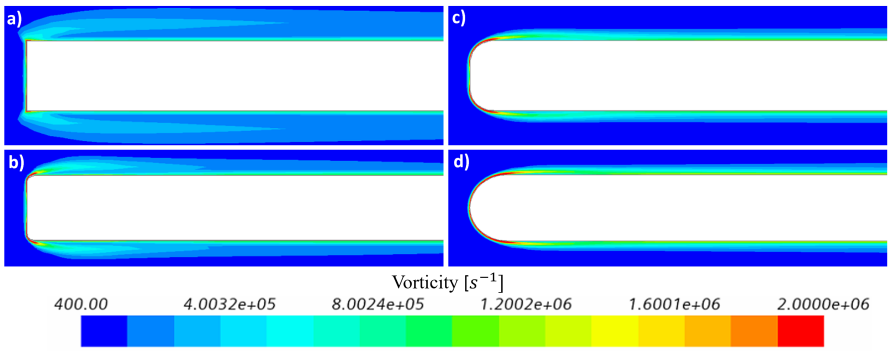

Figure 5.4: Vorticity contour showing the boundary layer detachment for different blend radius (R_b/H: a) 0; b) 1×10^{-3}; c) 3×10^{-3}; d) 5×10^{-3}) at section Y/H =0.1.

The final geometry selected was the one with a blend radius of $R_b/H = 4 \times 10^{-3}$. It has the same geometry on the oil side as the rest of the models. A picture comparing the standard and rounded geometries can be seen in Fig. 5.5.

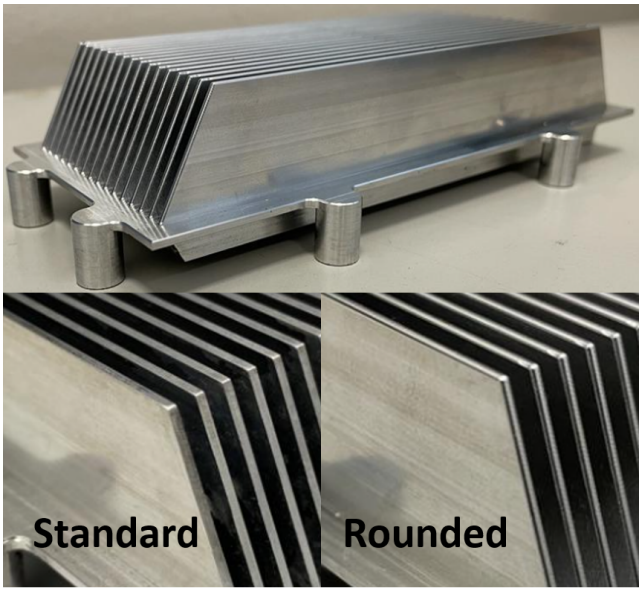

Figure 5.5: Photo of the heat exchanger geometry with rounded fins.

5.2. Aerodynamic results

Despite the primary function of a heat exchanger is to extract as much heat from the hot source as possible, in this application, it is necessary to do so without significantly affecting the aerodynamics on the air side.

This is because the exchanger uses the bypass airflow as a cold sink but this airstream will then be expanded in the secondary nozzle to produce thrust. Thus, this section is focused on the characterisation of the velocity fields and pressure drop induced by the SACOC.

5.2.1. Velocity fields

First, using the conventional isentropic flow relations, velocity is calculated from the Kiel total pressure and temperature data as well as the static pressure captured through the piezometric rings. The analysis of interpolated velocity contours is shown in Fig. 5.6, where each row shows the velocity evolution along the sections for one version and each column reflects the contours in the same section for the various SACOC versions.

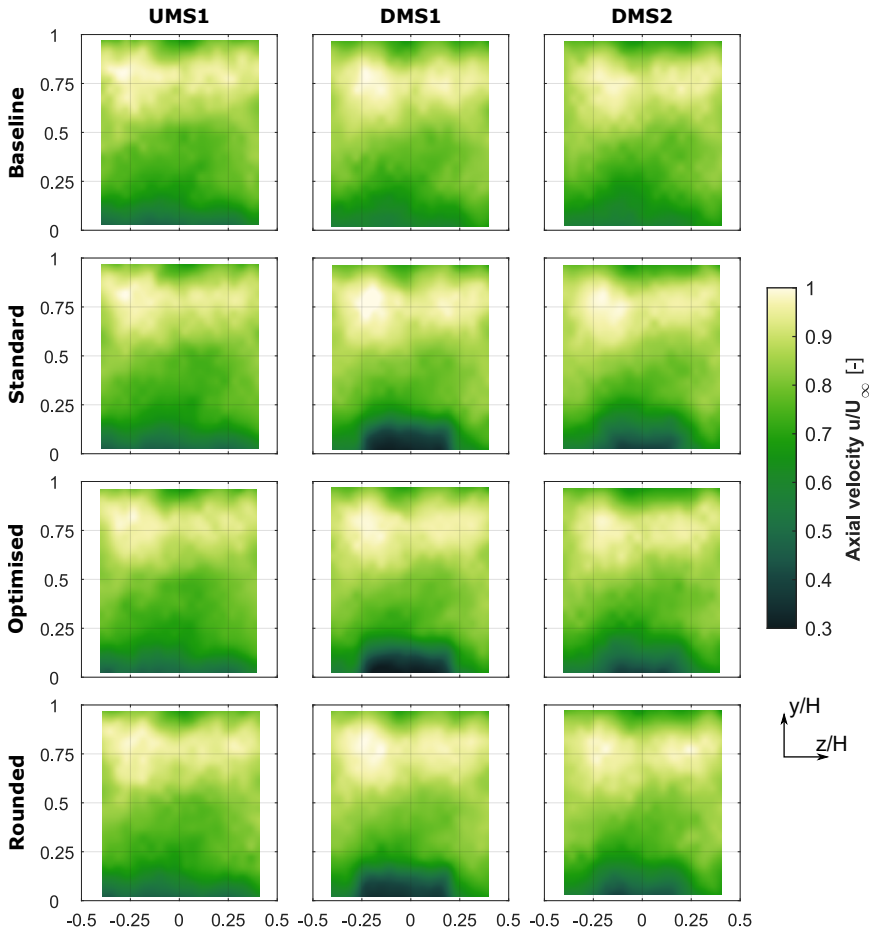

Figure 5.6: Velocity fields comparison for the different SACOC geometries (rows) measured at UMS1, DMS1 and DMS2 (columns) with a typical measurement uncertainty of ±0.06. Note especially the clear "velocity sink" that appears in the wake of the finned versions.

As expected, the gradients in the velocity field at UMS1 follow the intended profile and displays essentially identical contours in the four versions. The results in the three measurement sections are quite comparable when looking at the baseline geometry, which also somewhat reduces the gradients present in UMS1 in the downstream sections.

The three finned versions exhibit comparable behaviours, with the fins having a significant impact on the velocity at DMS1. In all situations, there is a region towards the bottom with particularly low values and an interface where the conditions become freestream-like. In the case of the optimised fins, this zone appears to be smaller than the standard, but the rounded geometry seems to be even less perturbed. The SACOC fins also have an impact on the downstream-most section, DMS2, but here the area of influence is less well defined than it was in DMS1 and, instead, extends towards the lateral walls and accelerates again. The test section's lateral zones, which are not behind the fins, suffer an acceleration compared to their values in the UMS1 up to a height that is similar to what is seen in the wake. Additionally, the gain in speed is greater in DMS1.

In Fig. 5.7, velocity profiles are shown for a more thorough study. These are the velocity averaged values of the four different versions for the SACOC span's centre region, $Z \in (-0.25H, +0.25H)$. This averaging is done to prevent solely showing the impact of the specific fin or channel in the centre.

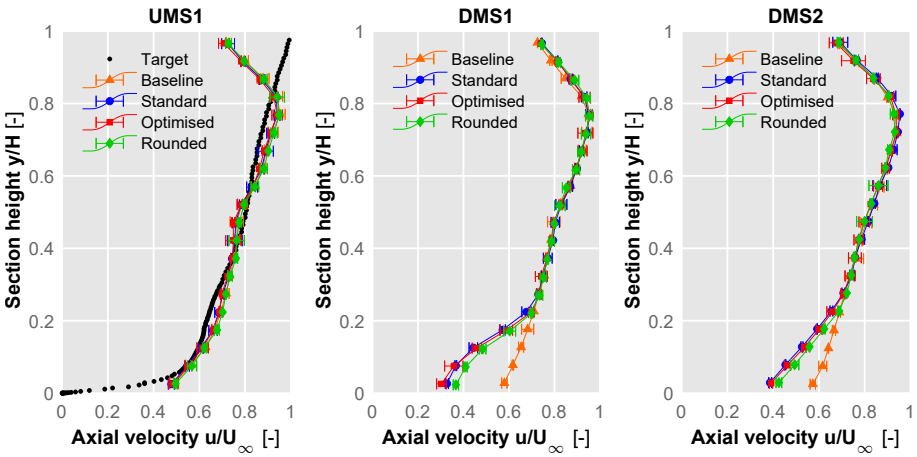

Figure 5.7: Velocity profiles averaged in the central region of the wind tunnel, $Z \in (-0.25H, +0.25H)$, for the different SACOC geometries at each section with a typical measurement uncertainty of ±0.06.

The figure's error bars show the mean values' standard deviation after several measurements. The velocity profiles for the UMS1 are nearly identical and very similar to the target velocity profile sought.

There are very slight changes in the baseline model's velocity profile from one plane to another, thereby maintaining the impact of the distortion screen throughout the tunnel test section.

The finned geometries, on the other hand, exhibit a clear effect on the downstream planes of lower velocities caused by the SACOC wake, being the deceleration clearer in DMS1 (already seen in Fig. 5.6). Here, nevertheless, it is possible to observe that the standard and the optimised versions present almost identical values in the whole height, whereas the rounded version has higher values in the wake than the previous ones. Again, this effect is more noticeable in DMS1.

This can be explained by the fact that rounding the edges of the fins reduces the aerodynamic impact on their leading edge. This allows the flow to remain attached to the surface, not blocking the channel between consecutive fins, and, thus, reducing the aerodynamic impact. It is possible to observe this difference in detached flow in Fig. 5.4.

Another point worth mentioning is that the four versions, despite having different velocities in the wake, present identical values above a height of around 25-30% of the section in the downstream regions. This implies that the fins' influence is confined to an area that is just very little above them.

It can be seen that a boundary layer is generated on the top wall of the tunnel above a height of 75% of H (which is absent in the bypass at this height), but it does not interact with the area affected by the SACOC. This supports the idea of a wind tunnel with a limited height can provide relevant results as long as the top is far enough from the fins.

Overall, velocity results have been measured at UMS1, DMS1, and DMS2 planes using Kiel probes. The results indicate that the targeted velocity profile is well reproduced in the upstream plane and the freestream of the downstream planes maintains the velocity gradient. Besides, the wake produced by the fins is confined to a region very similar in height and width to the SACOC. This implies that performing this type of measurement in scaled-down wind tunnels is reliable since the effects of the walls do not impact the performance of the heat exchanger.

5.2.2. Pressure drop

With regard to the pressure drop caused by the exchanger on the air side, Fig. 5.8 depicts the pressure drop for each version under various operating conditions between both piezometric rings. In the case of an incompressible flow, the pressure decrease can be expressed as follows [149]:

$$\Delta p = K \frac{1}{2} \rho V^2 \tag{5.2.1}$$

where ρ is the density, V the velocity magnitude and K is a pressure drop coefficient that only depends on the Reynolds number, but it becomes independent for high enough Re values [174]. By recalling the continuity equation $\dot{m} = \rho A V$, this can be rearranged as:

$$\Delta p = \frac{K}{2A^2} \frac{\dot{m}^2}{\rho} \tag{5.2.2}$$

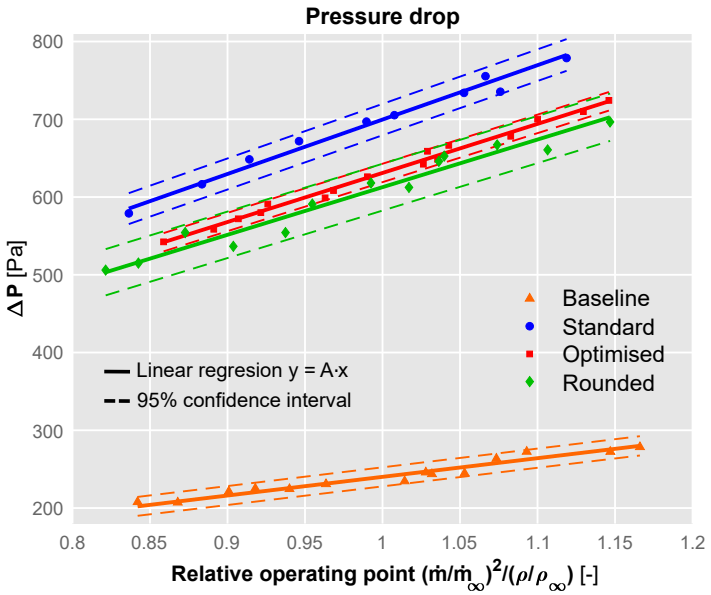

Figure 5.8: Pressure drop variation between piezometric rings with the relative operating point $\dot{m}^2/\rho$ for each geometry with a typical measurement uncertainty of ±1%.

The term $\dot{m}^2/\rho$ should therefore be roughly linear for Δp. This is true for all four configurations at the considered mass flow range, around ±15% of the nominal flow, as shown in Fig. 5.8.

The fundamental benefit of this fact is that it allows for easy computation of losses under various air mass flow settings and ensures that the pressure drop for each configuration is defined by a constant K.

As predicted, the flat plate's pressure drop is significantly smaller than the fins' pressure drop. The pressure drop associated with the optimised version of the fins is lower than that of the standard fins, reaching almost a 10% reduction in pressure drop under nominal conditions, supporting the numerical optimisation technique even though they have very comparable velocity distributions.

This can be explained by the variations in how both geometries interact aerodynamically with the flow, as thoroughly examined in [38]. In comparison to the geometry with conventional fins, the optimised geometry exhibits significantly lower turbulent kinetic energy values in the wake and essentially no vortical structures are created on the tip of the fins.

Nonetheless, the performance of the rounded SACOC is astonishingly good. The mere fact of using a blend radius for the fins' edges reduces the pressure drop in the same order as the topologically optimised shape, presenting even better figures. This fact can be explained by a more aerodynamic shape of the fins, reducing the boundary layer detachment and therefore, letting the air pass through channels between the fins that are virtually larger (a more abrupt detachment would cause blockage of a larger cross-section).

It also explains why the velocity profiles in Fig. 5.7 of the rounded versions exhibit faster values in the wake.

Although the pressure drop is a direct measurement, in general, non-dimensional parameters are preferred to describe and contrast compact heat exchangers [22, 48]. The Fanning friction coefficient f, which correlates the shear stress on the surfaces and the local flow kinetic energy density, is a characteristic variable in terms of pressure drop. This coefficient behaves generally like a Reynolds function, but for large Reynolds numbers (above 100 000), the value stays independent [174]. The Fanning friction coefficient is defined as follows:

$$f = \frac{\Delta p}{2L} \frac{D_h}{V^2 \rho} \tag{5.2.3}$$

being Δp the pressure drop, L the characteristic length which, in this case, is the base length of the fins, D_h the hydraulic diameter of the test section, V the incoming velocity and ρ the density.

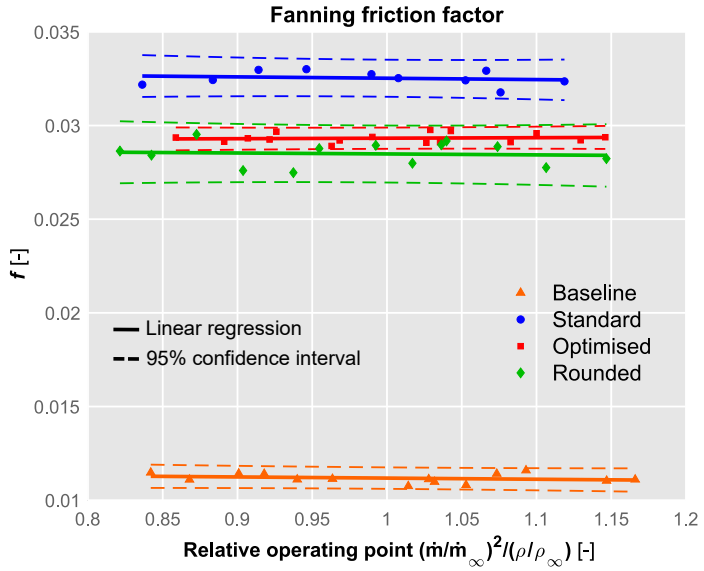

Figure 5.9: Fanning friction coefficient f variation with the relative operating point $\dot{m}^2/\rho$ for each geometry with a typical measurement uncertainty of ±1.1%.

The values of the Fanning friction factors of the four versions are displayed in Fig. 5.9 for the same relative operating range as the pressure drop. On one hand, it is possible to observe that the variations of the Fanning factor in each case can be considered negligible (regarding the linear regression, these are below ±1%), confirming thus that the f value at this high Reynolds numbers remains independent.

On the other hand, the values follow the same trend as in the pressure drop analysis. The Fanning factor f under nominal conditions is 11.83×10^{-3} in the baseline, 32.52×10^{-3} in the standard fins, 29.33×10^{-3} in the optimised ones and 28.48×10^{-3} after rounding the standard fins. These results are collected in Table 5.2.

Table 5.2: Fanning friction coefficient of the different SACOC geometries.

Baseline	Standard	Optimised	Rounded
11.83×10^{-3}	32.52×10^{-3}	29.33×10^{-3}	28.48×10^{-3}

The obvious behaviour of very low values in the baseline case is then followed by the rounded geometry, which has very similar values to the optimised version of the SACOC and finally, the standard finned heat exchanger with sharp edges features the largest value.

In summary, in this section, the pressure drop produced by the four different geometries has been analysed. The pressure drop was measured between the piezometric rings of the test section. Results show that the pressure loss is linear-dependent with the operating point $\dot{m}^2/\rho$, whereas the Fanning friction coefficient f remains independent. Comparing the finned geometries, it is possible to state that a careful design of the fins is crucial to improve the aerodynamic efficiency of the SACOC, since the optimised geometry reduces the pressure drop by 9.8% compared to the standard geometry and the rounded one improves this value with a reduction of 12.4%.

5.3. Thermal results

Despite the fact that the aerodynamic behaviour of this type of heat exchanger is of great importance, the ultimate and main purpose of their usage is to cool down the temperature of the oil. For this reason, a detailed analysis of the temperature fields and heat exchange is crucial.

In general, the thermal specifications of a heat exchanger are fixed for a certain application, i.e., they are employed to release a certain amount of heat from a hot source, so, with this in mind, the idea would be to try to maintain the heat transfer for the different versions and see what are the differences in terms of size (and thus, weight) and pressure drop.

However, another study which can be also representative and fair to compare is to keep the incoming conditions of air and oil mass flows and temperatures and analyse the performance of each version. Hence, even if there are models that exchange more heat, they can be re-designed to, for example, manufacture a smaller version to save weight and reduce impact in the air. This is the considered case.

5.3.1. Temperature fields

Temperatures on both sides of the heat exchanger, air and oil, have been recorded to perform the aerothermal characterisation. The thermocouple installed in the S-duct upstream of the settling chamber (see Fig. 3.3) has been used to measure the reference temperature T_∞.

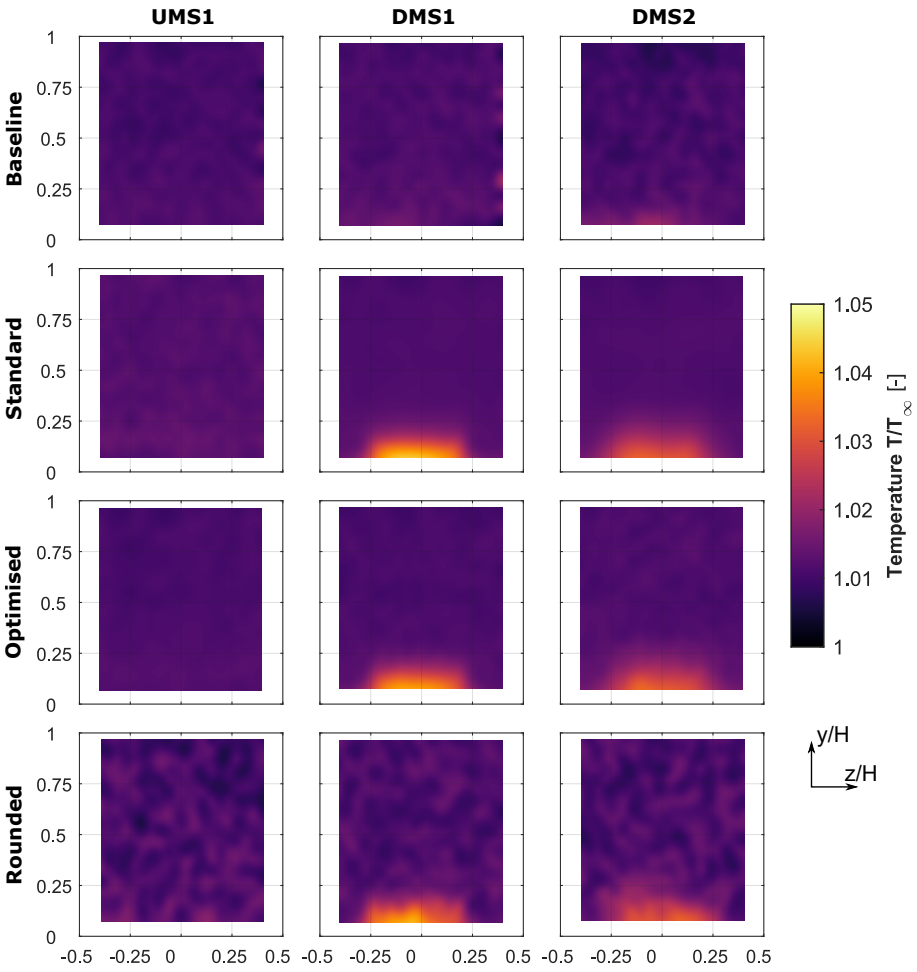

Figure 5.10: Total temperature fields comparison for the different SACOC geometries (rows) measured at UMS1, DMS1 and DMS2 (columns) with a typical measurement uncertainty of ±0.004.

This is done to capture variations in the temperature during the measurements that are not related to the heat exchangers. For instance, due to heating in the compressor that delivers the air, because the runs take enough time to capture temperature variations in the day, or the fact that the ambient temperature can vary from one day to another. It was already depicted in Fig. 3.4 the temperature correction that is performed during long tests.

Figure 5.10 displays temperature contours on the air side obtained from the thermocouples in the Kiel probes. There is a gap in the contours at the bottom because the Kiel thermocouple cannot measure the lower 7.5% of the section (recall Fig. 3.8). The figure demonstrates that the temperature only rises in the vicinity of the fins, up to a 25-30% of the section, a height which is similar to the velocity wake (see Fig. 5.6); above that point, the temperature is nearly constant, but the temperature rises as it gets closer to the bottom in the lower part.

Since the most heated portion of the air goes downstream together with the velocity wake, the influence of the fins is not seen close to the lateral walls either. The thermocouples in the probes are unable to measure the baseline temperature increase since it is weaker and restricted to lower locations that they cannot reach. There is a rise in temperature that follows the finned pattern for the standard, optimised and rounded versions.

The data from the four wake thermocouples are shown in Fig. 5.11 for a more thorough investigation of the temperature along the exchanger wake. Even though all four of them exhibit a similar trend, the finned geometries again exhibit more comparable values than the baseline version.

The temperature reaches its peak at 3-4% of the height and steadily drops to the ambient level between 25% and 30% of the channel height.

Due to heat losses across the wind tunnel, the freestream temperature at the TC1-4 locations can be slightly lower than the reference temperature T_∞. This, together with the experimental uncertainty associated the measurement can result in ratios of T/T_∞ in Fig. 5.11 slightly lower than 1.

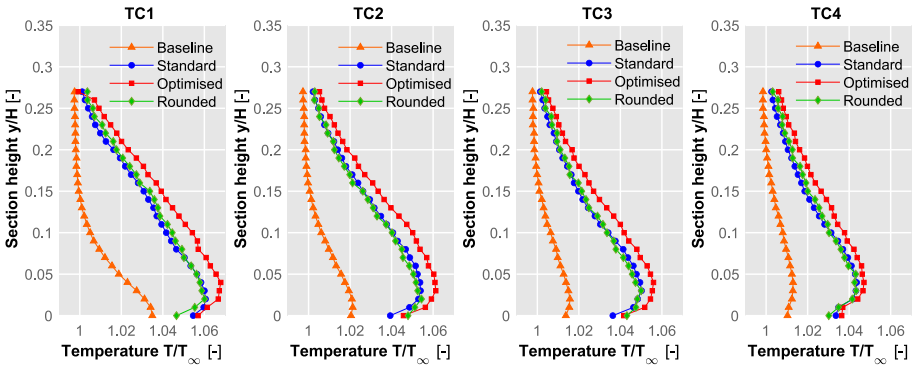

Figure 5.11: Wake temperature profiles for the different geometries as measured by the thermocouple array downstream the SACOC with a typical measurement uncertainty of ±0.005.

As expected, temperatures are higher in regions closer to the heat exchangers and they cool down as they get further downstream. Obviously, the baseline geometry presents lower temperature values, reaching freestream temperature conditions faster. One interesting thing to notice is that the standard and the rounded geometry have identical temperature values in the three measurement locations, whereas the optimised model features slightly higher temperatures, mainly in the regions closer to the SACOC.

This difference in temperature can be explained by the fact that the final geometry obtained during the topological optimisation has a larger surface compared to the standard geometry (specifically, 8.7% more per face). Thus, the air is in contact with a larger hot surface, absorbing more heat.

Overall, temperature results have been presented in the three measurement sections (UMS1, DMS1 and DMS2) and along four different axial positions in the wake downstream of the heat exchanger. The results indicate that the increment in temperature caused by the SACOC remains in the region also affected by the velocity wake, which ratifies the suitability of the methodology for using this type of setup to characterise surface heat exchangers. Furthermore, wake temperatures are larger in the optimised geometry, which indicates that the increase in the fins' surface also causes an increase in air temperature rise.

5.3.2. Heat exchange

Now that the air has been studied, it is time to move on to the oil section and analyse its temperatures and the heat exchanged. It is important to remember that the heat exchanged by the models is determined by carefully examining the oil circuit. Thus, as explained in Section 3.4.2.1, acquiring the oil temperature at the inlet and outlet by means of 8 RTDs (distributed according to Fig. 3.6) and the oil mass flow, assuming constant heat capacity, the heat transfer is defined as:

$$\dot{Q} = \frac{\dot{m}_o C_{p,o}}{4} \left(\sum_{i=1}^{4} T_{\text{in}_i} - \sum_{i=1}^{4} T_{\text{out}_i} \right) \tag{5.3.1}$$

Since the oil pan is made of an insulating material, it is assumed that, as an approximation, all the extracted heat from the oil is delivered to the air.

Under nominal conditions, the mean flow rate of $18.1 \times 10^{-3} \dot{m}_\infty$ on the oil side (where $\dot{m}_\infty$ is the nominal air mass flow), the fluid enters the pan with an average temperature of 1.33 T_∞ and moves in a laminar regime below the SACOC. The fluctuation in these values and air conditions from one version to another is less than 1%.

The temperature of the oil dropped after exiting the heat exchanger by 1.115% for the baseline, 2.936% for the standard fins, 3.234% for the optimised version and 3.296% in the rounded case. Considering the heat exchanged by the baseline to be $\dot{Q}_b$, these results lead to a heat evacuation of 2.711 $\dot{Q}_b$, 2.895 $\dot{Q}_b$ and 3.113 $\dot{Q}_b$ for the standard, optimised and rounded geometries, respectively. These results are displayed in Table 5.3.

Table 5.3: Heat exchanged by the SACOCs referred to the baseline case under nominal conditions.

Baseline	Standard	Optimised	Rounded
$\dot{Q}_b$	2.711 $\dot{Q}_b$	2.895 $\dot{Q}_b$	3.113 $\dot{Q}_b$

Generally speaking, it can be claimed that adding fins is a good idea in these situations because using fins is considered to be justifiable when, by doing so, it roughly doubles the amount of heat removal compared to not using them [171].

Firstly, it is obvious that the finned SACOC with standard geometry extracts considerably more heat from the oil than the baseline flat plate, compensating for the fact that its use increases the pressure drop.

It is also interesting to note that the optimised geometry not only reduces the pressure loss induced by the fins, but that the fact that the fin surface increases aids the heat evacuation, reaching larger values than the standard case.

Nevertheless, the most remarkable behaviour is the one obtained with the rounded geometry. A modification in the design as simple as using a blend radius on the edges of a standard geometry not only enhances the aerodynamic performance, but also improves the heat exchange. It is important however to consider the manufacturing implications that this modification may have.

At first, these results may seem a little counterintuitive, because the temperatures in the wake of the standard and rounded geometries (Fig. 5.11) are identical.

However, considering the aerodynamic results, one should remember that the flow remains more attached to the fin surface, which can aid heat extraction. More importantly though, the velocities of the air within fins are higher, which implies a larger amount of mass flow passing through the heat exchanger (Fig. 5.7). Considering this, if more amount of air is heated to the same temperature, the evacuated heat is larger. This fact evidences the closely coupled aerothermal problem that takes place in surface heat exchangers.

5.3.3. Overall heat transfer coefficient

As explained in Section 3.4.2.2, the overall heat transfer coefficient U is commonly used to determine the thermal performance of a heat exchanger. It can be understood as how permeable the heat exchanger is in terms of heat transfer. It is defined as:

$$\dot{Q} = UA\Delta T_{lm} \tag{5.3.2}$$

The term ΔT_{lm} is the log mean temperature difference, which can be written as follows:

$$\Delta T_{lm} = \frac{\Delta T_2 - \Delta T_1}{\ln(\Delta T_2/\Delta T_1)} \tag{5.3.3}$$

where $\Delta T_1 = T_{o,out} - T_{a,in}$ and $\Delta T_2 = T_{o,in} - T_{a,out}$.

As aforementioned in Section 3.4.2.2, there is no specific requirement for the term A in equation 5.3.2, since there is not a single possible value for U: it is the product which is constant. For this reason, in this case, it will be the baseline surface, as it is shared by the four models and represents the actual surface area that would be occupied on the turbofan bypass. This is justified because the effect of adding fins is already considered in the pressure drop evaluation.

One of the strongest points in favour of using the overall heat transfer coefficient to determine the experimental performance of heat exchangers is that it considers all the experimental conditions that may change from one version to another. Hence, even though these variations in air and oil mass flows and temperatures are lower than 1%, they are taken into account in the computation of the overall heat transfer coefficient.

Table 5.4 collects the values of the overall heat transfer coefficient U for each geometry. The trend observed here is the same as in the heat exchanged, being the baseline case the one with the lowest value of U, followed by the standard geometry and the optimised fins, and the rounded model presents the largest value of the overall heat transfer coefficient.

Table 5.4: Overall heat transfer coefficients for the four geometries under nominal conditions. Values in W/(m^{2}K).

Baseline	Standard	Optimised	Rounded
314.08	896.02	942.88	1073.28

Focusing only on the finned versions, the optimised geometry improves by 5.2% the value obtained with the standard case, and rounding the fins implies an enhancement of 19.78% in terms of overall heat transfer coefficient, confirming thus it is the most efficient to cool down the oil.

5.4. Impact of the incoming velocity distribution

During the experimental characterisation of the heat exchangers, a tailored distortion screen has been used to replicate a specific velocity distribution that aims to reproduce the velocity conditions around the SACOC when it is working in real operating conditions inside the turbofan. More precisely, the velocity profile used in the characterisation is the same as the case 1D.a exposed in Section 4.1.4.

Gelain et al. [45] demonstrated numerically the importance of simulating these devices considering, at least, the vertical velocity profile to capture a correct behaviour. In this section, this influence is analysed experimentally.

Measurements have been made with and without the distortion screen at the same mass flow in order to evaluate the impact of the realistic velocity profile, which is one of the key components of the experimental setup, on the aerothermal performance of the SACOC. To accomplish this, only the geometry with standard fins has been examined.

The central velocity profiles for both scenarios with and without the distortion screen are shown in Fig. 5.12, with the case designated as Clean the one without the panel. The velocity profile in the clean case is relatively uniform in the first plane, and the downstream sections exhibit the wake's influence in a manner that is very similar to that of the distortion screen case.

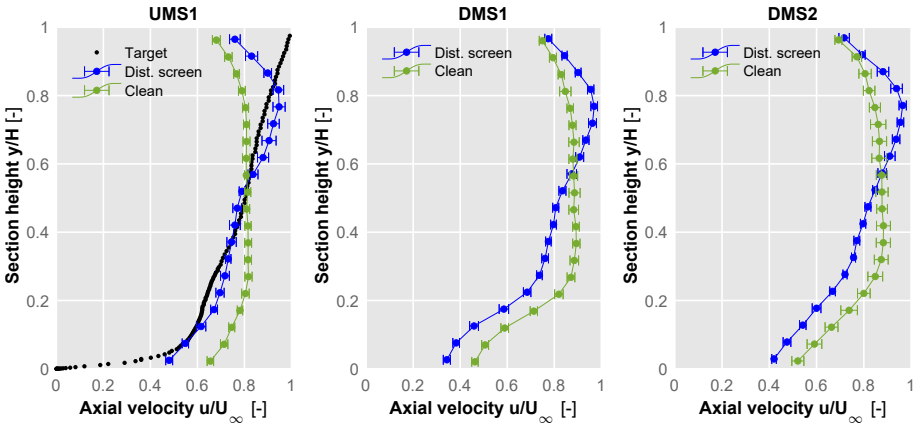

Figure 5.12: Velocity profiles averaged in the centre region of the wind tunnel $Z \in (-0.25H, +0.25H)$ for the geometry with standard fins with and without distortion screen with a typical measurement uncertainty of ±0.06.

It is more clear now the region of influence of the wake, which remains under the 27–30% of the tunnel height. However, because the velocity at UMS1's bottom is higher, the wake also has higher velocity values. Note also how as there is a decrease in velocity in the lower part of the section, the freestream is accelerated in comparison to the upstream section. This effect, although present, is not as easy to see with the distortion screen.

Regarding the pressure drop and the Fanning friction coefficient f, the comparison is rendered in Fig. 5.13. It is possible to observe how the clean case produces a greater pressure drop and the associated f factor is therefore larger.

At nominal conditions, the pressure loss can reach 772 Pa, which implies a considerable increase when compared to the 703 Pa of the case with the distortion screen. The reason behind this effect is that, in the end, the SACOC fins are the elements with the most influence on the pressure loss across the test section.

It is possible to see that the influence of the walls is accounted for in the baseline case, with a pressure drop value of 241 Pa in nominal conditions, whereas the standard geometry (which only differs from the baseline in the fins), induces a loss of 703 Pa.

Considering this, the presence of the velocity profile induced by the distortion screen makes the air flow slower in the fins region, which implies a smoother interaction with the heat exchanger, and thus, lower pressure losses.

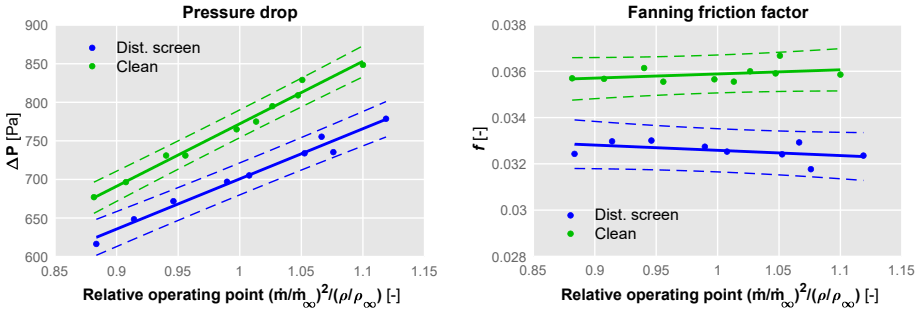

Figure 5.13: Pressure drop (left) and Fanning friction coefficient (right) variations with the relative operating point with and without the distortion screen for the standard fin geometry.

When looking at the Fanning coefficient f, there is a rise of 10.3% from the 32.52×10^{-3} of the standard geometry with the velocity profile to 35.88×10^{-3} in the case of the wind tunnel developed velocity distribution.

Considering the heat exchange, the scenario excluding the distortion panel increases the heat transfer to 3 $\dot{Q}_b$, which represents an increase of 10.74% when compared to the 2.711 $\dot{Q}_b$ obtained with the standard fins and the velocity profile. In this instance, the explanation lies in the fact that, opposite to what happens in the pressure drop, a greater mass flow of air in the area around the fins is advantageous in this case.

Indeed, when the air passes through the fins, not only increases the turbulence by being faster in the clean case (which enhances the heat transfer), but also reduces the residence time in contact with the fins. It means that the air presents colder temperatures and is able to extract more heat from the oil.

As long as tests are carried out in scaled wind tunnels with different velocity distributions to those in real operations, these results confirm the importance of replicating the velocity distribution in the surroundings of heat exchangers to perform representative experimental aerothermal characterisations.

5.5. Summary and conclusions

This chapter has focused on the experimental strategy to characterise surface heat exchangers using scaled wind tunnels for less expensive tests. Three main goals were sought in this chapter:

1. Determine the impact of the geometry of surface heat exchangers on their performance by comparing four different models.
2. Analyse the suitability of performing this type of experimental characterisation for heat exchangers in small-scale wind tunnels and demonstrate an adequate methodology.
3. Confirm the necessity of reproducing the actual velocity distribution to obtain representative values of the heat exchangers.

With respect to the impact of the geometry, four cases have been studied: a baseline, consisting of a flat plate; standard fins, consisting of a sequence of trapezoidal fins; and optimised geometry, produced by topologically optimising the standard fins shape; and rounded fins, in which a blend radius is applied to the edges of the standard fins.

Table 5.5 provides a summary of the findings for pressure drop and heat transfer in the form of the Fanning friction factor and the overall heat transfer coefficient.

Table 5.5: Summary of the aerothermal performances of the four geometries as Fanning friction factor f and overall heat transfer coefficient U.

Geometry	$f \times 10^3$ [-]	U [W/(m^{2}K)]
Baseline	11.18	314.08
Standard	32.52	896.02
Optimised	29.33	942.88
Rounded	28.48	1073.28

Although adding fins to a typical flat plate design increases significantly the amount of heat exchanged, the pressure drop caused in the air side also increases. However, it has been shown that a topologically optimised design, achieved by numerical simulations, can yield a considerable reduction in pressure drop and an increase in heat exchange compared to the conventional fins.

This effect is even more notorious in the model with rounded fins. In fact, the two last cases improve the heat transfer more than the worsen in pressure loss when compared to the baseline, something that does not happen with the standard geometry.

Regarding the finned heat exchangers, the f factor has been reduced by 9.8% when optimising the shape of the standard fins, and even the small modification of rounding its edges can improve by 12.42% this factor. Some-

thing similar occurs with the overall heat transfer coefficient, which rises by 5.2% in the optimised model and almost 20% in the rounded one. This puts into manifest the importance of a careful design or selection of the heat exchanger for a particular operation.

Regarding the suitability of these types of measurements, the influence of the fins has been found to be restricted to the bottom 25-30% of the section (where the fins account for 20% of the tunnel height), and the velocities and temperatures above that value are the same as a baseline case with no fins.

Additionally, although the tunnel walls have some effect on the velocity field, it was possible to observe that there was no interaction with the velocity field associated with the SACOCs.

It proves that representative results can be obtained in preliminary investigations when determining the performances of surface heat exchangers using a small-scale wind tunnel approach.

Finally, to analyse the actual SACOC aerothermal performances under real circumstances, it has been proven essential however to reproduce an adequate velocity distribution. It has been established that using a distortion screen to mimic the velocity profile around the exchanger is crucial in order to successfully employ this approach. Variations in the order of 10% were found in terms of pressure drop and heat exchange when examining the standard geometry at nominal mass flow with the distortion screen that replicates the profile 1D.a from Section 4.1.4 and without this distortion screen.

These conclusions can be summarised as follows:

- Four different geometries have been aerothermally characterised.
- The addition of fins increases considerably both, pressure drop and heat transfer. However, a careful design of the fin geometry can improve significantly the heat exchanger's performance.
- The experimental characterisation presented in this chapter is suitable to evaluate the aerothermal performance of heat exchangers since the outcomes from the geometries are not affected by the tunnel walls.
- Reproducing the velocity profile of the actual operating conditions has a strong impact on the surface heat exchanger performance.

In summary, testing heat exchangers on a small-scale wind tunnel is increasingly essential for engine manufacturers. Full engine testing should always be carried out, although they are very costly, time-consuming, and often difficult to exploit. Nevertheless, methodologies such as the one presented in this chapter can be used for the testing of many different geometries and flow conditions in smaller-scaled experimental facilities.

CHAPTER 6

Optical techniques applied to surface heat exchangers

As explained in the previous chapter, it is highly desirable to conduct experiments in scaled wind tunnels that can mimic the flow conditions surrounding the component because full-scale engine testing is very expensive and time-consuming for the experimental characterisation of aero engine components like surface heat exchangers. However, because of the section's smaller size and the characteristic high air velocities of turbofan engines, invasive instrumentation can alter the component's true aerodynamics. As a result, this chapter presents a methodology for characterising a surface heat exchanger made to operate in the turbofan bypass using optical techniques.

In the this chapter, various methods such as PIV, LDA, Schlieren visualisation, LDV and IR thermography will be used to assess the aerodynamic, structural and thermal performance of a heat exchanger, completing a thorough characterisation of the flow field. Data will undergo cross-validation using several measurement methods. Since most of the measurements would provide results already discussed in the previous chapter where four geometries were analysed, only the conventional geometry of standard fins will be used for the major part of this chapter.

Work on this chapter has been partly published in the following papers:

- Rapid aerodynamic characterization of surface heat exchangers for turbofan aeroengines through optical techniques and additive [6]
- Non-intrusive aerothermal characterization of surface heat exchangers for turbofan aeroengines [9]

Additionally, the possibility of performing a rapid aerodynamic characterisation in models built with additive manufacturing is also considered. This could allow determining the expected behaviour of different geometries during preliminary stages of the design.

6.1. Aerodynamic results

As explained in Chapter 5, the analysis of the SACOC aerodynamics is crucial in order to determine the impact the heat exchanger will have on its surroundings. In this case, it is critical as it operates in the bypass duct of turbofans and the air, employed here as a cold sink, is used for propulsive purposes.

Moreover, it has also been discussed the closely coupled problem between the aerodynamics and thermal performance of these types of devices, which highlights the importance of a complete and thorough characterisation.

Aerodynamic results will be extracted in terms of velocity fields by means of PIV (both, bi-dimensional and stereoscopic), LDA and Schlieren visualisation, but also LDV will be used to determine the structural behaviour of the fins.

6.1.1. Velocity field

The optical techniques used to characterise non-intrusively the heat exchanger have been thoroughly described in Section 3.2.2. Aerodynamics have been captured by means of PIV (Fig. 6.1), S-PIV, LDA and Schlieren

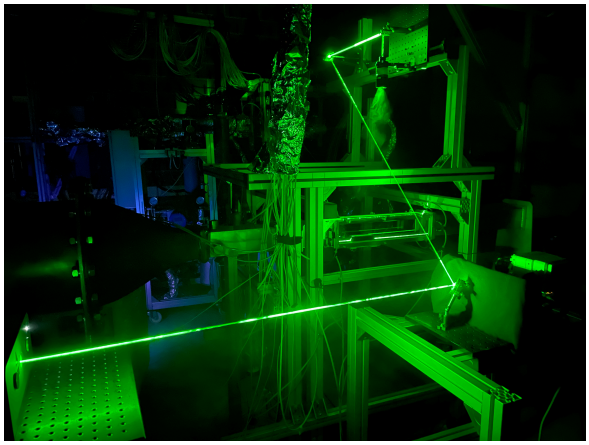

Figure 6.1: Image of the PIV configuration.

visualisation. The procedure for the acquisition of each different technique has also been described in Section 3.3. Again, the maximum velocity of the target profile U_∞ will be used for non-dimensionalisation purposes. This target velocity profile corresponds to case 1D.a described in Section 4.1.4.

6.1.1.1. Cross-validation

In order to assure the veracity of the results obtained, the first step is to perform a cross-validation. To do so, the velocity profiles along the centerlines of the three measurement sections are compared among the different techniques used.

This comparison is displayed in Figure 6.2. Kiel probe-based intrusive measurements have also been included in order to compare the results. The velocities at UMS1 represent the profile targeted during the tests as well as the velocity profiles measured. On one hand, it is possible to see how measurements overlap, which is a good sign of their reliability.

A detailed analysis of the velocity profiles was carried out in Section 5.2.1. It is important to note in Fig. 6.2 how similar all results are in each section, regardless of the method used, which confirms the veracity of the results and can be assumed cross-validated with each other.

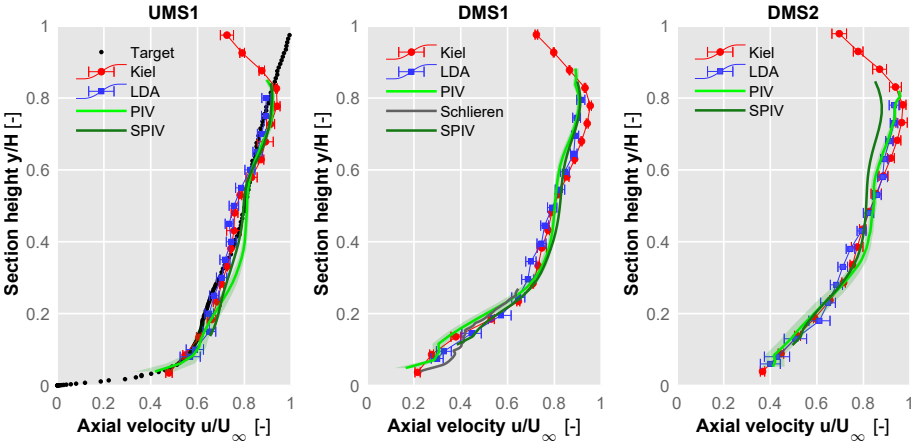

Figure 6.2: Velocity profiles in the centreline of the three measurement planes measured with Kiel probes (intrusive), LDA, and PIV (both, 2D and stereoscopic). In the lower region of DMS1, also the velocities have been extracted from the Schlieren measurements with PIV techniques. Kiel results averaged between $Z \in (-0.25H, +0.25H)$.

The DMS1 is the only plane with data measured with Schlieren visualisation, which is placed at the bottom of the section, since it is the region with the higher temperature contrast, which makes visible the flowfield with this technique. Even the Schlieren technique, which delivers data throughout the entire measurement depth rather than along the centreline, is in very good agreement with the other methods in the wake region. This confirms that this technique may be useful during preliminary stages of an experimental characterisation to analyse the impact of the geometry in the wake.

6.1.1.2. PIV

One of the main advantages of using PIV is its very high spatial resolution and, with a proper set-up, the whole volume of the test section can be analysed. The PIV's default setting illuminates a plane at a specific width (z coordinate). However, the volume can be discretised into a number of planes and the final volumetric result can be interpolated from that data. This is possible if the lens that produces the laser sheet is installed into a traverse system that can move it in a normal direction the laser plane (width-wise).

Figure 6.3 provides an illustration of this methodology. The figure exhibits the interpolated volume, and the first image displays the many planes that have been described in the SACOC's downstream zone. The axial component's velocity field in DMS1 is shown in the final image (although any region of interest within the interpolated volume can be extracted).

The axial velocity fields from the three measurement sections captured with PIV are displayed in Fig. 6.4. Due to the symmetry of the problem, only half width of the test section was examined. There is a lack of data

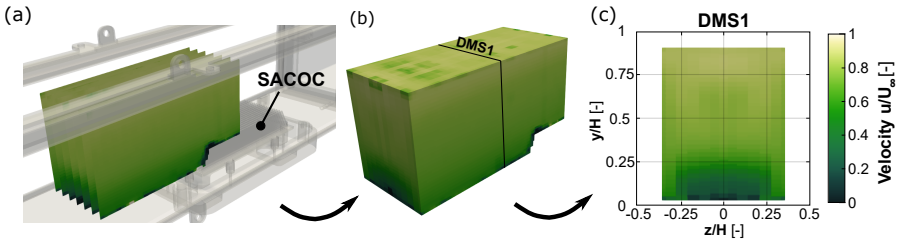

Figure 6.3: Velocity processing of the whole volume using PIV. (a) Experimental characterisation at different longitudinal planes. (b) Interpolation of the data to derive the volume. (c) Extraction of regions of interest.

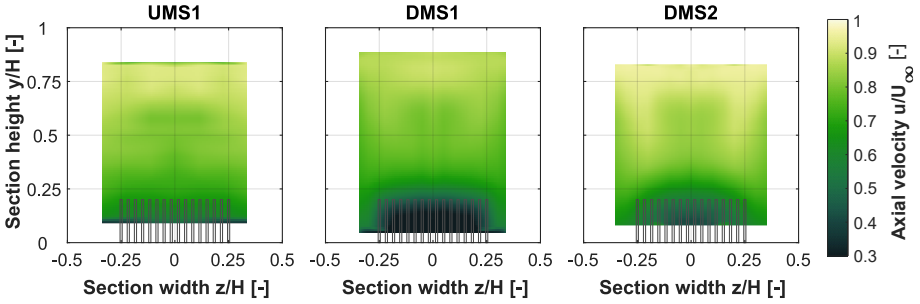

Figure 6.4: Axial velocity distribution in each measurement section measured with PIV.

in the bottom-most region due to reflections, and the lateral- and upper-most zones do not have data neither because the test section frames blocked either the light comeing from the lense or the camera field of view.

6.1.1.3. S-PIV

Although it is possible to derive some of the velocity components in planes perpendicular to the flow direction with PIV by interpolating between different laser sheets (explained in section 6.1.1.2), the most appropriate way to do it is with S-PIV.

The three measurement sections can be deeply characterised with S-PIV, and results are shown in Fig. 6.5. In this case, the data is extracted directly from the postprocessing of the velocity fields captured by both cameras.

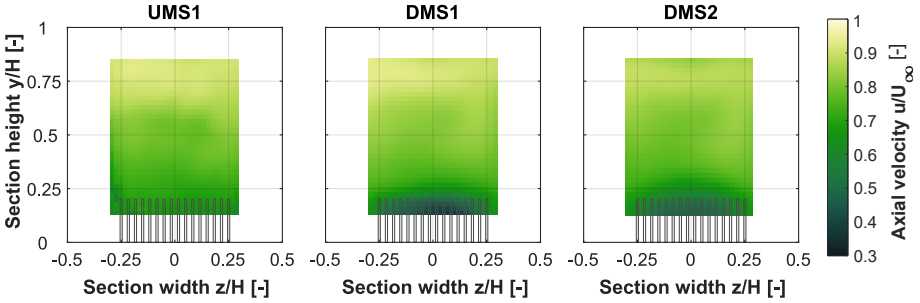

Figure 6.5: Axial velocity distribution in each measurement section measured with S-PIV.

Again, the data is not available in the lower region due to reflections from the tunnel floor and the laterals and top of the sections were blocked for the laser sheet and the cameras field of view.

The most interesting features about this method is the high spatial resolution directly obtained from the measurement, with a complete information of the three-dimensional velocity field in that plane at a fairly high rate (in this case, 1 kHz).

The velocity field measured with the Stereoscopic PIV is shown in Fig. 6.6 in each of the three characterisation sections, showing the three dimensions of the velocity. Although a comparable approach as the standard PIV might be used to characterise the entire test section's volume, the setup is more complicated, hence only the three measurement sections have been examined. To appreciate the in-plane components, the vectors in Fig. 6.6 have been rescaled in the out-of-plane component up to 20% of their real values.

Besides the velocity field in those planes, another figure which is very interesting to analyse and can be extracted from S-PIV measurements of those sections is the standard deviation. The standard deviation from the S-PIV results of the three velocity components in the measurement planes can be examined in Fig 6.7.

The axial velocity standard deviation values in the wake are greater than the other two components, which have values of the same order, as can be seen in Fig 6.7. Also noteworthy is the fact that the lower zone in DMS2 with high values is greater than in DMS1 for the three components. As

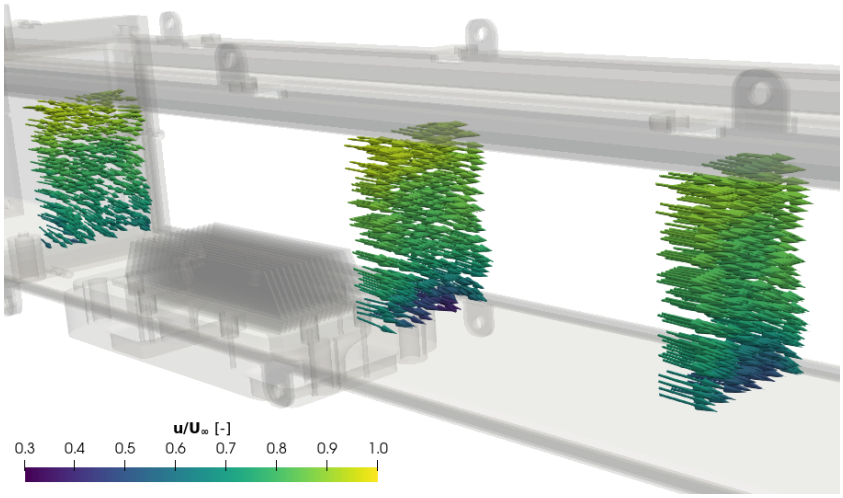

Figure 6.6: Velocity vectors from S-PIV at the three measurement sections.

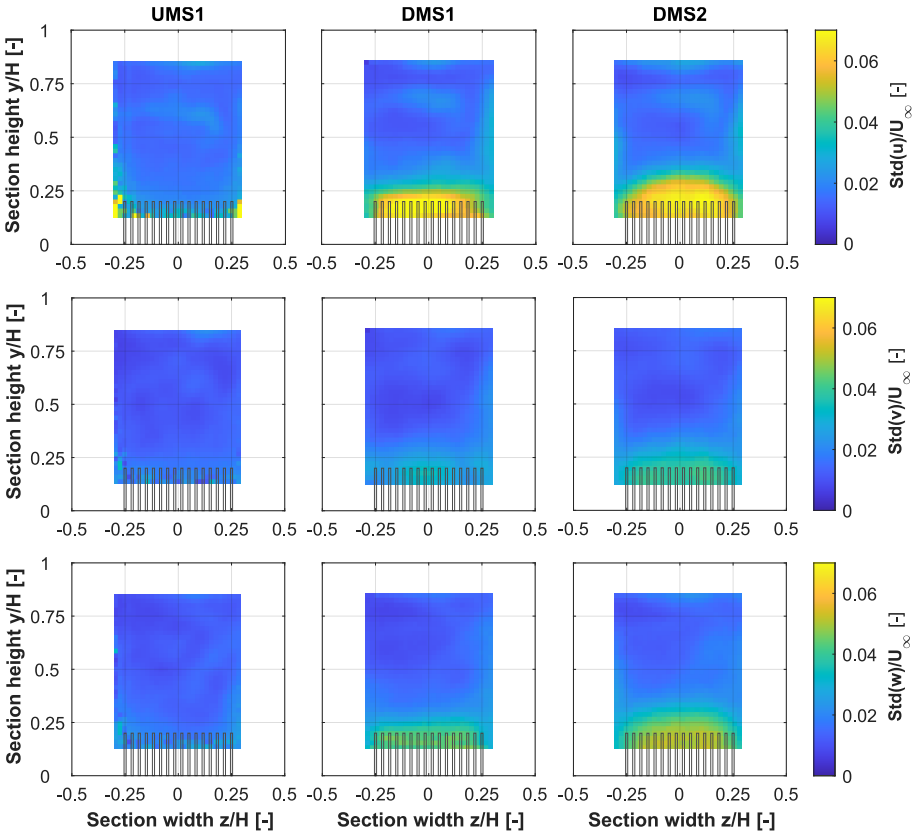

Figure 6.7: Standard deviation of the three-dimensional components (rows) from Stereo-PIV measurements in each plane (columns).

was already established, this is due to wake dispersal and mixing with the freestream, which results in lower (but comparable) values, but across a wider area. In the freestream, figures remain more or less constant across the sections, ranging from 0.02 to 0.03, approximately.

6.1.1.4. LDA

The axial velocity of in the measurement planes captured with LDA can be observed in Fig. 6.8. These results have been interpolated from a grid of points which, similarly as in the PIV case, only captured half of the test section for simplicity. Here, the upper and lower regions were not reachable

because the frames blocked one of the vertical beams, and, close to the lateral walls, the high reflections did not allow the system to capture the flickering.

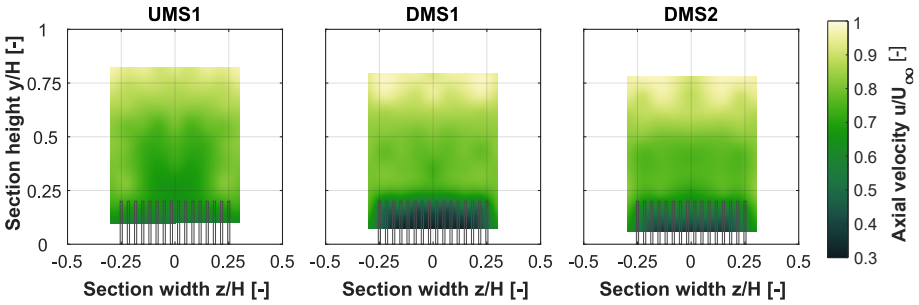

Figure 6.8: Axial velocity distribution in each measurement section measured with LDA.

Since the LDA is mounted in a 3D traverse system, it is possible to discretise not just a particular plane, but a whole volume in the test section and conduct a more thorough investigation of the velocity field. This is a very desireable characteristic of this system, since it allows to analyse any region that may be of interest with a very simple and automatised set-up. The volumetric measurement of the axial velocity using LDA is shown in Fig 6.9. It displays the interpolated axial velocity field as well as the discrete places where the measurements were taken.

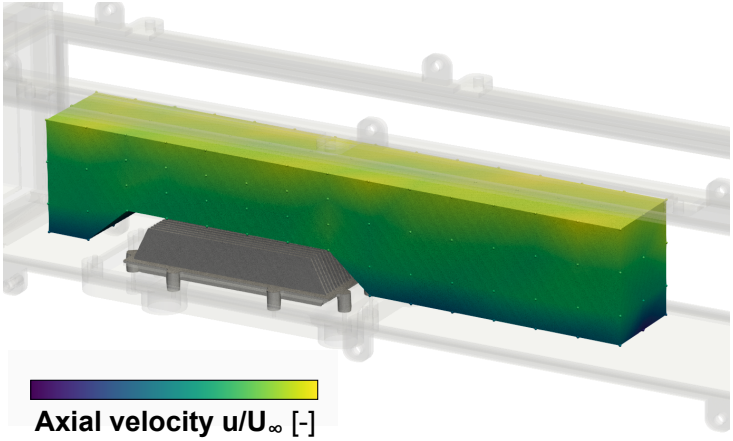

Figure 6.9: Sample volumetric LDA measurement.

Another relevant and very interesting figure that can be extracted from LDA measurements is the TKI. Section 3.4.1.2 explains how to calculate the TKI and its relevance. Although turbulence is closely related to the standard deviation displayed in Fig. 6.7, it is not possible to determine the actual TKI directly from S-PIV results due to the filtering and post-processing that takes place for the velocity field composition.

Recalling the definition of the TKI:

$$TKI = \frac{\sqrt{1/3\,(u'^2 + v'^2 + z'^2)}}{\sqrt{u^2 + v^2 + z^2}} \tag{6.1.1}$$

it is possible to observe that the three velocity components and their fluctuations are needed to properly define it. However, measurements from LDA only provide information of two velocity components. Nevertheless, considering that the flow is mainly uni-directional and that the standard deviation showed in Fig. 6.7 reflected that the variations in the in-plane components are of the same order, it has been assumed that the width-wise component of the velocity and its fluctuations can be considered the same as the vertical ones.

The TKI values of the three measurement planes are shown in Fig. 6.10 under the assumption that the vertical and width-wise turbulent components are identical. Anyway, since axial velocity fluctuations are the primary cause of turbulence, taking into account the third dimension turbulence has a very small impact.

The TKI is in the range of 2% across the majority of the section in UMS1 of Fig. 6.10 and rises to the order of 6-7% at the bottom. This is a consequence of the existence of the distortion screen, which is upstream and heightens the turbulence in the lower part of the section. This is because there is a larger gradient of velocities across the panel generated by the smaller pore region, which increases the turbulence.

This behaviour had been already predicted when analysing the distortion screens in Chapter 4. Fig. 4.12 showed the evolution of the turbulence downstream of the panels and it was possible to observe how the zones downstream of the screen regions with lower porosities presented larger values of turbulence.

In the downstream regions, values of the freestream are maintained close to 2-3%, similar to the standard deviation from the S-PIV. However, the lower zones experience a considerable increase in turbulence due to the wake of the fins, where the values reach figures over 10% in both cases. Once more, there is a slight increment in the area with larger TKI values in the DMS2 when compared to DMS1.

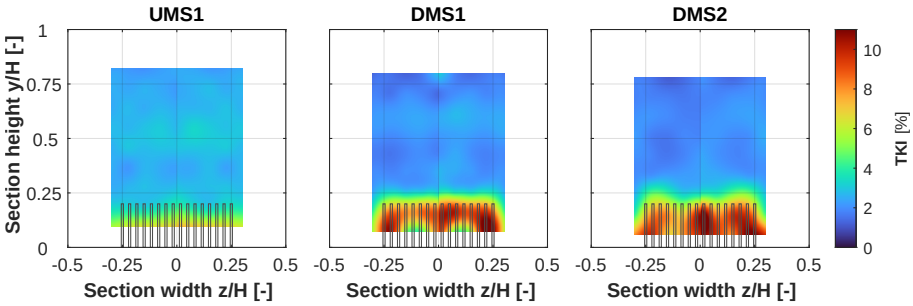

Figure 6.10: Turbulent Kinetic Intensity in each measurement plane derived from LDA measurements

6.1.1.5. Comparison between techniques

Results from PIV, S-PIV and LDA axial velocity measurements are gathered and shown in Fig. 6.11 for comparison. All in all, it is possible to observe the great similarity between them. A deep analysis explaining the behaviour of the velocity field in each one of the planes has already been conducted in Section 5.2.1. Here, it is possible to observe also the gradient in the upstream measurement plane and the region of influence of the fins downstream of the SACOC.

Another region worth analysing and comparing is the wake downstream of the fins of the SACOC. For this, not only the velocity distribution determined by PIV and LDA is available, but also from the Schlieren visualisation. Results are shown in Figure 6.12, with values in all three scenarios being highly similar.

PIV results are shown in the top figure. It is possible to see how the velocity exhibits lower values just downstream and above the fins. This is due to how the freestream interacts with the air that passes through the SACOC's central gap (the area between its fins) and how it is released immediately downstream of it. There are also other regions with very low velocities close to the bottom that may be influenced by reflections of the laser light on the tunnel floor.

In the velocity distribution of the LDA, it is crucial to note that the contours are interpolated from a coarser grid of points. In this case, although the measurement was automatic, since each point is measured individually, the measurement takes longer than in the other two cases and that is why the spatial resolution is lower. However, it is very interesting to note that LDA measurements are still very versatile since they can be performed almost anywhere in the test section.

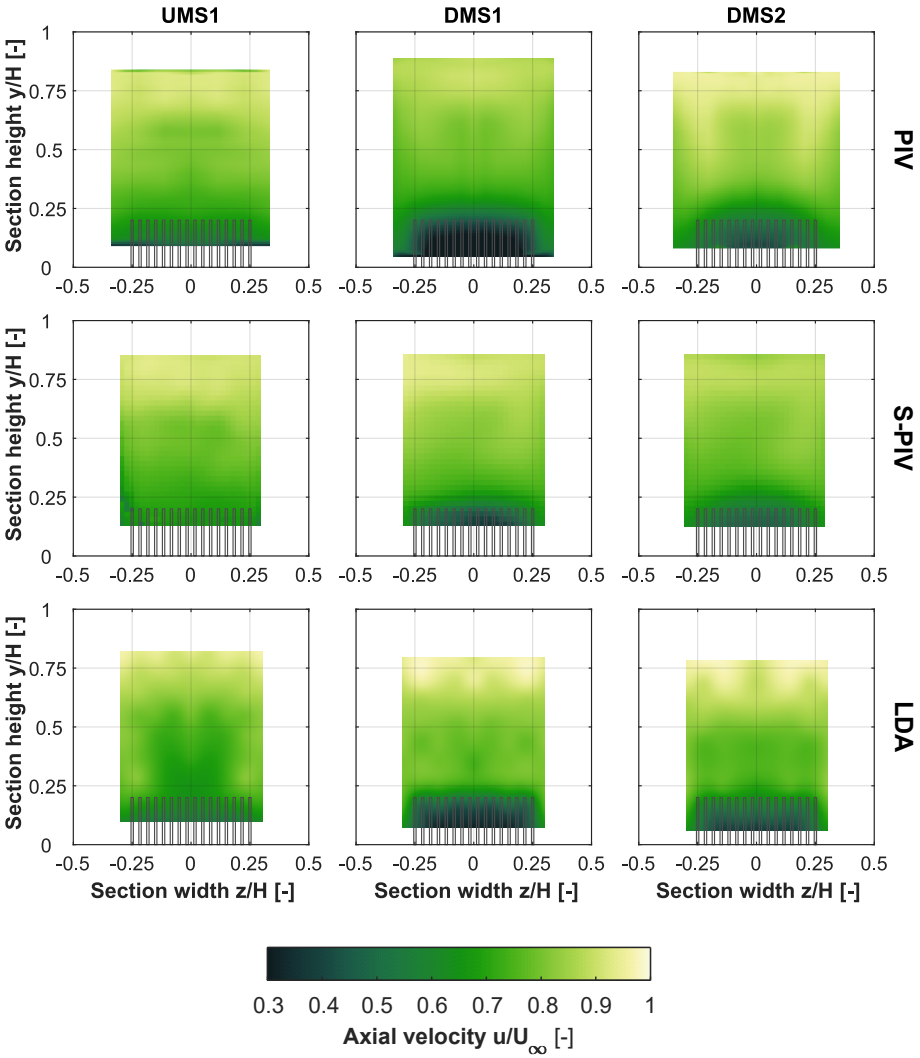

Figure 6.11: Velocity distribution in each plane (columns) measured with PIV, Stereo-PIV, and LDA (rows).

With the Schlieren visualisation measurement, it is important to consider that it gathers the information on the heated air, therefore there is no way to tell which section the velocity data comes from, whereas the PIV and LDA data are taken from the middle plane of the section.

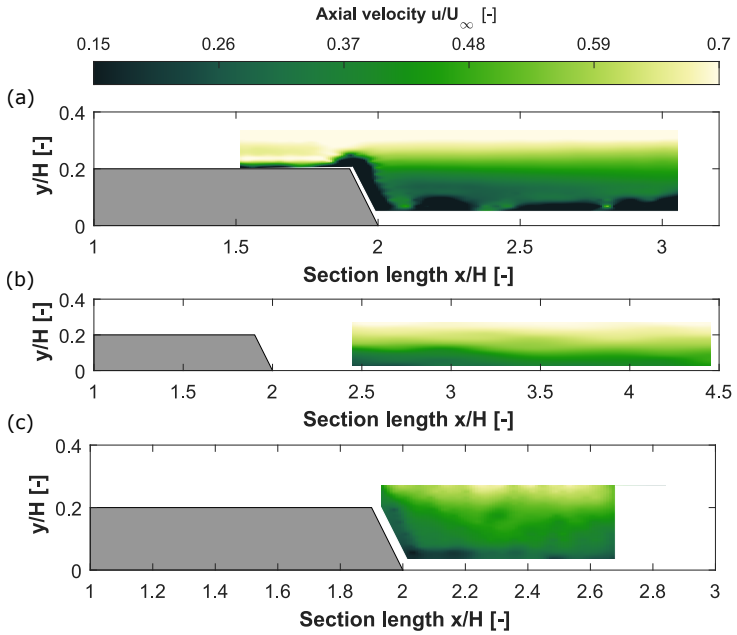

Figure 6.12: Velocities in the SACOC wake: (a) PIV, (b) LDA and (c) Schlieren.

One way to consider the measurement from the Schlieren technique is as if it was the integral mean velocity downstream of the SACOC. Because it captures velocity data from areas where the wake may be interacting with the lateral freestream (between the last fin and the lateral wall), the values of the wake velocity in this scenario are a little higher.

Moreover, one issue with this kind of measurement is that the correlation method could perceive two distinct particles at various depths as the same particle in a measuring plane, leading to inaccurate results. However, these erroneous results can be removed with appropriate postprocessing.

It is obvious that each strategy has benefits and drawbacks. There are certain conclusions that can be extracted from these results:

- Schlieren visualisation is rather simple to execute, but because of the small measurement area and the inability to pinpoint the specific location of the particles in the z direction, it is not very accurate.

- Since in Laser Doppler Anemometry, each measurement corresponds to a single point of the domain, LDA is a time-consuming technique, and in general, fewer data are acquired. Nevertheless, LDA can yield results of velocities at extremely high frequencies, capturing fluctuations to derive the TKI and the setup can be very straightforward.
- PIV provides the opportunity to gather a lot of data from a particular plane, but its implementation is more difficult and expensive, and its time resolution, while occasionally quite high, is inferior to that of LDA. However, a stereoscopic setup allows to extract the three-dimensional velocity field of a plane.
- The ability to characterise the entire volume as well as simply particular areas (such as the aforementioned measurement sections UMS1, DMS1 and DMS2) is a great benefit of these non-intrusive techniques.
- In any case, it is possible to confirm that the results obtained with each technique are in rather qualitatively good agreement with each other.

6.1.2. Fluid-Structure Interaction

Besides the analysis of the velocity field of the surface heat exchanger, it is of high interest to study the interaction the fins can have with the flow. The vibration of a heat exchanger can be negative in most cases, acting as a source of noise, causing fatigue, crack formation or even increasing turbulence and pressure loss. There may be some positive side effects though as well, such as the enhancement in heat exchange capacity caused by an increment of the heat transfer convective coefficient.

Figure 6.13 illustrates the vibration of the outermost fin, together with its modes. The first mode values are used to normalise frequencies and displacements. The Operational Deflection Shapes (ODS) are shown together with the frequency and displacement values associated with them.

Studying the vibrations with LDV has many benefits, one of which is the ability to study the entire surface without adding any mass. In order to perform a similar evaluation using accelerometers, adding mass to the fin could change not only its structural characteristics but also the outcome due to the altered fluid-structure interaction.

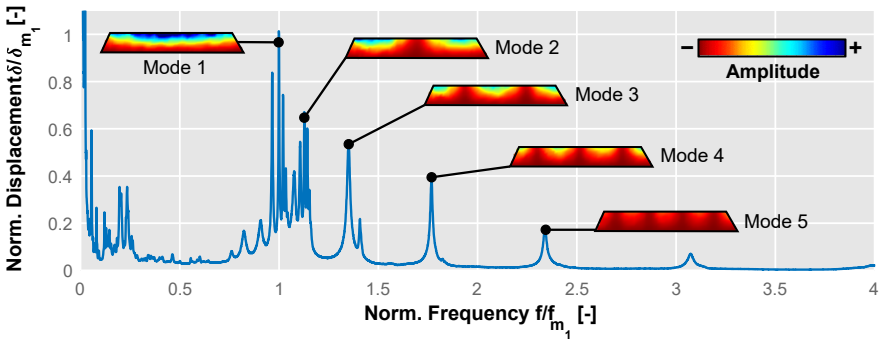

Figure 6.13: Average vibration spectrum of the outermost fin with operational deflection shapes. Amplitudes and frequencies are rendered dimensionless with the first mode values

6.1.2.1. Comparison with numerical simulations

To corroborate the results obtained experimentally, the geometry has been analysed numerically through Finite Elements Methods (FEM) using Ansys Mechanical.

The geometry has been discretised into 153 000 tetrahedral cells. Those parts in contact with the oil pan, i.e., the cylinders used to screw the SACOC to the pan and the lateral faces of the base, have been considered to be fixed. The model has been configured to not be pre-loaded, with a harmonic response and not damped.

The first 100 modes are analysed employing the Block Lanczos algorithm, which uses an automated shift technique to extract the desired number of eigenvalues.

Figure 6.14 represents the comparison of the Operational Deflection Shapes between the experimental measurements and the numerical calculations for the first five experimental modes. Note that these modes do not correspond to the whole heat exchanger ones, which can be obtained numerically, but to those that have been measured on the outermost fin.

In the five cases, the deformation of the outermost fin at the specific frequencies present almost identical behaviours. Table 6.1 displays the numerical and experimental results together with their respective relative errors. Similar to Fig. 6.13, the first five modes are examined, normalising the values with the experimental frequency of the first mode, being $\bar{f}_{Exp}$ the normalised experimental frequency and $\bar{f}_{Num}$ the one obtained numerically.

When taking into account the outcomes in Table 6.1, together with the ODS from Fig. 6.14, it is reasonable to conclude that for the first five modes, the LDV-captured values agree with the theoretical ones with a deviation lower than 2.66%, verifying the results.

6.1.2.2. Comparison between finned heat exchangers

The vibration spectrum of the three finned geometries is displayed in Fig. 6.15. This analysis can provide a better understanding of the aerodynamic performance of these heat exchangers.

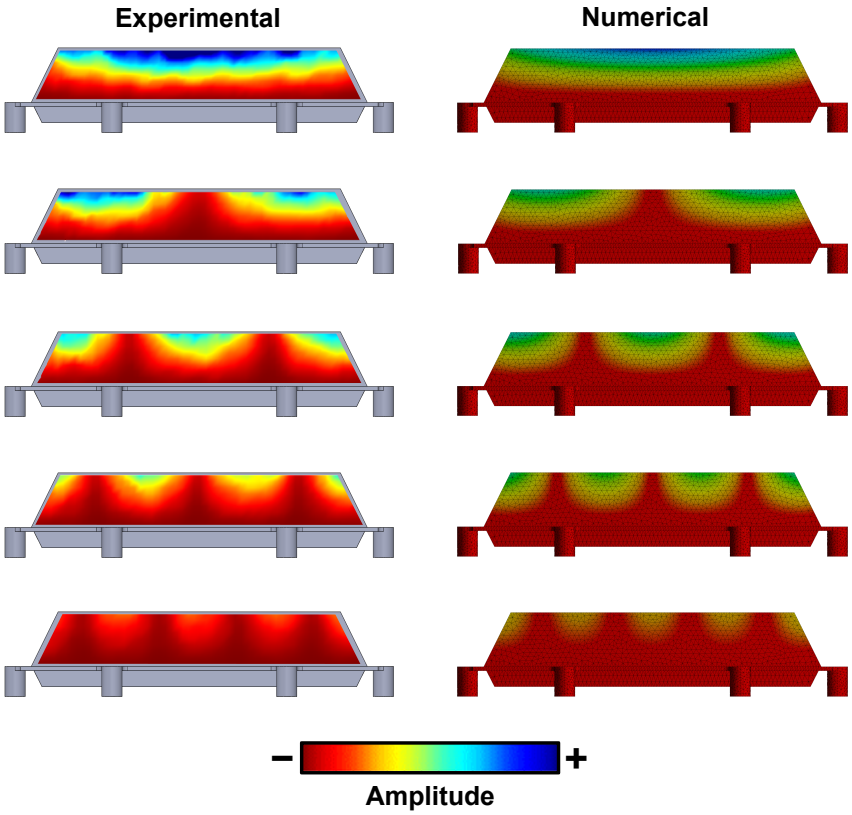

Figure 6.14: Comparison between the experimental and the numerical Operational Deflection Shapes of the first 5 modes in the outermost fin of the standard geometry.

Table 6.1: Comparison of the normalized frequencies of the first 5 modes between the experimental measurements and the theoretical numerical values and their relative error

Mode	$\bar{f}_{Exp}$	$\bar{f}_{Num}$	ε
1	1	0.999	0.1%
2	1.128	1.129	0.09%
3	1.352	1.389	2.66%
4	1.769	1.803	1.89%
5	2.341	2.370	1.22%

It is possible to observe that the fin displacement of the first four modes is considerably larger in the standard geometry than in the other two, which present similar values of displacement. Furthermore, the spectrum of the standard and the rounded geometry feature their modes almost at the same frequencies, since their geometry is practically identical, whereas the optimised geometry presents similar values but slightly different.

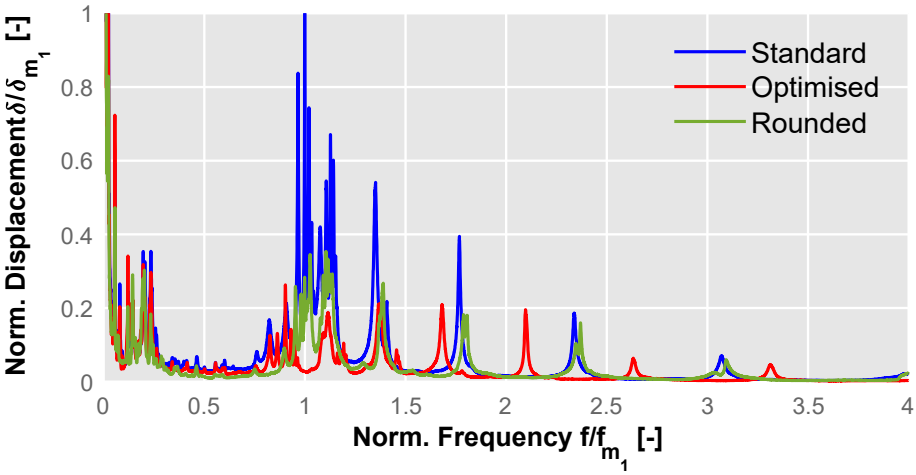

Figure 6.15: Comparison of the vibration spectrum between the different finned geometries. The normalisation values correspond to those of the standard geometry first mode.

The displacement of these first four modes in the optimised and rounded versions are in the same order of magnitude, around 20% – 30% of the first mode displacement in the standard case. However, the displacements of the standard geometry decrease until the same values as the other two are reached at the fifth mode and beyond.

This behaviour of the finned geometries can be related to their induced pressure drop too. The higher values of displacement in the standard geometry could lead to a more turbulent flow, asides from the possible higher energy absorption that also induces a larger flow pressure loss. In the case of the optimised and rounded geometries, the amplitudes throughout the spectrum are very similar, as the values obtained in the pressure drop.

6.1.3. Rapid characterisation using additive manufacturing

In recent years, the usage of additive manufacturing (AM) has become more significant. It is a manufacturing technique that is both quick and reasonably priced, and reproduces extremely complicated geometries with excellent accuracy. Although there are 3D printers that use metal as a model material, they are still not widely accessible due to their cost and lower precision for replicating complex designs. The usage of plastic 3D printers, therefore, looks more appropriate, at the expense of ignoring the heat performance in favour of analysing simply the aerodynamics.

Different AM techniques like Selective Laser Sintering (SLS) and Stereolithography (SLA) exist, but they may not yet be widely accessible due to the lack of professional or industrial machines of these kinds. Fused Deposition Modeling (FDM), the most popular kind of additive manufacturing, involves fused and layer-by-layer deposition of thermoplastic filament using an extruder head whose position is computer-controlled.

The standard geometry has been printed in this instance using a Stratasys F170 professional-grade FDM printer, as for the distortion screen. Acrylonitrile Styrene Acrylate (ASA) has been utilised in manufacturing the prototype. In terms of performance, it is quite comparable to the well-known Acrylonitrile Butadiene Styrene (ABS), however, it has a few advantages including improved UV resistance and generally smoother results.

Table 6.2 collects the mechanical properties of both materials together with the aluminium ones, highlighting the similarity between both plastic materials.

Table 6.2: Comparison between the mechanical properties of Aluminium, ABS and ASA.

Property	Aluminium	ABS	ASA
Modulus of Elasticity [GPa]	71.7	2.23	2.01
Tensile Yield Strength [MPa]	503	31	29
Ultimate Tensile Strength [MPa]	572	32	33
Shear Modulus [GPa]	26.9	2.06	1.87
Shear Strength [MPa]	331	60	60
Density [kg/m^3]	2810	1040	1050

The printer has a minimum layer height limit of 0.13 mm, which is also referred to as the lowest achievable precision. Fig. 6.16 displays a picture of both manufactured models: one made out of aluminium and the other one, 3D printed with ASA.

Nonetheless, it is evident that several features, such as stiffness or surface smoothness, will differ from the aluminium model. Additionally, the final product is not isotropic.

One of the main objectives of this comparison is to ascertain whether finned heat exchangers operating under the exigent conditions of aero-engines can be tested in advance using widely used commercial 3D printing technology or whether the differences with the actual model have a significant impact on the outcomes.

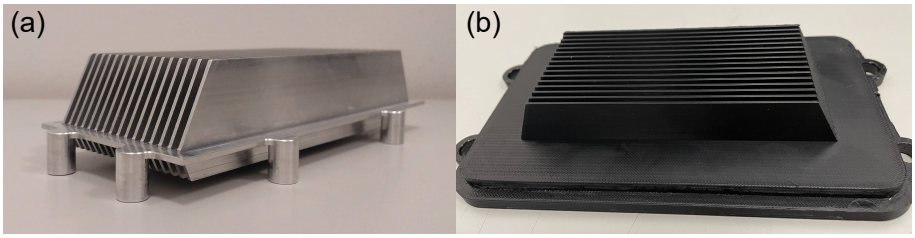

Figure 6.16: Standard SACOCs. On the left, (a) the aluminium model. On the right, (b) the ASA 3D printed model.

6.1.3.1. Velocity fields

It has been shown in Fig. 5.7 that the incoming velocity profile does not depend on the model studied since it does not affect the UMS1 measurements, being the results of the four different models overlapped. For this reason, UMS1 is not studied in this case.

Only the measurements in Planes DMS1 and DMS2 are hence compared in Fig. 6.17. Kiel probes have been utilised for the characterisation of the 3D printed model since Fig. 6.2 demonstrated that results obtained using Kiel probes produced the same values as the optical techniques. LDA results are also present in Fig. 6.17 as a reminder. Regardless of the tested model, it is feasible to show in both cases how the velocity profiles match each other.

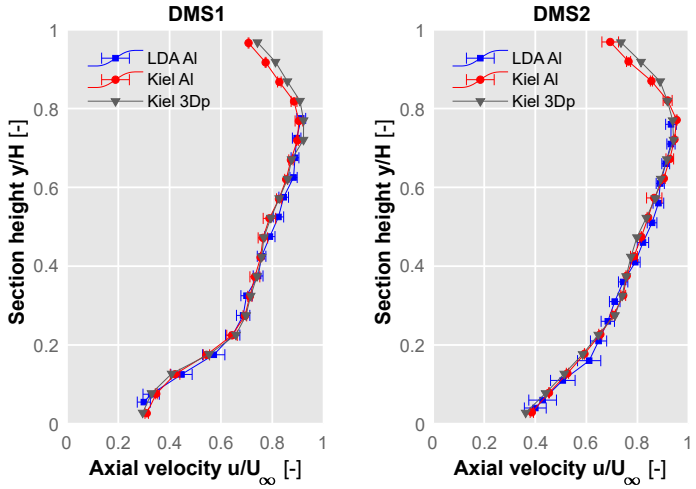

Figure 6.17: Comparison of the velocity profiles in the downstream planes between the aluminium and 3D-printed heat exchanger geometries.

However, the uppermost area has a slight mismatch that results from a tighter arrangement of the upstream glass wall parts during the measurements.

The probe was not inserted through the slit in UMS1 during the evaluation of the 3D-printed model because the characterisation only occurred in the downstream region. As a result, the gap between the glasses that creates this slit was smaller, which decreased air bleed through the first opening and increased velocity downstream. The prototypes' aerodynamic performance is unaffected by this effect though, which is negligible.

6.1.3.2. Pressure drop

The pressure drop that the SACOC causes in the air is yet another important element in the aerodynamic performance of a surface heat exchanger. Fig. 6.18 examines the inlet-outlet air differential pressure of the two models at different air mass flows.

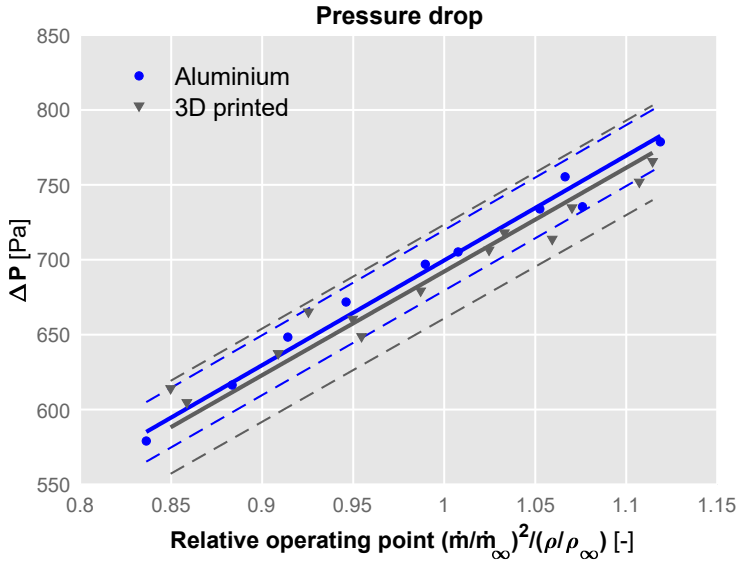

Figure 6.18: Pressure drop induced by the fins of each model. The continuous lines represent a linear fit for the measurements and the dashed lines the 95% confidence interval.

With practically all of the points lying within the combined 95% confidence interval, it is clear to notice that the measurements between the two models are highly similar. The trends are quite comparable and support the linear pattern, with a nominal conditional deviation of less than 1.06%.

As explained in Equation 5.2.2, the pressure drop presents a linear behaviour against the parameter $\dot{m}^2/\rho$ with a parameter K which is Re independent. The value of this parameter is $K_{Al} = 16.26$ for the aluminium model and $K_{3Dp} = 16.09$ for the ASA model, with a respective coefficient of determination, R^2, of $R^2_{Al} = 0.982$ and $R^2_{3Dp} = 0.928$.

6.1.3.3. Fluid-Structure Interaction

In the 3D-printed model, the fins' vibration may also be examined. The ASA heat exchanger is black, as seen in Fig. 6.16, which, added to a non-particularly reflective finishing, implies a low degree of reflection. For this reason, a reflective stripe is glued on the lateral fin during the measurements to enhance the laser signal that reaches the LDV.

When conducting this evaluation, two key factors (both related to the used material) should be taken into account. On one hand, the displacement's amplitude. Since ASA is less stiff than aluminium, a higher displacement should be anticipated. There is no precise method to estimate how large the variance might be, though, because this displacement is brought on by the interaction of the structure and fluid.

This is due to the fact that this type of vibration has a two-way effect: the printed heat exchanger's reduced stiffness makes it more susceptible to larger displacements, but these larger displacements also cause the model to interact more with the flow, which may cause the vibration to induce even larger amplitudes.

On the other hand, the frequency of the material's vibration modes is altered by variations in its structural qualities. Thus, the frequency of the 3D-printed model needs to be adjusted for a fair comparison. When comparing a model a to a model b, the adjusted frequency should therefore be calculated as follows:

$$f_a^* = f_a \sqrt{\frac{(E/\rho)_b}{(E/\rho)_a}} \tag{6.1.2}$$

with E being the material modulus of elasticity. The aluminium SACOC corrected frequency remains unchanged since the properties of the aluminium model have been used as a reference (model b in Eq. 6.1.2), whereas the corrected frequency of the ASA model is higher than the measured frequency.

The average vibration spectrum of both models is shown in Fig. 6.19. The left image depicts the displacements referring to the aluminium first mode, whereas the right figure scales the displacement values of both models with their respective first modes. Both figures feature adjusted frequencies, normalised with the aluminium first mode.

The displacements of the 3D-printed heat exchanger show magnitudes that are nearly ten times bigger than those of the metal model. This is due, as previously indicated, to a two-way interaction with the air as well as variances in the structural qualities of the materials.

However, despite having vibrations that are almost an order of magnitude bigger, the plastic heat exchanger fully replicates the aerodynamic results regarding both, the velocity distributions downstream of the model and the pressure drop caused.

It is also important to note how well the corrected frequency corresponds to the actual aluminium values. The fact that the peaks of the modes overlap at nearly the same frequencies can be seen at the bottom of Fig. 6.19, demonstrating that this method is appropriate during preliminary analysis. The minor discrepancies can be attributed to slight geometric variations brought on by production constraints or the fact that the 3D model, produced via FDM, does not have completely isotropic qualities and has an average density that is somewhat lower than that of the raw fibre utilised.

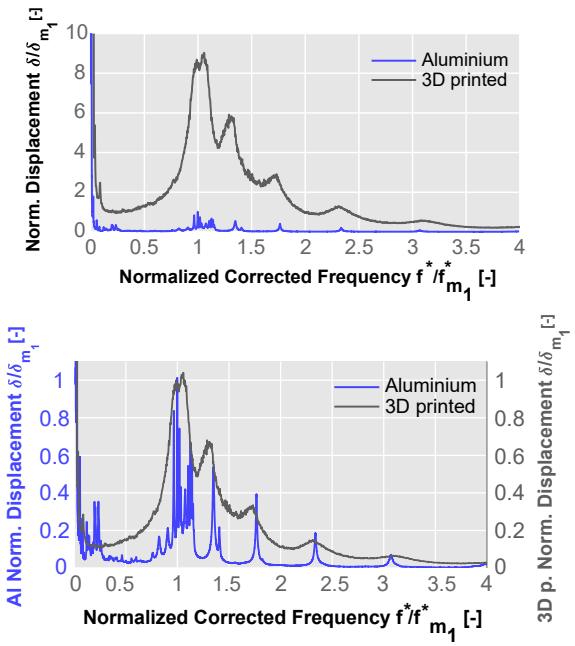

Figure 6.19: Comparison of the vibration spectrum of the aluminium and 3D printed models. Above, amplitudes normalised with the aluminium first mode. Below, each spectrum is normalised with its corresponding first mode amplitude. Frequencies have been corrected with the aluminium structural properties.

6.2. Thermal results

In this section, the thermal analysis of the heat exchanger will be performed. Infrared thermography is used to determine the SACOC temperature distribution to better understand its behaviour. Additionally, a procedure to conduct a thermal analysis in finned heat exchangers is presented, so the Colburn j factor can be extracted from the IR measurements.

Finally, a comparison between the four geometries is presented to complete the aerothermal analysis of the models.

6.2.1. Infrared thermography

The heat exchanger can also be analysed from a thermal point of view non-intrusively. To perform this characterisation, infrared thermography is used. The SACOC is examined from the upper side with a window that allows the long-infrared range between 9 and 14 μm to get through.

Both the tunnel floor and the heat exchanger were painted black using graphite-based paint in order to provide a uniform emissivity. The emissivity was specifically calibrated using a surface thermocouple for these measurements at the corresponding operating conditions.

The Field of View (FoV) of this window does not capture the whole plant of the heat exchanger, so different images are acquired and a final image is reconstructed.

Infrared results are displayed in Fig. 6.20. The temperature distribution is shown on the left-hand side. As might be predicted, the fins' tips have lower values than their bases, which are cooler towards their leading edges because they are farther from the oil inlet and are exposed to colder air.

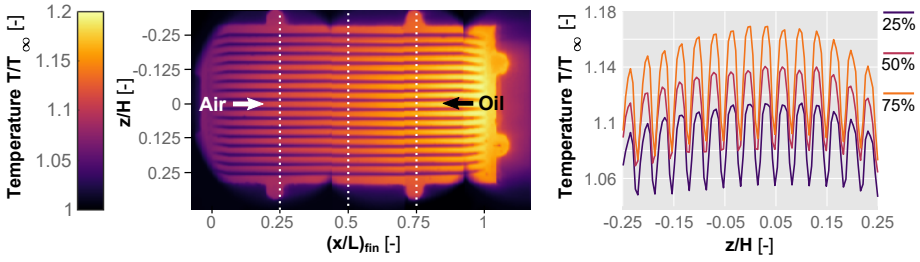

Figure 6.20: On the left, dimensionless temperature distribution on the heat exchanger measured with IR thermography. On the right, temperatures along 25%, 50% and 75% of the fins length.

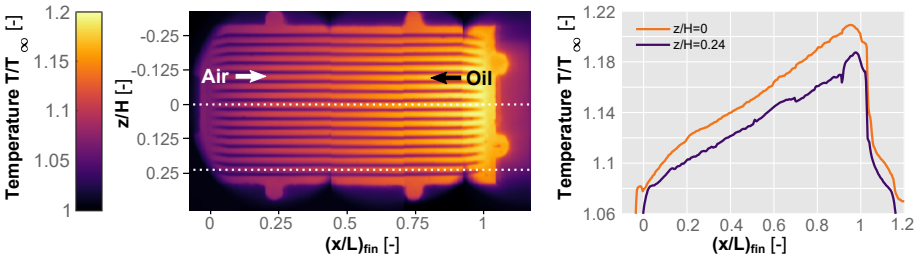

Figure 6.21: On the left, dimensionless temperature distribution on the heat exchanger measured with IR thermography. On the right, temperatures along the longitudinal centre line ($z/H = 0$) and the outermost gap ($z/H = 0.24$).

The temperature evolution along lines perpendicular to the flow direction at three different percentages (25, 50, and 75%) of the fins' length is shown on the right side of Fig. 6.20, making it easier to see the temperature of each fin and emphasising the enhanced cooling of the outer fins.

This effect is more clearly observed in Fig. 6.21. In the figure, the temperature distribution is also shown on the left, highlighting the lines along which the temperature is displayed on the right-hand side of the image.

Temperature's evolution follows a rather similar increasing trend, but the central line always presents larger values. The main explanation here lies with the cooler air close to the lateral fins, which is not heated as intensely as if it was in the centre. Indeed, it is possible to observe that the base at the leading edge of the SACOC has more similar values of temperature, since the air reaching that location is at a uniform temperature in the whole span. Nevertheless, as it advances along the heat exchanger, it gets warmer the closer it is to the centre, so it is less effective in extracting heat and temperatures are larger.

In addition, the larger path the oil has to undergo beneath the heat exchanger needs to be also considered, as both inlet and outlet are centred.

6.2.2. Thermal analysis in finned heat exchangers

One of the advantages of performing infrared measurements of the geometries is the possibility of deriving relevant parameters that are directly related to the thermal performance of surface heat exchangers. In Chapter 5, the heat transfer $\dot{Q}$ and the overall heat transfer coefficient U were used to determine how good each geometry was to transfer heat from the hot source to the cold sink. However, other parameters widely used to analyse

these characteristics of a heat exchanger such as the convective heat transfer coefficient h, the Nusselt number Nu or the Colburn j factor cannot be computed from the data available from that intrusive measurements.

Calculating the heat transfer coefficient is relatively simple for a flat plate with a known temperature, but its calculation is not straightforward when considering a finned heat exchanger. In Section 3.4.2.3, a detailed explanation of how this coefficient can be calculated, accounting for the effects of the fins, is provided.

It is possible to derive the heat transfer coefficient iteratively from equations 3.4.17, 3.4.33 and 3.4.34. Results of heat transfer coefficients for both air and oil can be obtained once the base temperature measured with the IR camera is imposed. Then, the Nusselt number and the Colburn factor are directly obtained by applying their definitions.

The SACOC with standard geometry presents a convective heat transfer coefficient under nominal conditions of 276.1 W/[m^{2}K] which, considering the air conductivity and fin thickness, confirms the assumption previously made that $(ht/k) \leq 0.0625$. The Nusselt number associated with this case is 1269, and the Colburn j factor reaches a value of 21.54×10^{-4}. These values are collected in Table 6.3.

Table 6.3: Convective heat transfer coefficient, Nusselt number and Colburn j factor of the standard geometry.

h [W/(m^{2}K)]	Nu [-]	$j \times 10^4$ [-]
276.1	1269	21.54

6.2.3. Comparison between geometries

The same procedure can be applied to the rest of the geometries. Firstly, Fig. 6.22 displays the temperature distribution in each of the models captured with IR thermography. It is also a composition of four different snapshots that captured different regions of the heat exchanger.

One of the most important outcomes that can be derived from this figure is the difference in temperatures between the baseline and the finned versions. The temperature is not only considerably higher in the baseline case, but it also presents a more uniform distribution than the rest of the models. This can be explained straightforwardly when considering the cooling effect of the fins. Since they enhance the heat exchange, the cooling that occurs in the baseline is much poorer, therefore being the temperature higher.

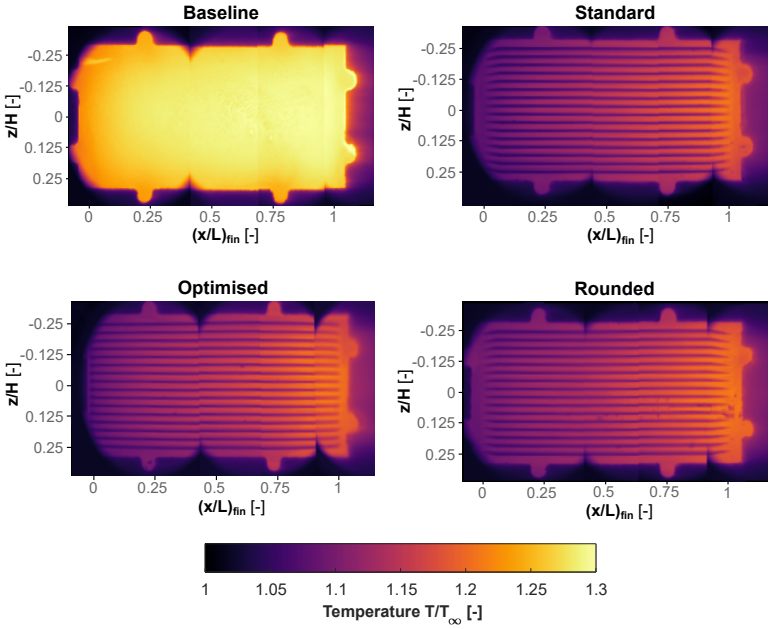

Figure 6.22: Base temperature distribution of the four models. Top-left: baseline. Top-right: standard. Bottom-left: optimised. Bottom-right: rounded.

Additionally, as the aluminium presents a very good conductivity, the temperature is quite uniform. The other cases present somewhat more differences in the flow-wise direction because of the higher interaction of the air with the exchanger due to the fins.

The temperature distribution of the standard, optimised and rounded geometries are quite alike, presenting higher values in the oil inlet, close to $(x/L)_{fin} = 1$, that decrease to the left (air inlet and oil outlet) and along the centre, $z/H = 0$, that diminish to the lateral of the heat exchanger.

Figure 6.23 allows a more quantitative look at the temperature distribution. It shows the temperatures of the models at three different locations: 25%, 50% and 75% of the length of the heat exchanger (along the white lines represented in Fig. 6.20).

It is clearer here that the temperature, for a constant x, presents larger values in the centre that are reduced as they get further towards the sides of the exchanger. This trend is also visible in the baseline. Note that the scale of the baseline figure does not display the same range as the finned versions, nor the resolution is the same. The variations, in this case, are hence slightly exaggerated compared to the other figures.

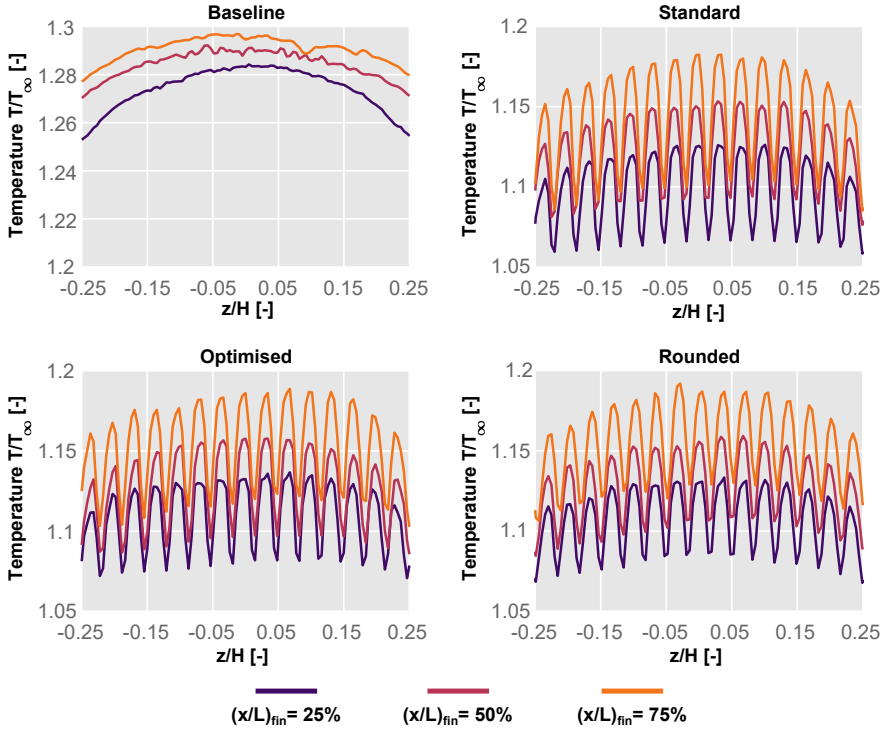

Figure 6.23: Temperature distribution in the direction perpendicular to the flow of the four models at three different axial locations: 25, 50 and 75% of the fin length. Top-left: baseline. Top-right: standard. Bottom-left: optimised. Bottom-right: rounded.

It is also possible to observe the temperature evolution as it gets closer to the oil inlet, presenting the optimised and the rounded geometries temperatures a bit above the standard values.

A closer look at the comparison can be taken in Fig 6.24 that represents, on the left, the temperature evolution of the base along the centreline of the models, $z/H = 0$, and on the right, the base temperature along the line that crosses the outermost gap of the exchangers, $z/H = 0.24$ (see Fig. 6.21 for a clearer explanation of the location).

The baseline heat exchanger, as previously seen, exhibits rather constant values from the leading to the trailing edge, displaying also higher values in the centre than in the lateral. The finned models, as expected, have very similar values in the centreline. However, they exhibit some differences that can be significant.

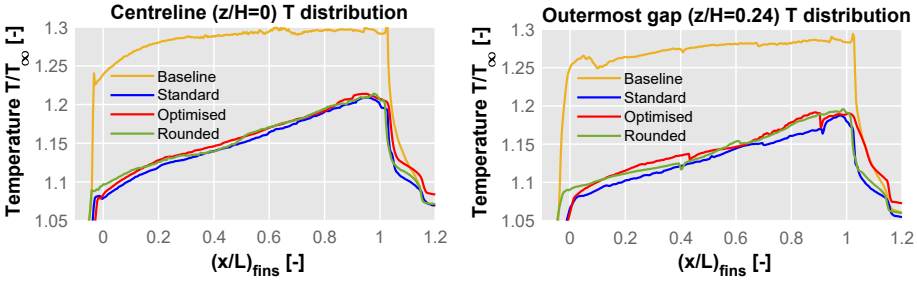

Figure 6.24: Temperature distribution of the base in the flow direction along two lines: on the left, the centreline ($z/H = 0$); on the right, the temperature of the outermost gap ($z/H = 0.24$).

Looking firstly at the centreline, it is possible to say that the three of them exhibit a similar trend where the temperature values increase monotonically. The one that presents lower values of temperature is the standard geometry, followed closely by the optimised one and slightly larger values can be observed in the rounded. This effect is primarily seen in the leading edge.

The explanation behind this behaviour may lie in the aerodynamic interaction between air and fins. The clearest case is the rounded geometry, which presents a more aerodynamic leading edge, enabling the flow to remain relatively attached to the walls.

Nevertheless, the flow hits the leading edge of the other two variants with sharp edges, forcing the increment of turbulence and reducing the temperature in that region.

This effect is less evident as the air advances towards the end of the fins, because the reduction in turbulence in the upstream-most region allows a larger amount of air to go within the fins and extract more heat, compensating hence the difference in the leading edge.

Something similar happens with the optimised geometry, generated to reduce the turbulence and the detachment in the upper zone of the fins. It is therefore more evident in Fig. 6.23 that the cooler peaks of the optimised model (which correspond to the tip temperatures) are hotter than in the standard case due to the reduction of vorticity in that region. This fact can be observed in the work of Chávez-Modena et al. [38] and represented in Fig. 6.25.

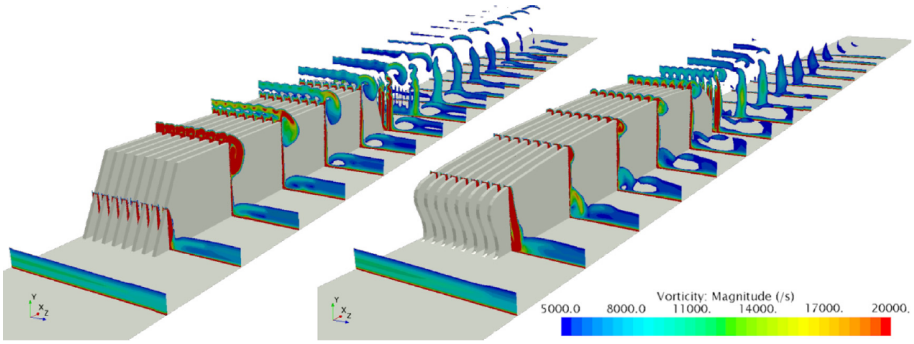

Figure 6.25: Comparison of the vorticity evolution around the fins of the standard and optimised geometries [38]

The graphic that represents the temperature along the outermost gap of the base in Fig. 6.24 can be explained in a similar manner, considering furthermore that the effect of the detachments and turbulence is more significant here than in the centreline.

It is important also to mention that the abrupt irregularities shown in some locations of the plots do not correspond to actual values, but to the fact that some regions were not reached by the IR camera. It is possible to observe these blacked zones in some points of the lateral limits in the temperature distributions of Fig. 6.22.

Regarding finally the derivation of the Colburn j factor, the procedure followed for the rest of the heat exchangers is the same, defining the Nusselt number with equations 3.4.17, 3.4.33 and 3.4.34, solving them iteratively and closing the problem with the base temperature obtained with IR thermography.

The baseline version is obviously straightforwardly derived from Eq. 3.4.16 since no correction for the additional fins has to be made. Results are gathered in Table 6.4.

Table 6.4: Values of the Nusselt number Nu and the Colburn j factor for each geometry.

Geometry	Nu **[-]**	$j \times 10^4$ **[-]**
Baseline	1776	29.43
Standard	1296	21.54
Optimised	1492	24.66
Rounded	1650	27.64

Note that the geometry with the highest values of Nusselt and Colburn factor is the baseline. This is a consequence of the convective heat transfer coefficient. These two numbers only consider the value of the convective coefficient, whereas the reference surface is not taken into account. For this reason, although the heat extracted by the baseline model is much lower than the other three, since its surface is considerably lower (no fins have to be summed to the base), the convective heat transfer coefficient h is slightly larger.

A more significant comparison would be made against equal or very similar areas, something similar to what was done when deriving the overall heat transfer coefficient U. In any case, the finned geometries do present reasonably similar surfaces, so comparisons are more significant.

It is also important to remember that one of the assumptions to compute the effects of the fins in the convection has been to consider that the fins have a constant area along the vertical direction, i.e., the fins have been simplified into rectangles.

For this reason, the total area considered in the three finned cases is the same, although the actual area (mainly in the optimised geometry) could differ a bit.

In general, the results follow a predictable trend with larger values of Nusselt and Colburn j factor for those versions which also exhibit larger values of overall heat transfer coefficient.

Besides the values they feature for the nominal conditions, an interesting analysis would be to determine the Colburn j factor variation with the mass flow. To this end, only the standard and rounded geometries have been considered.

This is because the baseline model, as already seen, is sufficiently different to the finned geometries to provide meaningful information. Only the standard and rounded geometries have been selected for their geometrical similitude and because the simplifications made in the development of the model are more accurate in simple geometries as these two than in the optimised complex geometry.

Figure 6.26 represents the values of the j factor for both standard and rounded geometries under different mass flows. Two main outcomes can be extracted from this analysis.

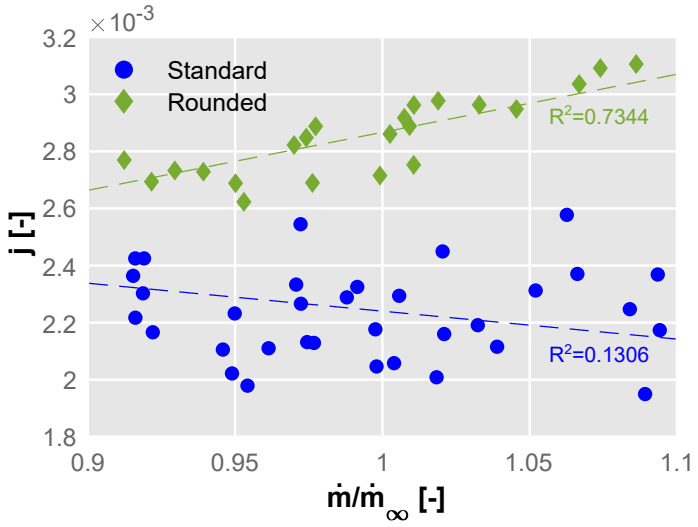

Figure 6.26: Evolution of the Colburn j factor with the mass flow for the standard and rounded versions.

On one hand, the rounded fins have a larger Colburn factor value compared to the fins, and this difference increases with the mass flow. As previously obtained from other measurements, this result can be understood as the rounded geometry being able to extract more heat from the oil than the standard geometry.

On the other hand, the fact that the difference between both versions increases with the mass flow is because the standard geometry seems to be independent of the mass flow. There is a relatively large dispersion between samples for similar mass flow values, and all fall within a similar range. However, the rounded SACOC does exhibit a certain trend with the mass flow, increasing above 15% for the considered mass flow range.

This can be due to the difference in the aerodynamic behaviour between both models. The heat exchanger with sharp edges provokes the flow to separate at the leading edge of the fins, limiting therefore the flow between them and making the SACOC less sensitive to mass flow variations. However, the rounded version facilitates the air to remain attached, reducing the impact at the leading edge and enhancing the heat exchange if more mass flow is available around the fins.

6.3. Summary and conclusions

This chapter presents an experimental investigation using non-intrusive methods on surface air-cooled oil coolers. Overall:

- Although scaled wind tunnels analysis are preferred over full-engine tests during design stages of surface heat exchangers, the use of intrusive measurements can have, however, an impact on the results because testing can entail relatively high Mach numbers in relatively small volumes. A methodology to optically characterise heat exchangers is therefore required.

- To cross-validate the results, various strategies have been used, each with its own benefits and drawbacks. Comparing bi-dimensional and stereoscopic PIV, LDA, and Schlieren visualisation has revealed excellent agreement among themselves, which corroborates the veracity of the results.

- The conclusions reached regarding the validity of using the scaled wind tunnel are the same as in the previous chapter, but the optical techniques have contributed to a deeper analysis, with higher spatial resolution and frequency, the possibility to evaluate the whole volume of the test section rather than only particular planes and new performance indicators such as the TKI.

- Additionally, vibration tests using LDV have been carried out in order to examine the primary frequencies and the morphologies of the fins' deflections. The results obtained are aligned with those measured during the pressure drop analysis.

- Besides, a comparison with a 3D printed model showed that producing prototypes quickly with additive FDM technology is feasible for preliminary testing. The velocity distribution and pressure drop of the plastic and aluminium models were essentially the same. Even the corrected primary frequencies of the ASA prototype capture the behaviour of the real model.

- The thermal characterisation through IR thermography offers more information about the interaction between the heat exchanger and the airflow, providing deeper insight into the phenomena that cause

the heat exchange. With the data that is extracted from these measurements, it has been shown that it is possible to derive the Colburn j factor for finned heat exchangers, which is a relevant parameter in the performance of these types of devices.

In this chapter, the same conclusion derived from the previous one can be confirmed regarding the suitability to perform a correct aerothermal characterisation of high-speed surface heat exchangers in reduced-scale facilities. Besides, using optical techniques has been proven to be highly advisable for their greater spatial and temporal resolution, the fact that they do not alter the flow or the object measured and their higher versatility to measure in different locations.

CHAPTER 7

Conclusions and future works

In previous chapters, a methodology was presented to thoroughly characterise surface air-cooled oil coolers for turbofans experimentally, together with the aerothermal results obtained during operating conditions of these types of heat exchangers. In this final chapter, the global conclusions gathered throughout the thesis document are collected and presented to evidence the main findings of this research.

Besides the main conclusions attained, this chapter also presents possible future works that can complement the results presented in this work and which are of great interest to gaining a deeper insight into the aerothermal performances of heat exchangers.

7.1. Conclusions

The conclusions reached after a complete analysis of surface heat exchangers seek to accomplish the objectives defined in Chapter 1 and extend the existing understanding of SACOCs, their performances and how to analyse them. The main conclusions derived from the research done for this doctoral thesis can be summarised into the following outcomes:

- A novel experimental test bench has been developed which reproduces the flow characteristics experienced by SACOCs located in the bypass duct of aero-engines downstream of fan OGVs. To the author's knowledge, this is the first of its kind and will allow the design of more efficient SACOCs which are expected to play an important role in the next generation of aero-engines.

- Creating representative inlet velocity profiles is key, and a method based on distortion screens has been demonstrated. The screens are manufactured using AM, and the design is automated based on an analytical model.

- Different geometries have been analysed and compared. Metrics such as the Fanning friction coefficient f, the overall heat transfer coefficient U and the Colburn j factor have been used. These key performance indicators have been extracted from intrusive and optical measurements and employed to determine how changes in the SACOC design impact its overall performance.

- Aero-thermal performance was assessed using a range of non-intrusive optical techniques (PIV, LDA, IR, etc.), which have the potential to replace/complement more conventional intrusive measurements. Apart from the obvious advantage of not affecting the flow, optical techniques offer a much higher spatial and temporal resolution and the versatility of performing the measurement at any location.

- A rich dataset from a range of experimental techniques has been generated which can be used for the validation of CFD models. This is of great importance as CFD allows for a very fast evaluation of the performance of this type of heat exchanger which may enable better designs.

These main findings can be broadly categorised into two groups: on one side, the methodology procedures that have been presented, validated, and discussed, and, on the other side, the results derived from applying this methodology to study the performances of turbofan heat exchangers.

7.1.1. Methodology

Throughout the thesis document, different methodologies have been proposed to experimentally characterise the aerothermal performances of surface heat exchangers, proving to be efficient and adequate. The following conclusions and findings have been reached:

- It is possible to automatise the design and manufacturing of distortion screens in order to generate a particular velocity distribution in small-scale wind tunnels. In this regard, it has been proven that for these

types of wind tunnels, it is a fast and affordable approach, very versatile and with highly accurate outcomes. Furthermore, its application has been proven to be necessary to obtain accurate results.

- By applying different measurement techniques, the methodology has been shown to be robust and reliable since the veracity of the results could be cross-validated using different approaches. The proposed techniques provide overlapping and complementary information, which enhances the understanding of the heat exchanger performances and increases confidence in the outcomes obtained.

- When performing experimental characterisations in small-scale wind tunnels at high speeds, optical techniques should always be considered, not only for their versatility, but to ensure that the measurement instruments such as probes, thermocouples, accelerometers, etc. do not impact the actual performances of the studied model.

- The possibility to characterise surface heat exchangers for turbofans in this type of reduced-scale wind tunnel has been demonstrated. As long as there is enough space between the heat exchanger and the surrounding walls, the effects related to the SACOC are confined to a region not much larger than its own size downstream of it. In this case, being the fins height the 20% of the tunnel's, the aerothermal effects were observed below the 30% of the test section height. In the width-wise direction, the effects were in the same order.

- In order to better understand the behaviour of the heat exchangers, it is necessary to analyse several relevant geometries, some of which can serve as a reference to compare the final results obtained. In addition to that, the possibility of rapidly generating geometries using additive manufacturing has also been proved to generate almost identical aerodynamic performances.

- During the development of the thesis document, it was shown the importance of employing relevant and adequate parameters that allow a full comparison between geometries. Sometimes, when performing experimental characterisations, it is not trivial to discriminate and insulate the causes related to observed variations or the models' key performance indicators. Considering this, the proposed procedures facilitate the identification of heat exchangers with better overall performances.

7.1.2. Results

Throughout the chapters of this thesis, different and relevant outcomes have been obtained in the field of thermal management and aerothermal performances of surface heat exchangers. Here, the most relevant are gathered and summarised:

- The distortion screen approach to generate a particular velocity distribution is able to tailor the flow field with high accuracy. It is possible to turn a developed velocity distribution inside a duct into a boundary layer, producing a one-dimensional variation of the velocity, but it also can be used to generate a complete bi-dimensional change of the flow field. A consideration to bear in mind is that distributions with large velocity gradients or with non-physical properties (e.g., non-zero velocity in the walls) cannot be properly reproduced.

- It is important however to consider that the modification in velocity is subjected to turbulence creation so, the lower the porosity of the screen to reduce the velocity, the higher the turbulence induced. In addition to this, some space needs to be left downstream of the distortion panel to let the turbulence created settle and achieve a smooth flow field. Numerical simulations show that one hydraulic diameter is enough, but a more advisable and conservative approach is to leave two hydraulic diameters. In any case, the distortion generated by the screen persists up to, at least, six hydraulic diameters.

- The velocity distribution generated by the distortion screens has also been proven to be highly necessary to obtain reliable results in the aerothermal performances of surface heat exchangers. If SACOCs are studied in a wind tunnel with its standard developed velocity field, the outcomes will differ from those in the actual application. It has been observed that variations in the order of 10% can be found in pressure drop and heat exchange. For this reason, reproducing the actual velocity profile by means, for instance, of a distortion screen appears to be essential to obtain more accurate results.

- The impact of four heat exchangers with different geometries has been analysed: a flat plate (baseline), a heat exchanger with standard trapezoidal fins (standard), one with topologically optimised fins (optimised) and another finned one with the standard geometry but with its edges been rounded (rounded). The addition of fins to the baseline

increases considerably both, pressure drop and heat exchange. However, a careful optimisation of the fins' geometry can yield increases in heat exchange and reductions in pressure losses. Furthermore, considering the very high Reynolds and compressible Mach regime of the operating conditions, rounding the edges of the standard geometry improves even more the heat exchange and gets better results in the pressure drop. It is highly significant because, comparing the rounded geometry outcomes with those from the baseline, the increase in heat exchange is higher than the pressure loss produced by the fins.

- The analysis of the aerothermal performances of surface heat exchangers has highlighted the highly coupled problem that these devices experience. In order to better understand them, different techniques are applied and some of the most relevant coupled results are gathered here:

  - The outermost fin vibration spectrum has shown that the amplitudes of the main modes are closely related to the pressure drop observed in the models. The standard geometry experiences higher values in both cases and the optimised and rounded models have figures which are in the same order in vibration amplitudes and pressure losses.
  - The behaviour of the wake temperatures is closely related to the aerodynamics and fins' surface, as well as to the heat exchange. It is possible to see how the model with the largest fins' surface has relatively larger temperatures in the wake, but how the rounded heat exchanger experiences a higher rate of heat exchange due to less boundary layer detachment in the leading edge.
  - Numerical simulation can also provide very interesting information about the outcomes observed and how they relate to each other, complementing information obtained with infrared thermography on the SACOC temperatures and how changes in vortical structures and boundary layer behaviour among the different models explain changes in the heat exchange or temperature distributions.

- It is additionally proven that, in case some rapid aerodynamic testing of heat exchangers finned geometries is needed, manufacturing the geometry with additive methods provide highly comparable results.

Not only velocity distributions are almost identical, but also the pressure drop induced by the model is of very high similarity. In terms of vibrations, the absolute amplitudes cannot be captured due to a two-way interaction between the fluid and the structure but, by applying a structural correction that considers the difference in the properties of the materials, the main vibration modes and frequencies are reproduced too with high accuracy.

7.2. Industrial impact

It is important to evaluate the potential impact that this research may have at industrial level. When an engine reaches the engine testing stage, the design of the system can be considered frozen since it is practically impossible to change anything due to being very expensive, the possibility of affecting other systems... Even if the design is not as good as it could be, it will not be changed anymore unless it is a show-stopper. Therefore, the most significant impacts are collected here:

- The great advantage of the test bench proposed is that it can capture the real conditions that occur in the engine, and thus be able to design and check the SACOC long before reaching engine testing.
- Currently this characterisation is done mainly by numerical simulations, extrapolating the validation of the models from either relatively low velocities or very simple and not quite representative setups. The proposed methodology will allow a more accurate determination of the aerothermal performance of new designs.
- This methodology, with more accurate results, opens the door to improving the design of SACOCs under real operating conditions, which could lead to significant benefits caused by both, the rise in engine efficiency and the possibility to incorporate new concepts that were not feasible because of thermal management issues.

7.3. Future works

This last section aims to provide some ideas that could be helpful to extend the results obtained in this doctoral thesis, as well as to improve some parts of the methodology or to explore new different approaches. It is divided into experimental-related works and numerical simulations.

7.3.1. Experimental research

The main content of this thesis document is based on how to develop an experimental methodology to assess the aerothermal performances of surface heat exchangers in the most robust manner. However, some extra experimental research can be of great interest:

- This thesis presents a thorough analysis of surface air-cooled oil coolers to be employed in turbofans. It is crucial to study the impact on the air side and, therefore, the doctoral thesis has been focused on this side. However, the role of the oil geometry and how the flow distribution beneath the SACOC can impact the aerothermal performances of these devices is also of tremendous importance. Thus, a study on the effects of the oil geometry such as the number and shape of the fins, adding deflectors perpendicular to the oil flow, turbulence generators, the height of the oil channel... could provide a different perspective of the same device which complements the findings of this investigation.

- The possibility of manufacturing heat exchangers via metallic 3D printing to generate new geometries can also be considered. Although it can have some negative effects on pressure losses (which can also be assessed), it seems a promising approach to designing very complex geometries, mainly on the oil side.

- The cases considered in this research have been evaluated under stationary and nominal conditions. A new interesting analysis would be to determine the aerothermal performances of a model under transient conditions to see how rapidly/easily adapts to new working environments. Furthermore, stationary points different to the nominal condition can also be considered to determine its performances in a wider operating range allowing not only a better understanding of the heat exchanger, but also the possibility of generating a performance map that can be used, for instance, in numerical models.

7.3.2. Numerical simulations

Numerical investigations are very compelling tools to obtain outcomes that could not be assessed otherwise and provide further insights into the physics of the observed phenomena. Some simulation-related works of high interest could be:

- The methodology proposed in this thesis on the automatic generation of distortion screens is an open loop, where a series of theoretical targets are used and a certain geometry is created. Nevertheless, a closed loop can be created after the simulations to refine the geometry. This would create a more complete and robust model that, after a first iteration with the results from the original geometry, the discrepancies between the desired velocity field and the one obtained numerically are used to modify the geometrical parameters of the design.

- A complete Conjugate Heat Transfer (CHT) simulation which considers the interaction between the three main actors in the heat exchange process, i.e., oil, SACOC and air, could provide a lot of useful information about the processes that take place during the exchange. Although some simulations have been used to derive geometries and/or aid in the understanding of the results, a complete simulation can increase the level of detail that explains the observed behaviour.

- A final level of complexity in simulations could be to perform, asides from the aforementioned or combining both proposals, a URANS or even a DES/LES calculation to capture transient phenomena produced by the heat exchanger. Moreover, a high-fidelity FSI analysis can be performed to capture the complete aerothermal performances of a surface heat exchanger.

Bibliography

[1] A. Broatch, P. Olmeda, J. García-Tíscar, A. Felgueroso, et al. "Experimental aerothermal characterization of surface air-cooled oil coolers for turbofan engines". International Journal of Heat and Mass Transfer 190, 2022, p. 122775 (cited in pp. 29, 30, 101).

[2] J. Sánchez-Dehesa, P. Gao, F. Cervera, A. Broatch, J. García-Tíscar, and A. Felgueroso. "Experimental evidence of the Poisson-like effect for flexural waves in thin metallic plates". Applied Physics Letters 120, 9 2022, p. 094102.

[3] A. Broatch, X. Margot, J. García-Tíscar, and A. Felgueroso. "An automatized methodology to generate velocity distortion panels for wind tunnel testing". Journal of Wind Engineering and Industrial Aerodynamics 227, 2022, p. 105065 (cited in p. 77).

[4] M. Chávez-Modena, L. M. González, E. Valero, A. Broatch, J. García-Tíscar, and A. Felgueroso. "Experimental and numerical methodology for the aero-thermal analysis of a SACOC heat exchanger". Applied Thermal Engineering 219, 2023, p. 119409 (cited in p. 101).

[5] A. Broatch, J. García-Tíscar, A. Felgueroso, M. Chávez-Modena, L. González, and E. Valero. "Numerical and experimental analysis of rounded fins for high speed air-cooled heat exchangers". International Journal of Heat and Mass Transfer 201, 2023, p. 123575 (cited in p. 101).

[6] A. Broatch, J. García-Tíscar, P. Quintero, and A. Felgueroso. "Rapid aerodynamic characterization of surface heat exchangers for turbofan aeroengines through optical techniques and additive manufacturing". Submitted to Applied Thermal Engineering, 2023 (cited in p. 127).

[7] M. Chávez-Modena, L. M. González, E. Valero, A. Broatch, J. García-Tíscar, and A. Felgueroso. "Numerical and experimental analysis of thermo- aerodynamic performance in an aero engine surface heat exchanger". In: AIAA Aviation 2021 Forum. 2021 (cited in p. 29).

[8] J. Sánchez-Dehesa, P. Gao, F. Cervera, A. Broatch, J. García-Tíscar, and A. Felgueroso. "Redirection of flexural waves in thin plates". In: Euronoise. 2021.

[9] A. Broatch, J. García-Tíscar, A. Felgueroso, M. Gelain, and A. Couilleaux. "Non-intrusive aerothermal characterization of surface heat exchangers for turbofan aeroengines". In: International Council of the Aeronautical Sciences. 2022 (cited in p. 127).

[10] J. Sánchez-Dehesa, P. Gao, F. Cervera, A. Broatch, J. García-Tíscar, and A. Felgueroso. "Collimation and redirection of flexural waves in thin elastic plates". In: Proceedings of the 24th International Congress on Acoustics. 2022.

[11] Clean Aviation Joint Undertaking. "Strategic Research and Innovation Agenda". Version December 2021 (cited in p. 2).

[12] European Environment Agency, European Union Aviation Safety Agency. "European Aviation Environmental Report 2019". Publications Office of the European Union, 2019 (cited in p. 2).

[13] F. Whittle. "Improvements relating to the propulsion of aircraft and other vehicles". GB347206A, 1932 (cited in p. 3).

[14] Rolls Royce press release. "Rolls-Royce UltraFan technology demonstrator build complete and getting ready to test". Accessed on 24/01/2023 (cited in p. 3).

[15] J. Sousa, L. Villafañe, and G. Paniagua. "Thermal analysis and modeling of surface heat exchangers operating in the transonic regime". Energy 64, 2014, pp. 961–969 (cited in pp. 5, 14).

[16] K. Hart. "Basic Architecture and Sizing of Commercial Aircraft Gas Turbine Oil Feed Systems". In: ASME Turbo Expo 2008: Power for Land, Sea, and Air. Volume 4: Heat Transfer, Parts A and B. 2008, pp. 1431–1441 (cited in pp. 12, 23).

[17] P. Gloeckner and C. Rodway. "The Evolution of Reliability and Efficiency of Aerospace Bearing Systems". Engineering 09 (11), 2017, pp. 962–991 (cited in p. 12).

[18] A. S. van Heerden, D. M. Judt, C. P. Lawson, S. Jafari, T. Nikolaidis, and D. Bosak. "Framework for integrated dynamic thermal simulation of future civil transport aircraft". In: AIAA Scitech 2020 Forum. American Institute of Aeronautics and Astronautics, 2020 (cited in p. 12).

[19] S. G. Mackin and S. J. Tutko. "Bleed air boosted engine oil cooler". U.S. pat. 2020/0063660 A1 (The Boeing Company, Chicago, IL). 2020 (cited in p. 12).

[20] A. L. Simon, J.-C. M. Pierre Di Giovanni, and B. P. Marcell Morelli. "Lubricating and cooling core for a mechanical reduction gear of an aircraft turbofan engine". U.S. pat. 2020/0166117 A1 (SAFRAN Transmission Systems, Colombes). 2020 (cited in p. 12).

[21] T. Filburn, A. Kloter, and D. Cloud. "Design of a Carbon-Carbon Finned Surface Heat Exchanger for a High-Bypass Ratio, High Speed Gas Turbine Engine". In: ASME Turbo Expo 2006: Power for Land, Sea, and Air. Volume 3: Heat Transfer, Parts A and B. 2006, pp. 483–490 (cited in p. 12).

[22] J. Hesselgreaves. Compact Heat Exchangers. Selection, Design and Operation. 1st ed. Elsevier Science & Technology Books, 2001 (cited in pp. 12, 112).

[23] E. Klein, J. Ling, V. C. Aute, Y. Hwang, et al. "A Review of Recent Advances in Additively Manufactured Heat Exchangers". In: 2018 (cited in p. 12).

[24] C. Huang, W. Cai, Y. Wang, Y. Liu, Q. Li, and B. Li. "Review on the characteristics of flow and heat transfer in printed circuit heat exchangers". Applied Thermal Engineering 153, 2019, pp. 190–205 (cited in p. 12).

[25] H. Rastan, A. Abdi, B. Hamawandi, M. Ignatowicz, J. P. Meyer, and B. Palm. "Heat transfer study of enhanced additively manufactured minichannel heat exchangers". International Journal of Heat and Mass Transfer 161, 2020 (cited in p. 12).

[26] S. Gururatana and S. Skullong. "Heat transfer augmentation in a pipe with 3D printed wavy insert". Case Studies in Thermal Engineering 21, 2020 (cited in p. 12).

[27] J. H. Haertel and G. F. Nellis. "A fully developed flow thermofluid model for topology optimization of 3D-printed air-cooled heat exchangers". Applied Thermal Engineering 119, 2017, pp. 10–24 (cited in p. 12).

[28] R. A. Felber, N. Rudolph, and G. F. Nellis. "Design and Simulation of 3D Printed Air-Cooled Heat Exchangers". In: 26th Annual International Solid Freeform Fabrication Symposium. 2016, pp. 2250–2259 (cited in p. 12).

[29] A. Vafadar, F. Guzzomi, and K. Hayward. "Experimental investigation and comparison of the thermal performance of additively and conventionally manufactured heat exchangers". Metals 11, 4 2021 (cited in pp. 12, 16).

[30] D. Saltzman, M. Bichnevicius, S. Lynch, T. W. Simpson, et al. "Design and evaluation of an additively manufactured aircraft heat exchanger". Applied Thermal Engineering 138, 2018, pp. 254–263 (cited in pp. 12, 16).

[31] J. Adams. "Advanced heat transfer surfaces for gas turbine heat exchangers". PhD thesis. University of Oxford, 2004 (cited in p. 12).

[32] J. Doo, M. Ha, J. Min, R. Stieger, A. Rolt, and C. Son. "An investigation of crosscorrugated heat exchanger primary surfaces for advanced intercooled-cycle aero engines (Part-I: Novel geometry of primary surface)". International Journal of Heat and Mass Transfer 55, 2012, pp. 5256–5267 (cited in p. 12).

[33] P. Dube, S. Hiravennavar, and A. Ali Z. "Statistical Model to Predict Air Side Pressure Drop for Heat Exchangers". In: WCX World Congress Experience. 2018, pp. 2018–01–0081 (cited in p. 13).

[34] J. Doo, M. Ha, J. Min, R. Stieger, A. Rolt, and C. Son. "An investigation of crosscorrugated heat exchanger primary surfaces for advanced intercooled-cycle aero engines (Part-II: Design optimization of primary surface)". International Journal of Heat and Mass Transfer 61, 2013, pp. 138–148 (cited in p. 13).

[35] M. Bonjakovi, S. Muhi, and A. iki. "Experimental testing of the heat exchanger with star-shaped fins". International Journal of Heat and Mass Transfer 149, 2019 (cited in p. 13).

[36] H. Zhang, J. Guo, X. Cui, J. Zhou, et al. "Experimental and numerical investigations of thermal-hydraulic characteristics in a novel airfoil fin heat exchanger". International Journal of Heat and Mass Transfer 175, 2021 (cited in p. 13).

[37] J. Gong, J. Onishi, A. He, Y. Kametani, Y. Hasegawa, and N. Shikazono. "Heat transfer enhancement and pressure loss in a plate-fin heat exchanger with V-shaped oblique wavy surface". International Journal of Heat and Mass Transfer 161, 2020 (cited in p. 13).

[38] M. Chávez-Modena, L. M. González, and E. Valero. "Numerical Optimization of the Fin Shape Experiments of a Heat Conjugate Problem surface air/oil heat exchanger (SACOC)". Journal of Heat and Mass Transfer 182, 2021, p. 121971 (cited in pp. 13, 17, 30, 104, 105, 112, 154, 155).

[39] L. Zhang, Z. Qian, J. Deng, and Y. Yin. "Fluidstructure interaction numerical simulation of thermal performance and mechanical property on plate-fins heat exchanger". Heat and Mass Transfer 51 (9), 2015, pp. 1337–1353 (cited in p. 13).

[40] Z. Qu, W. Tao, and Y. He. "Three-dimensional numerical simulation on laminar heat transfer and fluid flow characteristic of strip fin surface with X arrangement of strips". Journal of Heat Transfer 126, 2004, pp. 697–707 (cited in p. 13).

[41] T. L. W.Q. Tao Y.P. Cheng. "The influence of strip location on the pressure drop and heat transfer performance of a slotted fin". Numerical Heat Transfer, Part A: Applications 52, 2007, pp. 463–480 (cited in p. 13).

[42] L. Villafañe and G. Paniagua. "Aerodynamic impact of finned heat exchangers on transonic flows". Experimental Thermal and Fluid Science 97, 2018, pp. 223–236 (cited in p. 14).

[43] S. Kim, J. K. Min, M. Y. Ha, and C. Son. "Investigation of high-speed bypass effect on the performance of the surface airoil heat exchanger for an aero engine". International Journal of Heat and Mass Transfer 77, 2014, pp. 321–334 (cited in pp. 14, 15).

[44] M. Kim, M. Y. Ha, and J. K. Min. "A numerical study on various pinfin shaped surface airoil heat exchangers for an aero gas-turbine engine". International Journal of Heat and Mass Transfer 93, 2016, pp. 637–652 (cited in p. 15).

[45] M. C. Gelain, A. Couilleaux, M. Errera, R. Vicquelin, and O. Gicquel. "Conjugate heat transfer analysis of a surface air-cooled oil cooler (SACOC) installed in a turbofan by-pass duct." In: AIAA Aviation 2021 Forum. 2021 (cited in pp. 15, 23, 120).

[46] K. Guo, N. Zhang, and R. Smith. "Optimisation of fin selection and thermal design of counter-current plate-fin heat exchangers". Applied Thermal Engineering 78, 2015, pp. 491–499 (cited in p. 15).

[47] R. K. Shah and D. P. Sekulic. "Selection of Heat Exchangers and Their Components". In: Fundamentals of Heat Exchanger Design. John Wiley & Sons, Ltd, 2003. Chap. 10, pp. 673–734 (cited in p. 15).

[48] R. M. Manglik and A. E. Bergles. "Heat transfer and pressure drop correlations for the rectangular offset strip fin compact heat exchanger". Experimental Thermal and Fluid Science 10 (2), 1995, pp. 171–180 (cited in pp. 16, 112).

[49] E. M. Sparrow, J. W. Ramsey, and C. A. C. Altemani. "Experiments on In-line Pin Fin Arrays and Performance Comparisons with Staggered Arrays". Journal of Heat Transfer 102 (1), 1980, pp. 44–50 (cited in p. 16).

[50] C. R. D. Losier, S. Subramanian, V. Ponyavin, Y. Chen, A. E. Hechanova, and P. F. Peterson. "The parametric study of an innovative offset strip-fin heat exchanger". Journal of Heat Transfer 129, 10 2007, pp. 1453–1458 (cited in p. 16).

[51] T. M. Jeng and S. C. Tzeng. "Pressure drop and heat transfer of square pin-fin arrays in in-line and staggered arrangements". International Journal of Heat and Mass Transfer 50, 11-12 2007, pp. 2364–2375 (cited in p. 16).

[52] F. Wang, J. Zhang, and S. Wang. "Investigation on flow and heat transfer characteristics in rectangular channel with drop-shaped pin fins". Propulsion and Power Research 1, 1 2012, pp. 64–70 (cited in p. 16).

[53] D. Soodphakdee, M. Behnia, and D. W. Copeland. "A Comparison of Fin Geometries for Heatsinks in Laminar Forced Convection: Part I-Round, Elliptical, and Plate Fins in Staggered and In-Line Configurations". The International Journal of Microcircuits and Electronic Packaging 24, 1 2001 (cited in p. 16).

[54] H. Jonsson and B. Moshfegh. "Modeling of the Thermal and Hydraulic Performance of Plate Fin, Strip Fin, and Pin Fin Heat Sinks-Influence of Flow Bypass". IEEE Transactions on components and packing technologies 24, 2 2001, pp. 142–149 (cited in p. 16).

[55] M. Wong, I. Owen, C. J. Sutcliffe, and A. Puri. "Convective heat transfer and pressure losses across novel heat sinks fabricated by Selective Laser Melting". International Journal of Heat and Mass Transfer 52, 1-2 2009, pp. 281–288 (cited in p. 16).

[56] O. Leon, G. Mey, and E. Dick. "Study of the optimal layout of cooling fins in forced convection cooling". Microelectronics Reliability 42, 7 2002, pp. 1101–1111 (cited in p. 16).

[57] O. A. Leon, G. D. Mey, E. Dick, and J. Vierendeels. "Staggered heat sinks with aerodynamic cooling fins". Microelectronics Reliability 44, 7 2004, pp. 1181–1187 (cited in p. 16).

[58] N. Limbasiya, A. Roy, and A. B. Harichandan. "Numerical simulation of heat transfer for microelectronic heat sinks with different fin geometries in tandem and staggered arrangements". Thermal Science and Engineering Progress 4, 2017, pp. 11–17 (cited in p. 16).

[59] V. S. Krishna and L. Dineshkumar. "Numerical analysis on enhancement of heat transfer in micro-heat sink using dimpling surface". In: AIP Conference Proceedings. Vol. 2200. American Institute of Physics Inc., 2019, pp. 020059-1–7 (cited in p. 16).

[60] N. Saleha, N. Fadèla, and A. Abbès. "Improving cooling effectiveness by use of chamfers on the top of electronic components". Microelectronics Reliability 55, 7 2015, pp. 1067–1076 (cited in p. 16).

[61] L. H. Tang, Z. Min, G. N. Xie, and Q. W. Wang. "Fin pattern effects on air-side heat transfer and friction characteristics of fin-and-tube heat exchangers with large number of large-diameter tube rows". Heat Transfer Engineering 30, 3 2009, pp. 171–180 (cited in p. 17).

[62] L. H. Tang, M. Zeng, and Q. W. Wang. "Experimental and numerical investigation on air-side performance of fin-and-tube heat exchangers with various fin patterns". Experimental Thermal and Fluid Science 33, 5 2009, pp. 818–827 (cited in p. 17).

[63] T. L. Ngo, Y. Kato, K. Nikitin, and T. Ishizuka. "Heat transfer and pressure drop correlations of microchannel heat exchangers with S-shaped and zigzag fins for carbon dioxide cycles". Experimental Thermal and Fluid Science 32, 2 2007, pp. 560–570 (cited in p. 17).

[64] N. Tsuzuki, Y. Kato, K. Nikitin, and T. Ishizuka. "Advanced microchannel heat exchanger with S-shaped fins". Journal of Nuclear Science and Technology 46, 5 2009, pp. 403–412 (cited in p. 17).

[65] X. Zhang, Y. Wang, P. Cang, and R. Wang. "Experimental investigation of thermal hydraulic performance of heat exchangers with different Reynolds numbers on both air-side and water-side". Applied Thermal Engineering 99, 2016, pp. 1331–1339 (cited in p. 17).

[66] G. J. Michna, A. M. Jacobi, and R. L. Burton. "An experimental study of the friction factor and mass transfer performance of an offset-strip fin array at very high Reynolds numbers". Journal of Heat Transfer 129, 9 2007, pp. 1134–1140 (cited in p. 17).

[67] J. Cohen and D. Bourell. "Development of Novel Tapered Pin Fin Geometries for Additive Manufacturing of Compact Heat Exchangers". In: Solid Freeform Fabrication Symposium. 2016, pp. 2314–2336 (cited in p. 17).

[68] I. Jaswal and F. E. Ames. "Heat Transfer and Pressure Drop Measurements in Constant and Converging Section Pin and Diamond Pedestal Arrays". Journal of Thermal Science and Engineering Applications 1 (1), 2009. 011006 (cited in p. 17).

[69] C. A. Borghi, A. Cristofolini, M. R. Carraro, C. Gorse, et al. "Non-Intrusive Characterization of the Ionized Flow Produced by Nozzle of an Hypersonic Wind Tunnel". In: 14th AIAA/AHI Space Planes and Hypersonic Systems and Technologies Conference. 2006 (cited in p. 18).

[70] L. Savino, F. D. Filippis, E. Marenna, and A. Cipullo. "Experimental Characterization of the CIRA Plasma Wind Tunnel Flow by Optical Emission Spectroscopy". In: 17th AIAA International Space Planes and Hypersonic Systems and Technologies Conference. 2011 (cited in p. 18).

[71] P. Sagnier and J. L. Vérant. "Flow characterization in the ONERA F4 high-enthalpy wind tunnel". AIAA Journal 36, 4 1998, pp. 522–531 (cited in p. 18).

[72] J. Oriol, J. P. Leclerc, C. Jallut, P. Tochon, and P. Clement. "Characterization of the two-phase flow regimes and liquid dispersion in horizontal and vertical tubes by using coloured tracer and non-intrusive optical detector". Chemical Engineering Science 63, 1 2008, pp. 24–34 (cited in p. 19).

[73] M. J. Rightley, L. K. Matthews, and G. P. Mulholland. "Experimental characterization of the heat transfer in a free-falling-particle receiver". Solar Energy 48, 6 1992, pp. 363–374 (cited in p. 19).

[74] G. V. Iungo. "Experimental characterization of wind turbine wakes: Wind tunnel tests and wind LiDAR measurements". Journal of Wind Engineering and Industrial Aerodynamics 149, 2016, pp. 35–39 (cited in p. 19).

[75] D. A. Olson, A. W. Katz, A. M. Naguib, M. M. Koochesfahani, D. P. Rizzetta, and M. R. Visbal. "On the challenges in experimental characterization of flow separation over airfoils at low Reynolds number". Experiments in Fluids 54, 2 2013 (cited in p. 19).

[76] G. Buresti, A. Talamelli, and P. Petagna. "Experimental characterization of the velocity field of a coaxial jet configuration". Experimental Thermal and Fluid Science 9, 2 1994, pp. 135–146 (cited in pp. 19, 21).

[77] J. Scrittore, K. Thole, and S. Burd. "Experimental Characterization of Film-Cooling Effectiveness Near Combustor Dilution Holes". In: Proceedings of the ASME Turbo Expo. Vol. 3. 2005 (cited in p. 19).

[78] K. B. Lee and Y. K. Kwon. "Flow and thermal field with relevance to heat transfer enhancement of interrupted-plate heat exchangers". Experimental Heat Transfer 5, 2 1992, pp. 83–100 (cited in p. 19).

[79] Q. W. Dong, Y. Q. Wang, and M. S. Liu. "Numerical and experimental investigation of shellside characteristics for RODbaffle heat exchanger". Applied Thermal Engineering 28, 7 2008, pp. 651–660 (cited in pp. 19, 21).

[80] K. P. Gertzos and Y. G. Caouris. "Experimental and computational study of the developed flow field in a flat plate integrated collector storage (ICS) solar device with recirculation". Experimental Thermal and Fluid Science 31, 8 2007, pp. 1133–1145 (cited in pp. 19, 21).

[81] K. P. Gertzos and Y. G. Caouris. "Optimal arrangement of structural and functional parts in a flat plate integrated collector storage solar water heater (ICSSWH)". Experimental Thermal and Fluid Science 32, 5 2008, pp. 1105–1117 (cited in p. 19).

[82] D. Saltzman and S. Lynch. "Flow-Field Measurements in a Metal Additively Manufactured Offset Strip Fin Array Using Laser Doppler Velocimetry". Journal of Fluids Engineering, Transactions of the ASME 143, 4 2021 (cited in pp. 19, 21).

[83] F. Vitillo, L. Cachon, F. Reulet, and P. Millan. "Flow analysis of an innovative compact heat exchanger channel geometry". International Journal of Heat and Fluid Flow 58, 2016, pp. 30–39 (cited in pp. 20, 21).

[84] J. Wen, Y. Li, S. Wang, and A. Zhou. "Experimental investigation of header configuration improvement in plate-fin heat exchanger". Applied Thermal Engineering 27, 11-12 2007, pp. 1761–1770 (cited in pp. 20, 21).

[85] M. Yataghene, F. Francine, and L. Jack. "Flow patterns analysis using experimental PIV technique inside scraped surface heat exchanger in continuous flow condition". Applied Thermal Engineering 31, 14-15 2011, pp. 2855–2868 (cited in pp. 20, 21).

[86] D. Yashar, H. Cho, and P. Domanski. "Measurement of Air-Velocity Profiles for Finned-Tube Heat Exchangers Using Particle Image Velocimetry". In: International Refrigeration and Air Conditioning Conference. 2008 (cited in p. 20).

[87] G. F. Naterer and O. B. Adeyinka. "New laser based method for non-intrusive measurement of available energy loss and local entropy production". Experimental Thermal and Fluid Science 31, 2 2006, pp. 91–95 (cited in p. 20).

[88] D. Jaíková, P. varc, V. Dvoák, and V. Kopecký. "Fluid velocity and LIF temperature measurement in a real model of heat exchanger". In: EPJ Web of Conferences. Vol. 25. 2012 (cited in pp. 20, 21).

[89] S. Amiri, R. Taher, and L. Mongeau. "Quantitative visualization of temperature field and measurement of local heat transfer coefficient over heat exchanger elements in sinusoidal oscillating flow". Experimental Thermal and Fluid Science 85, 2017, pp. 22–36 (cited in p. 20).

[90] P. Bencs, S. Szabó, R. Bordás, K. Zähringer, and D. Thévenin. "Synchronization of Particle Image Velocimetry and Background Oriented Schlieren measurement techniques". In: PSFVIP-8: The 8th Pacific Symposium on Flow Visualization and Image Processing. 2011 (cited in pp. 20, 21).

[91] S. C. Tirtey, L. Walpot, O. Chazot, and D. Fletcher. "Experimental Characterization of Hypersonic Boundary Layer in Flight and in Wind-tunnel Condition". In: 14th AIAA/AHI Space Planes and Hypersonic Systems and Technologies Conference. 2006 (cited in p. 20).

[92] R. S. Mullisen and R. I. Loehrke. "A Study of the Flow Mechanisms Responsible for Heat Transfer Enhancement in Interrupted-Plate Heat Exchangers". Journal of Heat Transfer 108, 2 1986, pp. 377–385 (cited in pp. 20, 21).

[93] W. Jarosinski. "Experimental Study of Heat Transfer from the Heated Rib-Roughed Wall to a Steady or Pulsating Flow". In: SAE Technical Paper 2001-01-1249. 2001 (cited in pp. 20, 21).

[94] N. S. Rajput and A. Srivastava. "Non-intrusive dynamic measurements of nanofluid-based heat transfer phenomena under thermally developing flow regime in the context of compact channels". Experimental Thermal and Fluid Science 74, 2016, pp. 271–285 (cited in pp. 20, 21).

[95] P. Leblay, J. F. Henry, D. Caron, D. Leducq, L. Fournaison, and A. Bontemps. "Characterisation of the hydraulic maldistribution in a heat exchanger by local measurement of convective heat transfer coefficients using infrared thermography". Energy Economics 45, 2014, pp. 73–82 (cited in p. 21).

[96] S. Somasundharam and K. S. Reddy. "Simultaneous estimation of thermal properties of orthotropic material with non-intrusive measurement". International Journal of Heat and Mass Transfer 126, 2018, pp. 1162–1177 (cited in p. 21).

[97] M. Mobtil, D. Bougeard, and S. Russeil. "Experimental study of inverse identification of unsteady heat transfer coefficient in a fin and tube heat exchanger assembly". International Journal of Heat and Mass Transfer 125, 2018, pp. 17–31 (cited in p. 21).

[98] V. Kulkarni, N. Sahoo, and S. D. Chavan. "Simulation of honeycomb-screen combinations for turbulence management in a subsonic wind tunnel". Journal of Wind Engineering and Industrial Aerodynamics 99, 1 2011, pp. 37–45 (cited in p. 22).

[99] K. Ghorbanian, M. R. Soltani, and M. D. Manshadi. "Experimental investigation on turbulence intensity reduction in subsonic wind tunnels". Aerospace Science and Technology 15, 2 2011, pp. 137–147 (cited in p. 22).

[100] A. L. Sullivan, I. K. Knight, R. J. Hurley, and C. Webber. "A contraction-less, low-turbulence wind tunnel for the study of free-burning fires". Experimental Thermal and Fluid Science 44, 2013, pp. 264–274 (cited in p. 22).

[101] J. B. Barlow, W. H. Rae, and A. Pope. Low-speed wind tunnel testing. 3rd ed. New York: Wiley, 1999. 713 pp. (cited in p. 22).

[102] J. Paduano, E. Greitzer, and A. Epstein. "Compression System Stability and Active Control". Annual Review of Fluid Mechanics 33 (1), 2001, pp. 491–517 (cited in p. 22).

[103] X. J. Yu and B. J. Liu. "Stereoscopic PIV measurement of unsteady flows in an axial compressor stage". Experimental Thermal and Fluid Science 31, 8 2007, pp. 1049–1060 (cited in p. 22).

[104] T. D. Toge and A. Pradeep. "Experimental investigation of stall inception of a low speed contra rotating axial flow fan under circumferential distorted flow condition". Aerospace Science and Technology 70, 2017, pp. 534–548 (cited in pp. 22, 26).

[105] J. Li, J. Du, Y. Liu, H. Zhang, and C. Nie. "Effect of inlet radial distortion on aerodynamic stability in a multi-stage axial flow compressor". Aerospace Science and Technology 105, 2020 (cited in p. 22).

[106] C. Tan, I. Day, S. Morris, and A. Wadia. "Spike-Type Compressor Stall Inception, Detection, and Control". Annual Review of Fluid Mechanics 42 (1), 2010, pp. 275–300 (cited in p. 22).

[107] F. J. Zenger, A. Renz, M. Becher, and S. Becker. "Experimental investigation of the noise emission of axial fans under distorted inflow conditions". Journal of Sound and Vibration 383, 2016, pp. 124–145 (cited in p. 22).

[108] P. Lin, M. Wang, C. Wang, and J. Fu. "Abrupt stall detection for axial compressors with non-uniform inflow via deterministic learning". Neurocomputing 338, 2019, pp. 163–171 (cited in p. 22).

[109] P. B. Salunkhe, J. Joseph, and A. M. Pradeep. "Active feedback control of stall in an axial flow fan under dynamic inflow distortion". Experimental Thermal and Fluid Science 35, 6 2011, pp. 1135–1142 (cited in p. 22).

[110] S-16 Turbine Engine Inlet Flow Distortion Committee. "A Methodology for Assessing Inlet Swirl Distortion". In: SAE Mobilus. 2017, p. 110 (cited in p. 23).

[111] J. R. Lucas, W. F. OBrien, and A. M. Ferrar. "Effect of BLIType Inlet Distortion on Turbofan Engine Performance". In: ASME Turbo Expo 2014: Turbine Technical Conference and Exposition. Volume 1A: Aircraft Engine; Fans and Blowers. 2014, V01AT01A037 (cited in p. 23).

[112] G. Tanguy, D. G. MacManus, E. Garnier, and P. G. Martin. "Characteristics of unsteady total pressure distortion for a complex aero-engine intake duct". Aerospace Science and Technology 78, 2018, pp. 297–311 (cited in pp. 23, 26).

[113] M. Migliorini, P. Zachos, and D. MacManus. "The impact of inlet boundary layer thickness on the unsteady aerodynamics of S-duct intakes". In: AIAA Propulsion and Energy 2019 Forum. 2019, p. 15 (cited in pp. 23, 26).

[114] E. Valencia, V. Alulema, D. Rodriguez, P. Laskaridis, and I. Roumeliotis. "Novel fan configuration for distributed propulsion systems with boundary layer ingestion on an hybrid wing body airframe". Thermal Science and Engineering Progress 18, 2020, p. 100515 (cited in p. 23).

[115] A. J. Provenza, K. P. Duffy, and M. A. Bakhle. "Aeromechanical Response of a Distortion-Tolerant Boundary Layer Ingesting Fan". Journal of Engineering for Gas Turbines and Power 141 (1), 2019, p. 011011 (cited in p. 23).

[116] G. McLelland, D. G. MacManus, P. K. Zachos, D. Gil-Prieto, and M. Migliorini. "Influence of Upstream Total Pressure Profiles on S-Duct Intake Flow Distortion". Journal of Propulsion and Power 36 (3), 2020, pp. 346–356 (cited in p. 23).

[117] M. M. Wojewodka, C. White, S. Shahpar, and K. Kontis. "Numerical study of complex flow physics and coherent structures of the flow through a convoluted duct". Aerospace Science and Technology, 2021, p. 107191 (cited in p. 23).

[118] A. G. Harouni. "Flow control of a boundary layer ingesting serpentine diffuser via blowing and suction". Aerospace Science and Technology 39, 2014, pp. 472–480 (cited in p. 23).

[119] D. J. Frohnapfel, K. Todd Lowe, and W. F. O'Brien. "Experimental Quantification of Fan Rotor Effects on Inlet Swirl Using Swirl Distortion Descriptors". Journal of Engineering for Gas Turbines and Power 140 (8), 2018, p. 082603 (cited in p. 23).

[120] T. Guimarães, K. T. Lowe, and W. F. OBrien. "Vortical flow development in round ducts across scales for engine inlet applications". Experiments in Fluids 60 (4), 2019, p. 52 (cited in pp. 23, 26).

[121] S. Gorton, L. Owens, L. Jenkins, B. Allan, and E. Schuster. "Active Flow Control on a Boundary-Layer-Ingesting Inlet". In: 42nd AIAA Aerospace Sciences Meeting and Exhibit. 2004, p. 12 (cited in p. 23).

[122] P. P. Walsh and P. Fletcher. Gas turbine performance. 2nd ed. Malden, MA: Blackwell Science, 2004. 646 pp. (cited in p. 23).

[123] K. Ameur, C. Masson, and P. J. Eecen. "2D and 3D numerical simulation of the wind-rotor/nacelle interaction in an atmospheric boundary layer". Journal of Wind Engineering and Industrial Aerodynamics 99, 8 2011, pp. 833–844 (cited in p. 23).

[124] T. Maruyama. "Surface and inlet boundary conditions for the simulation of turbulent boundary layer over complex rough surfaces". Journal of Wind Engineering and Industrial Aerodynamics 81, 1999, pp. 311–322 (cited in p. 23).

[125] T. Maruyama, W. Rodi, Y. Maruyama, and H. Hiraoka. "Large eddy simulation of the turbulent boundary layer behind roughness elements using an artificially generated inflow". Journal of Wind Engineering and Industrial Aerodynamics 83, 1999, pp. 381–392 (cited in p. 23).

[126] H. Kozmar. "Flow, turbulence and surface pressure on a wall-mounted cube in turbulent boundary layers". Journal of Wind Engineering and Industrial Aerodynamics 210, 2021 (cited in p. 24).

[127] T. C. Hohman, T. V. Buren, L. Martinelli, and A. J. Smits. "Generating an artificially thickened boundary layer to simulate the neutral atmospheric boundary layer". Journal of Wind Engineering and Industrial Aerodynamics 145, 2015, pp. 1–16 (cited in p. 24).

[128] A. Jafari, F. Ghanadi, M. Arjomandi, M. J. Emes, and B. S. Cazzolato. "Correlating turbulence intensity and length scale with the unsteady lift force on flat plates in an atmospheric boundary layer flow". Journal of Wind Engineering and Industrial Aerodynamics 189, 2019, pp. 218–230 (cited in p. 24).

[129] R. A. Catarelli, P. L. Fernández-Cabán, F. J. Masters, J. A. Bridge, K. R. Gurley, and C. J. Matyas. "Automated terrain generation for precise atmospheric boundary layer simulation in the wind tunnel". Journal of Wind Engineering and Industrial Aerodynamics 207, 2020 (cited in p. 24).

[130] H. Kikitsu, J. Kanda, and R. Iwasaki. "Flow simulation by wind tunnel with computer-controlled multiple fans". Journal of Wind Engineering and Industrial Aerodynamics 83, 1995, pp. 421–429 (cited in p. 24).

[131] A. Nishi, H. Kikugawa, Y. Matsuda, and D. Tashiro. "Active control of turbulence for an atmospheric boundary layer model in a wind tunnel". Journal of Wind Engineering and Industrial Aerodynamics 83, 1999, pp. 409–419 (cited in p. 24).

[132] W. T. Ecker, K. W. Mort, and J. Jope. Aerodynamic design guidelines and computer program for estimation of subsonic wind tunnel performance. Washington D.C.: National Aeronautics and Space Administration. 197 pp. (cited in pp. 24, 80).

[133] P. R. Owen and H. K. Zienkiewicz. "The production of uniform shear flow in a wind tunnel". Journal of Fluid Mechanics 2 (6), 1957, p. 521 (cited in pp. 25, 26).

[134] J. C. Phillips, N. H. Thomas, R. J. Perkins, and P. C. H. Miller. "Wind tunnel velocity profiles generated by differentially-spaced flat plates". Journal of Wind Engineering and Industrial Aerodynamics 80, 1999, pp. 253–262 (cited in pp. 25, 26).

[135] M. Saleem Yusoof, M. Sivapragasam, and M. Deshpande. "Strip distortion generator for simulating inlet flow distortion in gas turbine engine ground test facilities". Propulsion and Power Research 5 (4), 2016, pp. 287–301 (cited in p. 25).

[136] F. ONeill. "Source models of flow through and around screens and gauzes". Ocean Engineering 33 (14), 2006, pp. 1884–1895 (cited in p. 25).

[137] K. Steiros and M. Hultmark. "Drag on flat plates of arbitrary porosity". Journal of Fluid Mechanics 853, 2018, p. 11 (cited in p. 25).

[138] J.-K. Koo and D. F. James. "Fluid flow around and through a screen". Journal of Fluid Mechanics 60 (3), 1973, p. 513 (cited in p. 25).

[139] W. Schneck, A. Ferrar, J. Bailey, K. Hoopes, and W. O'Brien. "Improved Prediction Method for the Design of High-Resolution Total Pressure Distortion Screens". In: 51st AIAA Aerospace Sciences Meeting including the New Horizons Forum and Aerospace Exposition. 2013, p. 19 (cited in pp. 25, 26).

[140] J. E. Stephens, M. Celestina, and C. Hughes. "Swirl Distortion Using Stream Vanes for Boundary Layer Ingestion Research". In: ASME Turbo Expo 2019: Turbomachinery Technical Conference and Exposition. Volume 2A: Turbomachinery. 2019, V02AT39A035 (cited in pp. 25, 26).

[141] M. Sivapragasam. "Flow field behind a complex total pressure distortion screen". In: Proceedings of the Institution of Mechanical Engineers, Part G: Journal of Aerospace Engineering. Vol. 233. 14. 2019, pp. 5075–5092 (cited in pp. 25, 26).

[142] P. Roach. "The generation of nearly isotropic turbulence by means of grids". International Journal of Heat and Fluid Flow 8 (2), 1987, pp. 82–92 (cited in p. 26).

[143] Y. Huang, X. He, P. Jiang, and H. Zhu. "Effect of non-uniform inlet velocity profile on flow field characteristics of a bluff body". Experimental Thermal and Fluid Science 118, 2020 (cited in p. 26).

[144] B. Overall. "A Procedure for the Design of Complex Distortion Screen Patterns for Producing Specified Steady-State Total Pressure Profiles at the Inlet of Turbine Engines". In: Report AD890870, US Air Force. 1972, p. 56 (cited in pp. 26, 78).

[145] S.-W. Hong, I.-B. Lee, and I.-H. Seo. "Modelling and predicting wind velocity patterns for windbreak fence design". Journal of Wind Engineering and Industrial Aerodynamics 142, 2015, pp. 53–64 (cited in p. 26).

[146] J. V. Taylor. "Complete flow conditioning gauzes". Experiments in Fluids 60 (3), 2019, p. 35 (cited in p. 26).

[147] S. Etheridge, J. G. Lee, C. Carter, M. Hagenmaier, and R. Milligan. "Effect of flow distortion on fuel/air mixing and combustion in an upstream-fueled cavity flameholder for a supersonic combustor". Experimental Thermal and Fluid Science 88, 2017, pp. 461–471 (cited in p. 27).

[148] K. Yu, J. Xu, L. Tang, and J. Mo. "Inverse design of inlet distortion using method of characteristics for direct-connect scramjet studies". Aerospace Science and Technology 46, 2015, pp. 351–359 (cited in p. 27).

[149] A. Torregrosa, A. Broatch, J. García-Tíscar, and F. Roig. "Experimental verification of hydrodynamic similarity in hot flows". Experimental Thermal and Fluid Science 119, 2020, p. 110220 (cited in pp. 30, 111).

[150] J. R. Serrano, F. J. Arnau, L. M. Gracía-Cuevas, V. Samala, and L. Smith. "Experimental approach for the characterization and performance analysis of twin entry radial-inflow turbines in a gas stand and with different flow admission conditions". Applied Thermal Engineering 159, 2019, p. 113737 (cited in p. 30).

[151] J. R. Serrano, F. J. Arnau, L. M. García-Cuevas, P. Soler, and R. Cheung. "Experimental validation of a one-dimensional twin-entry radial turbine model under non-linear pulse conditions". International Journal of Engine Research, 2019, p. 1468087419869157 (cited in p. 30).

[152] Community Research and Development Information Service. "Novel system removes debris from compressor". In: Research*eu results magazine. Vol. 50. Publications Office of the European Union, 2016, p. 22 (cited in p. 30).

[153] G. Paniagua, D. Cuadrado, J. Saavedra, V. Andreoli, et al. "Design of the Purdue Experimental Turbine Aerothermal Laboratory for Optical and Surface Aerothermal Measurements". Journal of Engineering for Gas Turbines and Power 141 (1), 2018 (cited in p. 31).

[154] G. K. Gyimah, Z.-n. Guo, P. Huang, S.-z. Jiang, et al. "Improvers of Pressure-Viscosity Coefficients of Two-Phase Liquid-Solid Lubricants". DEStech Transactions on Engineering and Technology Research, amita 2016 (cited in p. 38).

[155] S. Wrenick, P. Sutor, H. Pangilinan, and E. E. Schwarz. "Heat Transfer Properties of Engine Oils". In: World Tribology Congress III, Volume 1. 2005, pp. 595–596 (cited in p. 38).

[156] M. Raffel, C. Willert, S. Wereley, and J. Kompenhans. Particle Image Velocimetry: A Practical Guide. Third edition. Springer, 2007, p. 680 (cited in p. 45).

[157] A. Boutier and J.-M. Most. "Laser Doppler Velocimetry". In: Laser Velocimetry in Fluid Mechanics. ISTE Ltd, 2012. Chap. 3, pp. 33–138 (cited in p. 51).

[158] G. Settles. Schlieren and Shadowgraph Techniques: Visualizing Phenomena in Transparent Media. First edition. Springer, 2001, p. 376 (cited in p. 53).

[159] P. Chiariotti, C. Rembe, P. Castellini, and M. Allen. Laser Doppler Vibrometry Measurements in Structural Dynamics. Springer New York, 2020, pp. 1–45 (cited in p. 55).

[160] W. Thielicke and R. Sonntag. "Particle Image Velocimetry for MATLAB: Accuracy and enhanced algorithms in PIVlab". Journal of Open Research Software 9 (1), 2021 (cited in p. 63).

[161] D. Harper and W. Brown. Mathematical equations for heat conduction in the fins of air cooled engines. NACA Report No. 158, 1922, p. 33 (cited in p. 72).

[162] P. J. Schneider. Conduction Heat Transfer. Addison-Wesley, 1957, p. 418 (cited in p. 72).

[163] J. Kirchner. "Data Analysis Toolkit #5: Uncertainty Analysis and Error Propagation". In: Report from University of California. 2001 (cited in p. 74).

[164] H. H. Ku. "Notes on the Use of Propagation of Error Formulas". Journal of Research of the National Bureau of Standards 70 C, 4 1966, pp. 263–273 (cited in p. 75).

[165] L. Andreassi, S. Cordiner, and V. Mulone. "Cell Shape Influence on Mass Transfer and Backpressure Losses in an Automotive Catalytic Converter". In: 2004 SAE Fuels & Lubricants Meeting & Exhibition. 2004, pp. 2004–01–1837 (cited in p. 78).

[166] S. Biswas, J. Kumar, M. Ganeshachar, S. N. Babu, and S. Ramachandra. "Fatigue Failure of a Distortion Screen during Testing". Procedia Engineering 55, 2013, pp. 487–492 (cited in p. 78).

[167] I. Gibson, D. W. Rosen, B. Stucker, et al. Additive manufacturing technologies. Vol. 17. Springer, 2014 (cited in p. 84).

[168] F. Menter. "Zonal Two Equation k-w Turbulence Models For Aerodynamic Flows". In: 24th Fluid Dynamics Conference. American Institute of Aeronautics and Astronautics, 1993, p. 22 (cited in p. 87).

[169] F. R. Menter, P. E. Smirnov, T. Liu, and R. Avancha. "A One-Equation Local Correlation-Based Transition Model". Flow, Turbulence and Combustion 95 (4), 2015, pp. 583–619 (cited in p. 88).

[170] Alcoa Global Cold Finished Products. Characteristics of Aluminium 7075. 2021 (cited in p. 102).

[171] F. P. Incropera. Fundamentals of heat and mass transfer. 6th ed. Hoboken, NJ: John Wiley, 2007 (cited in pp. 103, 118).

[172] F. Giannetti and P. Luchini. "Structural sensitivity of the first instability of the cylinder wake". Journal of Fluid Mechanics 581 (1), 2007, pp. 167–197 (cited in p. 104).

[173] P. Luchini and A. Bottaro. "Adjoint equations in stability analysis". Annual Review of fluid mechanics 46, 2014, pp. 493–517 (cited in p. 104).

[174] P. Thomas. "Steady-state compressible and incompressible flow". In: Simulation of Industrial Processes for Control Engineers. First edition. Elsevier, 1999. Chap. 4 & 6, pp. 32-40 & 50–59 (cited in pp. 111, 112).